

**Hydrothermal and Ionothermal Carbon  
Structures:**

**From carbon negative materials  
to energy applications.**

**Dissertation**

zur Erlangung des akademischen Grades  
Doktor der Naturwissenschaften (Dr. rer. nat.)  
in der Wissenschaftsdisziplin „Kolloidchemie“

eingereicht an der  
Mathematisch-Naturwissenschaftlichen Fakultät  
der Universität Potsdam

von

**Tim-Patrick Fellingner**

Geboren am 28.03.1983 in Berlin

Potsdam-Golm, im September 2011

Published online at the  
Institutional Repository of the University of Potsdam:  
URL <http://opus.kobv.de/ubp/volltexte/2012/5782/>  
URN <urn:nbn:de:kobv:517-opus-57825>  
<http://nbn-resolving.de/urn:nbn:de:kobv:517-opus-57825>

## Acknowledgement

First of all I would like to thank all the persons, who somehow contributed to the success of the present work.

I would like to thank my supervisor **Prof. Dr. Markus Antonietti** for the chance to do my PhD at the MPI, especially under his direct supervision. The present work certainly took benefit of his intensive supervision and advancement as well as his patience and inspiration. I would further like to thank for his professional and personal advice.

Sincere thanks are given to **Prof. Arne Thomas**, **Prof. John Texter** and **Prof. Shu-Hong Yu** for agreeing to examine this work.

**Dr. Maria-Magdalena Titirci** is acknowledged for co-laboration in the context of hydrothermal carbon and social integration into the sustainable materials group.

I would like to particular thank **Dr. Robin Jeremy White** for a lot of helpful professional advice and scientific exchange, but also very unprofessional and entertaining personal exchange.

Frédéric Hasché (TU Berlin / Strasser group) is thanked for the fruitful co-laboration.

Markus Engenhorst (TU Duisburg / Schmechel group) is acknowledged for fancy conductivity measurements.

Carmen Serra (Uni Vigo), Camillo Falco, Niki Baccile (CNRS Paris) and Jan Dirk Epping (TU Berlin), Sören Selve (TU Berlin), Prof. Smirnova's group (TU Hamburg-Harburg), Vitaly Budarin (Uni York), Bodo Ryschka, technicians Rona Pitschke, Heike Runge and Regina Rothe are acknowledged for XPS, NMR, HRTEM measurements, supercritical drying, technical support, SEM / TEM imaging and general help.

I would like to thank Britta Seidt and Debora Ressnig for their internship work. Best wishes for your future at the MPI!

Further on I would like to thank my (former office and lab) mates, Jens P., Johannes S., Micha B., Antje W., Katja J., Vasana F., Nicola R., Wen Y., Yuanjian Z., Li Zhao, Jérôme R., Bettina M., and my (present office and lab) mates Stephanie W., Nina F., Daniel K. and Regina R. which created and still create a very enjoyable atmosphere.

Additionally, I want to thank all the other personal work-life-balances, Rafael G., Helmut C., Camillo F., Dmitri F., Caro v. D., Vroni B., Claudia L., Micha K., Jörg M., John B., Alex K., Shiori K., Constanze V., Stefan G., Flo H., ChristinE, ChristinA, Niels t. B., Daniel K., Alfonso G. M., Irene T., Miriam U. and all the other persons, which could not be mentioned here but also generate an excellent working environment.

Finally, I would like to thank my family and friends for their understanding and support.

## Table of content

### *Hydrothermal and Ionothermal Carbon Structures:*

<i>Introduction – Carbon, Climate and Energy</i>	<i>1</i>
<i>A Hydrothermal Carbon</i>	<i>4</i>
Basics and State-of-the-Art	4
A1 Reaction Pathway of the Hydrothermal Carbonisation	8
A2 The Hydrothermal Carbonisation of Glucose, Catalysed by Borax	20
A3 Carbon Aerogels with Optimised Surface Area and Transport Porosity via Borax-Mediated Hydrothermal Carbonisation of Glucose	27
A4 Functional Carbon Spheres via Hydrothermal Carbonisation of Biowaste	38
<i>B Ionic Liquid-Derived Heteroatom-Containing Carbons – Synthesis, structure control and potential as non-metal electrocatalysts in the oxygen reduction reaction</i>	<i>45</i>
Basics and State-of-the-Art	45
1) The Oxygen Reduction Reaction (ORR)	45
2) Electrocatalysis	46
3) Heteroatom - containing Carbons from Ionic Liquid Precursors	49
B1 Ionic Liquid-Based Nitrogen-Doped Carbons as Highly Active Non-Metal Catalysts for PEMFCs	56
B2 Mesoporous Nitrogen – Doped Carbon for the Selective Electrocatalytic Synthesis of Hydrogen Peroxide	61
B3 Ionothermal Synthesis of Graphitic Boron Carbon Nitride: Reaction mechanism, chemical structure and physicochemical properties	70
<i>C Conclusions</i>	<i>98</i>
<i>D Applied Methods</i>	<i>104</i>
<i>E Experimental Part</i>	<i>114</i>
<i>F Appendix</i>	<i>117</i>
<i>G References</i>	<i>125</i>

## Introduction – Carbon, Climate and Energy

The industrial revolution in the second half of the 18<sup>th</sup> century significantly altered mankind, society and, more generally, the world. Fossil fuels started to replace wind and water as power source in automotive and factories, leading to substantial gains in efficiency, and eventually being converted into electricity in the 19<sup>th</sup> century. These changes have led to ever improving living standards, but at the expense of our carbon footprint by drastically increasing carbon dioxide emissions. The 20<sup>th</sup> century witnessed the emergence and industrial development of synthetic polymers which are now present in every part of our life, with some social commentators already referring to this era as the “*century of plastics*”. All the advantages of plastics in our daily life (prosthetics, lightweight equipment, cheapness, *etc.*) further improve the quality of life we experience, but also influence our consuming habits by altering our societal mind set to a “throw-away” culture, in turn generating megaton quantities of waste. Another “*game changer*” in the late 20<sup>th</sup> century was ever our increasing energy consumption, partly induced by the development of electric devices. It can for instance be symbolised by computers, which do not only help with work and communication, but are running practically continuously in multiple environments including the domestic homes of the western and increasingly so in the developing world. As a consequence, the worldwide demand for electrical energy, which was 8.3 million GWh in 1980, has increased drastically to 18.9 million GWh by 2006. By 2030, the need is estimated to further increase and reach 30.7 million GWh.<sup>[1]</sup>

All these developments make carbon the key elemental component, usually blended into notations such as “*carbon cycle*” or “*carbon footprint*”. Neglecting the minor amounts of uranium, the fossil resources crude oil, natural gas and coal are our primary sources for energy and chemical raw materials. In this context, two major global problems are not only foreseeable, but already dictate the global economy and political environment of our time; on one hand, crude oil is running short. Even if alternative ways for energy generation can be established, oil would still be needed as a raw source for chemistry, plastics and also fine chemicals and medical drugs production. In this respect,

the world simply cannot continue to grow and develop in the way it did over the last two centuries; rather a dead - end of such economy is to be expected. Concurrently, oxidation of carbon - rich fuels, at the end of the pipe, produces vast amounts of carbon dioxide (CO<sub>2</sub>). Being a greenhouse gas, CO<sub>2</sub> emissions are believed to be partly responsible for global warming and climate changes.

The need for sustainable energy generation, but also sustainable chemistry is thus of the highest priority and is at the origin of tremendous research activities across many different scientific disciplines. It also sets the framework of the present thesis. Natural biomass, created *via* the photosynthetic conversion of CO<sub>2</sub> from the environment, can be used as an energy source, as well as serving as a base feedstock for chemistry. It is clear by the sheer quantity required that biomass alone however, will never fulfil the energy needs of mankind alone (for that photoenergy conversion, geothermal power plants or wind energy have to be developed as well). However, it can play a major role in the so - called carbon storage and reuse (CSR) strategy, which might reduce the CO<sub>2</sub> level and counteract global warming by generating new materials, chemical feedstock, or even transportable fuels. In this regard, the generation of long lasting materials is certainly an appropriate process for storing carbon. However, traditional procedures to prepare functional carbons do not follow sustainable principles such as energy and atom economy, low toxicity and use of renewable resources.<sup>[2]</sup> Therefore, hydrothermal carbonisation (HC), a mimic of natural coalification, has recently attracted a lot of interest in both academia and industry.<sup>[3]</sup> HC is a method used to effectively convert carbohydrate - rich (waste) biomass into carbonaceous materials under comparably mild conditions (*i.e.* 160 - 200 °C and self - generated pressure). Briefly, HC can be seen as a model system for a green and sustainable process to transfer low value and widely available biomass into useful carbon negative materials.<sup>[4]</sup>

Interestingly, carbon materials also considerably contribute to the field of energy - related applications, *i.e.* they also help to generate, store, transport, and save energy. Their practically unlimited availability at low costs combined with desirable physicochemical properties like electrical conductivity, thermal and chemical stability, have led to an almost ubiquitous usage of carbon in electric and electronic devices, such as electrodes in high - tech applications. Nanostructured carbon is already used in fuel

cells, conventional batteries and supercapacitors, but is expected to play an even much bigger role in new forthcoming energy schemes. The importance of this operation can be demonstrated with a single example: wind energy, solar energy and wave power do not deliver energy permanently and need therefore, for efficient use, to be combined with massive energy storage devices. If such devices could be made with sustainable carbons as key components, the scene for carbon research is set.

In this thesis, both concepts, *i.e.* the sustainable use of biomass to produce CO<sub>2</sub>-negative functional materials and the use of high performance carbon materials for energy-related applications, are investigated. In the first part a literature review of hydrothermolysis, hydrothermal carbonisation of sugars and the respective chemistry is summarised in proposed mechanistic reaction pathways to hydrothermal carbon. A highly active and sustainable carbonisation catalyst, namely borax (Na<sub>2</sub>B<sub>4</sub>O<sub>7</sub> · 10 H<sub>2</sub>O), is proposed and discussed with regard to its effectuality in the context of the proposed HC reaction pathway. Furthermore, the hydrothermal carbonisation is extended to a new concept towards meaningful carbon nanostructures *via* borax addition and a model case of successful employment of biomass waste. In the second part, carbonisable cyano-containing ionic liquids (ILs) are employed as direct precursors for the synthesis of heteroatom-containing carbon materials. A chemical tool, to nanostructure the final material is introduced and the selection of materials producible *via* the ionic liquid route is expanded to graphitic boron carbon nitride. The ternary material is simply achieved by the employment of 1-ethyl-3-methylimidazolium tetracyanoborate (Emim-TCB). A detailed mechanistic investigation and structure characterisation employing calorimetric, spectroscopic, microscopic and scattering methods is provided. The presented materials show very interesting and desirable physicochemical properties, making them potentially applicable, as will be demonstrated, in energy-related devices like polymer-electrolyte membrane fuel cells.

# A Hydrothermal Carbon

## Basics and State-of-the-Art

The process of hydrothermal carbonisation (HC) usually comprises the decomposition of carbohydrates in the presence of water at elevated temperatures (140 - 220 °C) in a closed autoclave system mimicking the natural coalification over short reaction times (*e.g.* ~ 12 hours).<sup>[5]</sup> In a closed autoclave system self-generated pressures of *ca.* 10 bars are achieved during the synthesis. Compared to other carbonisation processes, these are comparatively mild conditions compatible with the standards of sustainable chemistry.<sup>[2]</sup> If a pure carbohydrate solution is used, the resulting carbonaceous product is rather hydrophilic and typically composed of micron-sized spherical particles. From the thermodynamic point of view the overall process is exothermic, inducing potential for technological usage.<sup>[3]</sup> Importantly, the starting carbon content is mostly retained within the non-volatile product, making stored hydrothermal carbon a potential synthetic carbon sink to counteract global warming.<sup>[5]</sup> Compared to microbiological degradation, the natural fate of biomass, which mainly produces CO<sub>2</sub>, this is highly advantageous. Ideally the production of useful functional carbonaceous materials, called “designer coals” could be achieved leading to the simultaneous benefits of carbon storage and also for application-oriented carbon material design.

There are already well-established methodologies allowing a high level of structural control for the production of carbonaceous nanostructures with various morphologies such as ellipsoids<sup>[6]</sup> and nanowires.<sup>[7, 8]</sup> As a consequence hydrothermal carbon hybrid materials (*e.g.* carbon nanocomposites), have shown promise in fields of tremendous importance including energy conversion<sup>[9]</sup> and storage,<sup>[10]</sup> sorption<sup>[11]</sup> or catalysis.<sup>[12, 13]</sup> Although there are a number of examples presenting the successful conversion of “real” biomass / biowaste (*e.g.* sugar beet chips, pine cones, pine needles, oak leaves, orange peels and prawns)<sup>[3, 14]</sup> into hydrothermal carbon, the previously mentioned applications have been accomplished with materials produced from purified sugars. Obviously, there is still a big challenge in using crude biomass products coming directly from agricultural biowaste. Additional natural ingredients present in



carbohydrate - rich biomass typically interfere with the carbonisation process leading to less desirable products. The development of methods for turning these compounds (*e.g.* inorganic substrates<sup>[14]</sup>, lignin<sup>[15, 16]</sup> or proteins<sup>[17, 18]</sup>) into advantageous “additives” or “templates” for the resulting carbon materials is currently ongoing, although they still remain rather generic and are not yet marketable. Additionally, for most technology relevant applications (*e.g.* heterogeneous catalysis, electrodes, sorption *etc.*) high surface areas and porosity are essential. In this context bottom - up approaches using metal salts,<sup>[7]</sup> surfactants,<sup>[13, 19, 20]</sup> hard templates<sup>[21]</sup> and other additives<sup>[10]</sup> have successfully resulted in the formation of nanostructured carbon or carbon composite materials demonstrating their general feasibility. However, there is still no simple route which allows subtle control over textural properties (*e.g.* surface area) and the ability to tailor pure hydrothermal carbon without structural backbones such as hard and soft templates. A protein - directed approach to porous nitrogen - doped hydrothermal carbon was developed and concurrently to this thesis successfully expanded to nitrogen - doped hydrothermal carbon aerogels within our group.<sup>[17, 18]</sup>

To put the current topic in context, the hydrothermal treatment of carbohydrates was scientifically investigated already in the mid of the 19<sup>th</sup> century. Hydrolysis of carbohydrates into sugars and their decomposition into humic acids and formic acid was reported.<sup>[22]</sup> In 1913 Bergius simulated the natural coalification of cellulose *via* hydrothermal treatment.<sup>[23]</sup> Since the energy crisis in 1973 renewed interest has appeared in the acidic hydrolysis of carbohydrate biomass and Bobleter *et al.* has shown that in a dynamic process, the yields of solubilised biomass by hydrothermolysis at neutral pH could be substantially increased.<sup>[24]</sup> Bobleter *et al.* were able to classify hydrothermolysis as existing between already well - established acidic hydrolysis and alkaline degradation of carbohydrates. It was found that the cleavage of glycosidic bonds in polysaccharides under hydrothermal conditions has an H<sup>+</sup> and OH<sup>-</sup> independent region (approximately between pH 3 and 7) and therefore has to be distinguished from the aforementioned processes.<sup>[24]</sup> However, it also combines features of both processes supported by following facts:

- a) Lobry de Bruyn - Alberda van Ekstein rearrangement (glucose ↔ fructose) occurs extensively during alkaline and hydrothermal treatments, but sparingly in acidic media;
- b) The degradation products hydroxymethylfurfural (HMF) and furfural are major reaction products in acidic and hydrothermal reactions, but are practically absent during alkaline treatment.

Interestingly, under hydrothermal conditions the isomerisation of glucose to fructose appears, while the other direction can be neglected.<sup>[25-27]</sup> Sugar decomposition under subcritical aqueous conditions happens *via* dehydration and retro - aldol condensation.<sup>[27]</sup> At lower temperatures of < 350 °C dehydration is favoured.<sup>[28]</sup> Of the dehydration products, furfural is generated from pentoses, such as xylose and ribose, whereas HMF is obtained from hexoses, such as glucose, fructose and mannose. Glucose is the most abundant sugar unit in biomass. Therefore, it is the major product of acidic hydrolysis of carbohydrate biomass.<sup>[28]</sup> In order to produce HMF from the acidic treatment of biomass e.g. glucose, additional dehydration catalysts have to be applied. In hydrothermolysis HMF is directly the main product. Without catalysts HMF is preferably derived from dehydration of fructose and not from glucose directly.<sup>[29-32]</sup> The need of catalysts in acidic hydrolysis, while the hydrothermal process directly converts biomass to HMF confirms the effective Lobry de Bruyn - Alberda van Ekstein rearrangement (BER) under hydrothermal conditions. Since HMF is one of the most promising biomass - derived, petrochemical replacement platform chemicals, significant research has been conducted to investigate the effective production of the reactive furane derivative.<sup>[25-27, 29-31, 33-35]</sup> The main challenges are to find proper catalysts to optimise selective dehydration and fast extraction of HMF from an aqueous reaction medium, which promotes HMF decomposition. With increasing reaction time in aqueous medium, HMF successively decomposes into levulinic acid (LA) and formic acid (FA) on the one hand and into polymeric carbonaceous material on the other hand.<sup>[26]</sup> Whilst most people have tried to avoid such resinification or hydrothermal carbonisation of biomass - derived sugars and consequently HMF, Antonietti and others rediscovered the process in the sense of Bergius, for the production of green and valuable carbon and carbon hybrid

materials.<sup>[3, 23, 36-38]</sup> Depending to a large degree on the applied conditions (*i.e.* the grade of carbonisation), the products are called humines,<sup>[39]</sup> hydrothermal carbon<sup>[2]</sup> or hydrochar.<sup>[40]</sup> As mentioned above, carbonaceous materials prepared at 140 - 220 °C are called hydrothermal carbon (HTC). As the most abundant and therefore most interesting biomass - derived sugar is glucose, the majority of research has been concentrated on the respective decomposition towards HTC (Figure A1). Since herein the focus lies on hydrothermal carbon, the formation of hydroxylbenzenes and retro - aldol products, which has been extensively reported to occur at higher reaction temperatures, is not considered.<sup>[28, 41, 42]</sup> However, these compounds should also play a minor role in the formation of HTC. A broad overview on biomass transformation and the various decomposition products depending on the actual subcritical water conditions was recently provided by Möller *et al.*<sup>[43]</sup>

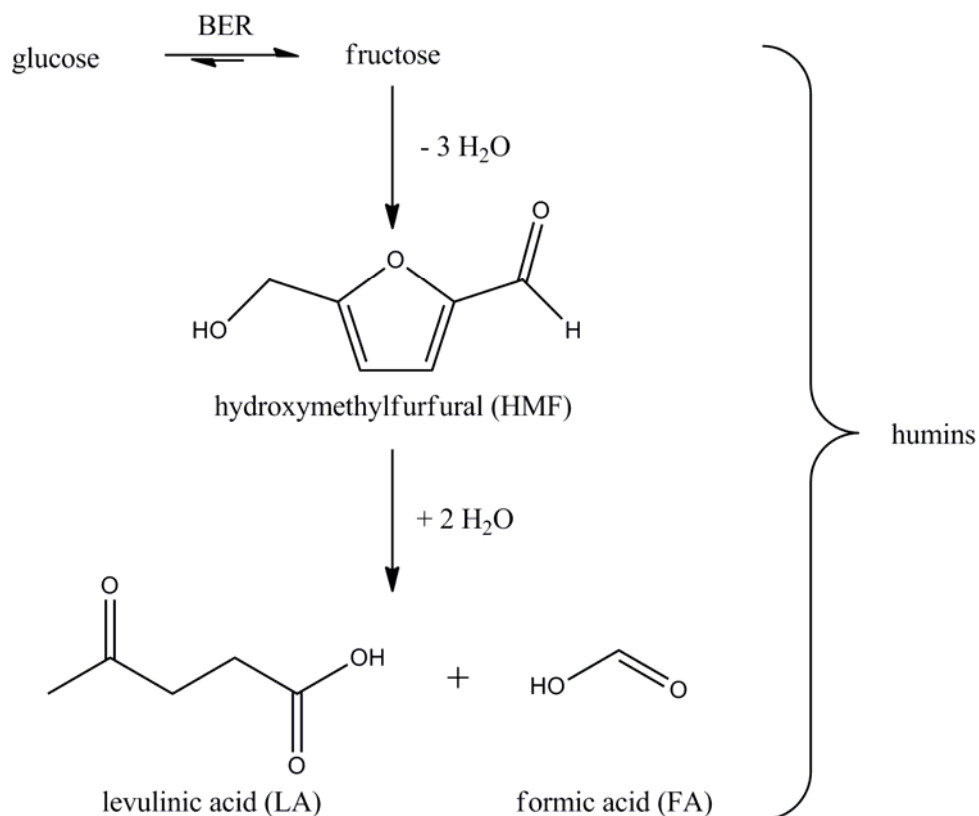


**Figure A1:** Hydrothermal reaction scheme of glucose

## A1 Reaction Pathway of the Hydrothermal Carbonisation

HMF can be considered to be the main precursor for the generation of HTC from the model monosaccharide glucose. To understand the chemistry of HMF one has to regard the well - known furan chemistry (Figure A2).

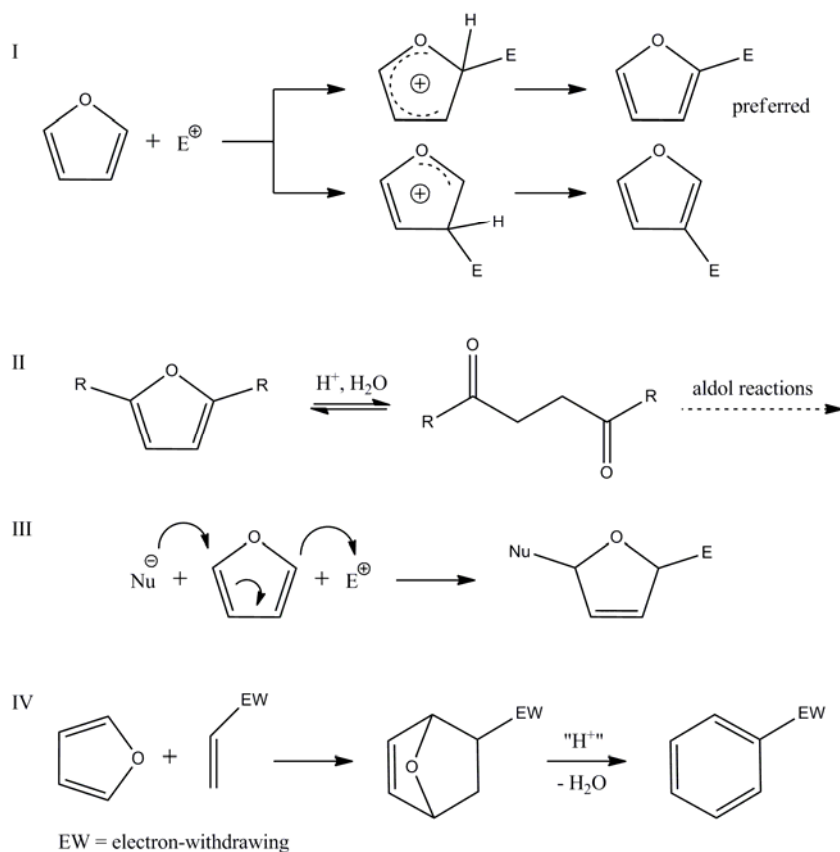


**Figure A2:** Overview of furan chemistry

Furan is a five - membered heterocyclic aromatic compound, with a ring composed of one oxygen and four carbon atoms. The aromatic resonance energy is low compared to benzene and the electron density within the ring exceeds that of benzene due to the electron - donating effect of the oxygen. Consequently, furan shows high reactivity ( $10^{11}$  times higher than benzene) towards electrophilic aromatic substitution reactions, which are preferred in the 2,5 - position (Figure A2/I). The high electron density and low resonance stabilisation lead to a manifold of electrophilic addition and ring - opening reactions compared to other aromatic compounds. As acid catalysed ring - opening

reactions lead to diketones, furans can also be viewed as masked diketones (Figure A2/II). Diketones, possessing  $\alpha$  - hydrogens can easily undergo inter- and intramolecular aldol - type reactions induced by keto - enole tautomerism. Due to the rather weak conjugation of the oxygen atom, furans can also undergo nucleophilic addition reactions, behaving like a 1,3 - butadienes (Figure A2/III). The resulting adducts can be easily converted by nucleophilic substitution. Additionally, the 1,3 - diene substructure fixes the ring in a s - cis - position, a perfect diene component setup for Diels - Alder reactions (Figure A2/IV). Diels - Alder products can subsequently be transformed into classical aromatic compounds.<sup>[44]</sup>

Naturally, the substitution pattern of the furan ring, as well as reaction conditions can drastically influence its reactivity. Recently, a significant quantity of research effort has focused on the chemistry and transformation of HMF. Lewkowski reviewed aspects of synthesis and chemical conversions of HMF in 2001.<sup>[45]</sup> Very recently Rosatella *et al.* reviewed the broad field of biological properties, synthesis and synthetic applications of HMF.<sup>[46]</sup> Both articles describe a manifold of reaction mechanisms taking into account reactions on the hydroxymethyl group (*e.g.* esterification, etherification and oxidation) and the formyl group (*e.g.* reduction, oxidation, aldol- and aldol - like reactions). The general aim, however, is the preparation of symmetric compounds for the use as monomers in sustainable polymer synthesis. Investigations on the oligo- / polymerisation of HMF are still scarce. As will be discussed later, Gandini *et al.* carried out a lot of work on furan - based polymers.<sup>[47-49]</sup> They also reported on Diels - Alder reactions in that context. In order to distinguish HMF from furan and achieve insight into the corresponding glucose – based hydrothermal carbonisation process, the chemistry of the respective functional groups has to firstly be considered. The highly reactive formyl group can be attacked by several nucleophiles (Figure A3). One of the most important reactions of aldehydes is the aldol condensation with  $\alpha$  - carbonyl compounds, such as diketones (Figure A3/A). In the presence of alcohols, aldehydes are transferred into acetals (Figure A3/B). In case of vicinal diols *e.g.* sugars, dioxolanes can be formed. Such reactions are well known within the chemistry of sugars. The reversible formation of dioxolanes is often used to protect the reactive aldehyde group. Interestingly, the acetalisation changes the reactivity of the furan ring in HMF, as it blocks the negative

mesomeric effect of the electron withdrawing formyl group and therefore increases the electron - density within the ring.

The hydroxyl group of the hydroxymethyl substituent can undergo simple nucleophilic substitution acting as leaving group (Figure A3/C), as well as etherification / esterification in the presence of alcohols / carboxylic acids (Figure A3/D). It is noteworthy that acetalisation promotes the leaving group reactivity of the hydroxyl function *via* the increased electron density within the ring and the stabilisation of the resulting primary carbocation. The carbocation (Figure A3/E) can undergo electrophilic substitution reactions at nucleophilic furan rings (Figure A3/F).

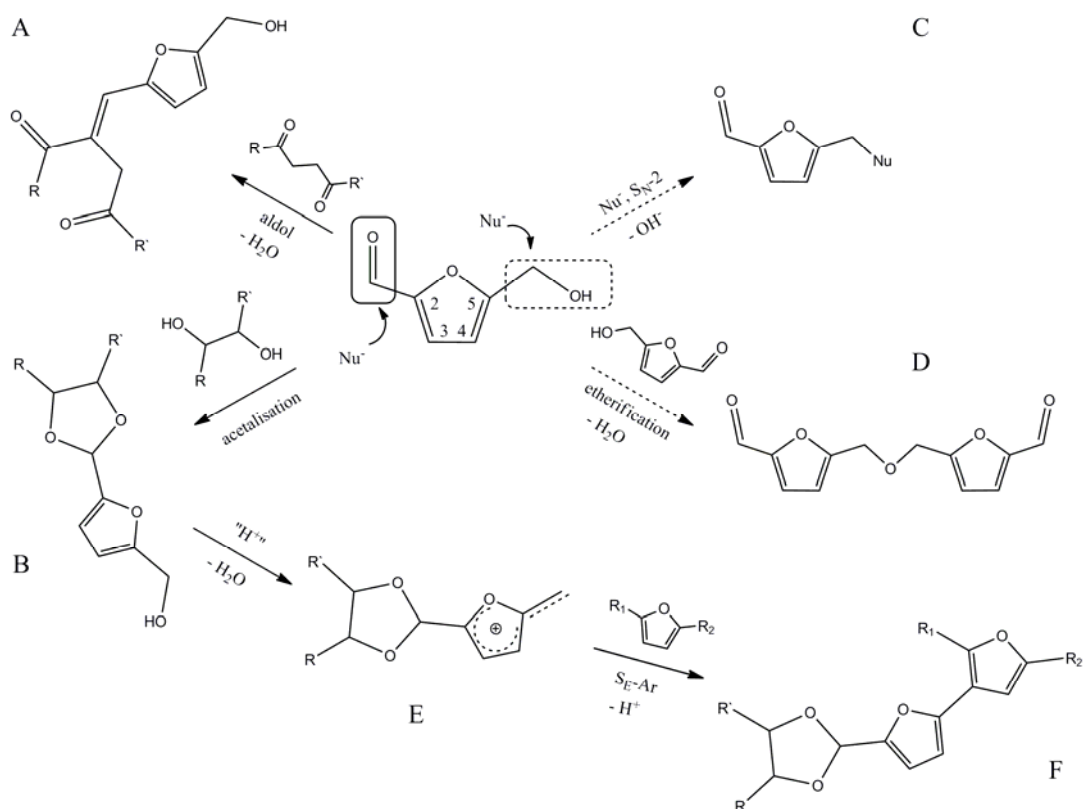


**Figure A3:** Selection of HC - relevant reactions at the substituents of HMF and acetal - protected HMF

Secondly, the effects of substituents on the chemistry of the ring need to be considered (Figure A4). Electron - withdrawing substituents will reduce electrophilic attacks on the ring (Figure A4/I). This is especially the case as the hydroxymethyl- and the formyl - group of HMF are located at the preferred 2,5 - positions. Instead, nucleophilic addition reactions are more favoured due to the previously mentioned

resonance effect with the formyl group (Figure A4/II). However, the substituents are even more reactive towards nucleophilic addition / substitution and may compete with reactions at the ring, also due to sterical restraints at the 2,5 - position. The addition of water and subsequent ring - opening leads to the formation of levulinic acid and formic acid in hydrothermolysis (Figure A4/III).<sup>[50]</sup> This indicates the strong involvement of such ring - opening reactions, which can convert furans into diketones.<sup>[32]</sup> In turn,  $\alpha$  - H - diketones give rise to versatile aldol chemistry (Figure A4/III).

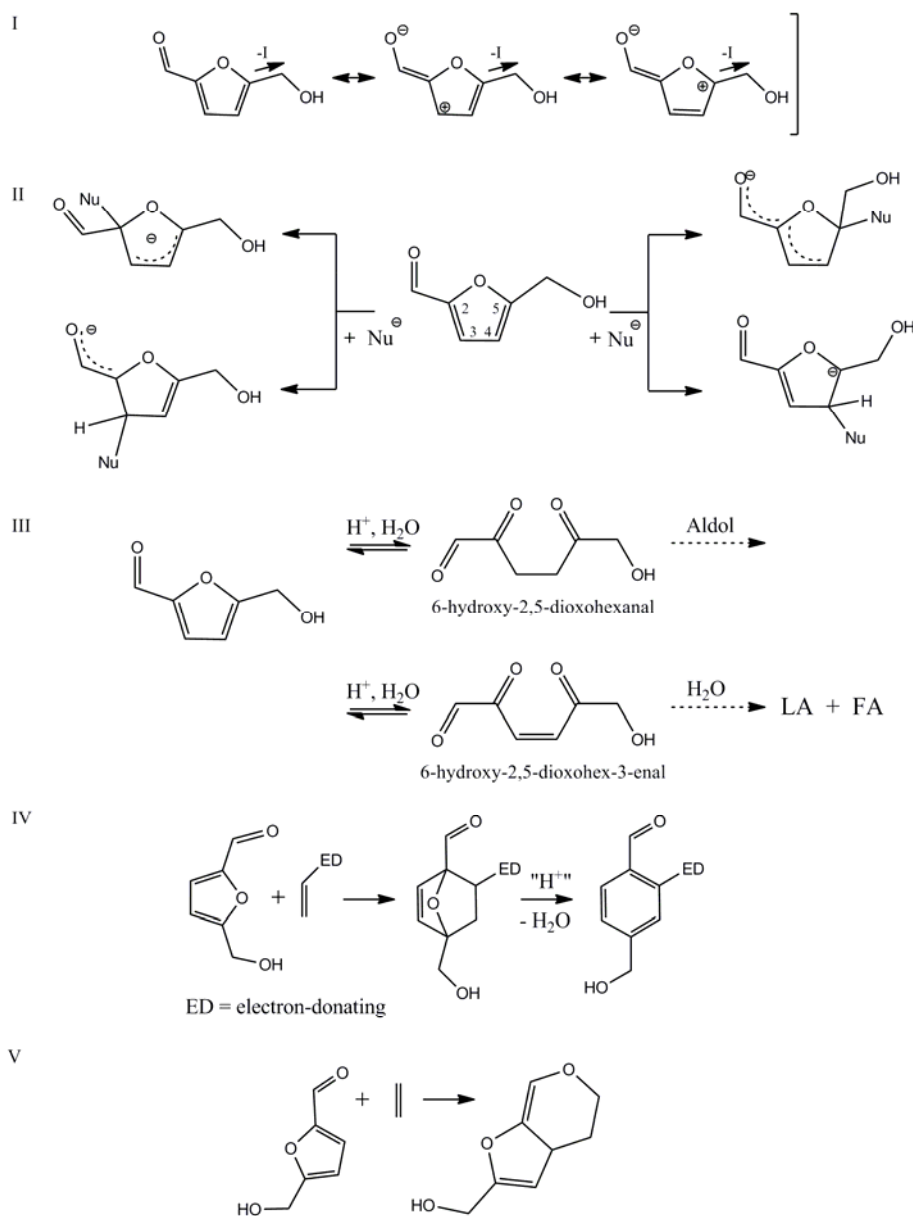


**Figure A4:** Selection of possible HC - relevant reactions at the ring of HMF

In the context of Diels - Alder reactions, the diene substructure of HMF changes from an electron - rich diene like furan, to a more electron - poor diene, which consequently rather prefers the reaction with electron - rich dienophiles (Figure A4/IV). Notably, the formyl - group in HMF is located in  $\alpha$  - ene position and therefore creates another diene substructure, which might also undergo cycloaddition reactions (Figure A4/V). Pressure and temperature additionally influence the reactivity, particularly in Diels - Alder reactions, which generally are exothermic and have a negative reaction volume. Water as solvent, can be favourable for Diels - Alder reactions of rather hydrophobic reactants and it is also known to accelerate reactions with ionic transition states like aldol reactions.<sup>[51]</sup>

Unfortunately, there is still not much literature on the mechanism of formation of the insoluble polymeric species appearing during the hydrothermolysis of carbohydrate biomass. In the majority of papers dealing with this topic, the occurrence of soluble polymers and insoluble humins is mentioned. Although the formation of these species lowers yields, and therefore limits the efficiency of the desired process, reports on the composition or building mechanism in these papers remain rare. A lot of research has given only unsatisfactory results, mostly because the proposed linear condensation products are expected to be colourless thermoplasts instead of the obtained black duroplasts. This curiosity hints to the complexity of the “side” reactions, especially as most of the mentioned processes start from rather homogeneous if not single precursor solutions.

The chemistry of mono - substituted furans, which either possess the hydroxymethyl- (furfuryl alcohol) or the formyl - function (furfural) is comparably well investigated. Self - condensation, sometimes called resinification, of furfural and fururyl alcohol under non - aqueous conditions is also reported. Gandini *et al.*, a major contributor to the study of furan - based polymerisation, have explained the difficulties in understanding the mechanism of poly - furfuryl alcohol with two side reactions, namely hydride abstraction and intramolecular Diels - Alder reactions. Alternating  $H^- / H^+$  abstraction cycles at methylene bridges of the oligo(furfuryl alcohol) lead to a conjugated linear polymer. Dihydrofuran moieties are then likely to react as dienophiles with the diene substructure of furans to produce the typical cross - linked resins. Using this model,



Gandini *et al.* also explained the colour generation of the branched polymer by highly conjugated sections within the resin.<sup>[47, 48, 52]</sup> Under acidic and aqueous conditions the proposed polymerisation and cross-linking scheme, leading to the resinification of furfuryl alcohol, probably also involves diketone formation within the polymer chain (Figure A5/A). This happens *via* ring-opening reactions, which are thermodynamically slightly favoured.<sup>[53]</sup> Attention has to be drawn to the possibility of converting the ether bridge in oligo- / poly(furfuryl alcohol) into a methylene bridge by the release of formaldehyd. Etherification is expected from HMF as well (Figure A3/D). Therefore this mechanism is likely to contribute to the formation of HTC. However, due to the formyl group, the reactivity of HMF should be closer to furfural, where the “resinification” is even more complicated and less understood. Different resin precursors were found by simple thermal degradation of furfural at 100 - 250 °C (Figure A5/B). Both together lead to cross-linked precipitates and it is proposed that charge stabilisation in the conjugated systems may lead to the dark colouration.

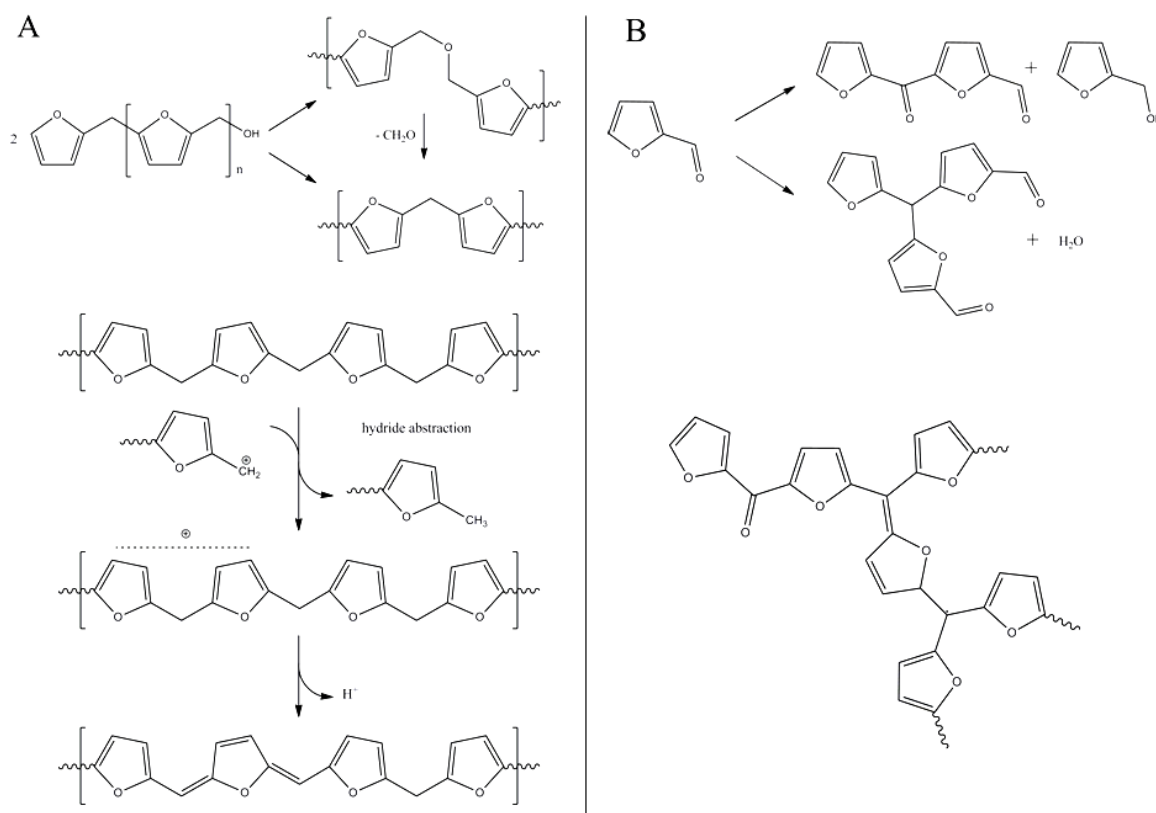


**Figure A5:** Resinification schemes of A) furfuryl alcohol and B) furfural (adapted from <sup>[52]</sup> and <sup>[54]</sup>)

Radical reactions as well as reactions involving the release of hydride ions have also to be considered under the hydrothermal conditions. It is reported that HMF, which does not possess a free 2- or 5- position, is hardly sensitive to this anhydrous resinification reaction.<sup>[48]</sup> Additionally, the presented “resinification” products are clearly to be distinguished from the respective hydrothermal carbon as ring - opening reactions were avoided by anhydrous conditions. Titirici *et al.* used furfural as the precursor for the production of mesoporous carbons using silica hard templates as structure directing agents, and hydrothermal carbonisation was reported to be a preconditioning step prior to pyrolysis, leading to formation of stable material, which could withstand the silica removal procedure.<sup>[55]</sup> The presence of water at high temperature strongly changes the reactivity of the furans to form solids, as herein the reactivity is HMF > furfuryl alcohol >> furfural. It is very likely that this change is related to ring - opening reactions. Accordingly, HMF and furfuryl alcohol are industrially used precursors for the production of the linear levulinic acid / levulinic acid derivatives, whilst furfural is not.<sup>[54, 56]</sup>

The large variety of different reaction conditions (pH, temperature and pressure) and reaction mixtures, composed of unequal amounts of sugar, organic and inorganic additives, leads to unpredictable reactivity and complicates the search for a “general” reaction scheme. However, possible pathways, which are likely to occur in certain quantities depending on the actual situation, and their consequences on the final materials, can be proposed. Employing solid - state NMR techniques, Baccile *et al.* discussed the structure of glucose - based HTC derived at 180 °C for 24 h. In contrast to formerly proposed models of core - shell particles with an aromatic core and oxygen - rich shell,<sup>[40]</sup> a furan - based structure was concluded. Accordingly, a branched polyfuran type of network with aliphatic ketone linkers and embedded levulinic acid is the proposed structural model. The furans are mostly 2,5 - disubstituted, building a linear polymer chain backbone, but are also cross - linked at the 3,4 - positions. Long range double bond conjugation, as occurs in classical aromatic systems was reported in medium abundance. A low appearance of formyl, carboxyl and methyl end groups was also indicated. However, a relationship between the proposed material structure (*e.g.* composition /

conjugation) and the inherent brown / black colouration of the hydrothermal carbon was not discussed. Unfortunately, a discussion on the reaction pathway and an explanation of the appearance of hydroxyl - functions, as observed by FT - IR spectroscopy, is still missing but will be addressed in the following section.

Oligomerisation / reversion of hexoses is known to occur at mild conditions, but is successively displaced by the formation of HMF with increasing temperatures.<sup>[57]</sup> Hydrothermal treatment of pure fructose and of pure HMF leads to different soluble polymeric species.<sup>[26]</sup> This suggests reactions between HMF and its decomposition products with sugar. Even if NMR studies suggested the composition of the respective final HTC to be equal, different pathways may influence the final product morphology.<sup>[2]</sup> This is also indicated by differences in particle size starting from pure HMF or from sugar.<sup>[5]</sup> In the industrial formation of furfural from pentoses, not the whole sugar is converted to furfural. An important yield lowering reaction is known to be the acetalisation of pentoses with furfural.<sup>[54]</sup> Acetal formation from HMF with glucose and / or fructose, as well as intermediate diols can be expected. Indeed, HC of equimolar amounts of HMF and a HMF / glucose mixture at 180 °C for 11 hours lead to different solid yields (yield (HMF) > yield (mixture)), although the time scale of dehydration are minutes.<sup>[58]</sup> As mentioned before, the acetalisation partially reduces the reactivity of HMF due to protection of the aldehyde group. The increased electron density of the ring increases the reactivity of the hydroxyl group, which can undergo etherification or dissociation leading to substitution in the 3,4 - position of other furans. Obviously the formyl group affects the reaction rate more. Furthermore ring - opening reactions create diketones like levulinic acid which can easily undergo aldol condensations. Horvat *et al.*, have studied the formation of levulinic acid, and conclude that instead of a 2,3 - addition of water, which would lead ultimately to levulinic acid, the 4,5 - water addition should also occur. The proposed pathway of Horvat *et al.*, most likely would produce 2,5 - dioxo - 6 - hydroxohexanal (Figure A4/III), which was meant to start the formation of a polymeric species.<sup>[50]</sup> Patil *et al.* recently followed this expectation to explain the formation of humins at mild conditions, *via* aldol addition and condensation, using IR spectroscopy.<sup>[39]</sup>

Together, substitution and condensation are polymerisation reactions. Regarding the previously mentioned solid state NMR results, which suggested furans to be mostly 2,5 - substituted, aldol condensation and to a less extend etherification can be considered to be the most important reactions. Therein, diketones will react with the very reactive aldehyde function of HMF and with other diketones to form linear polymers. Ring – opening reactions of added furans and further aldol reactions may lead to cross – linking. Etherification can enhance the branched character of the product. As reported for poly(furfuryl alcohol), loss of formaldehyde converts ether bridges into methylene bridges. Deprotonation and dehydroxylation, as well as alternating H<sup>-</sup> / H<sup>+</sup> abstraction can create conjugated networks, which explain the dark colouring of HTC material. The dihydrofurans present within the conjugated network and double bonds from aldol condensations give rise to Diels - Alder reactions with the inherent *s* - cis diene substructure of furanes, creating further cross - linking and additional aromatic structures. This is especially the case when nitrogen - containing additives, such as proteins and amino acids are involved.

In summary, we can speak of a set of dehydration, polymerisation *i.e.* condensation and addition as well as aromatisation reactions, which lead to the final chemical structure of HTC (Figure A6, reaction pathway in the Appendix). Regarding the overall scheme, it has to be mentioned that Diels - Alder reactions for HC of pure sugar will probably play a minor role, but will be enhanced by nitrogen - containing additives, which can react with carbonyl compounds to intermediately form imines, finally leading to increased aromaticity.

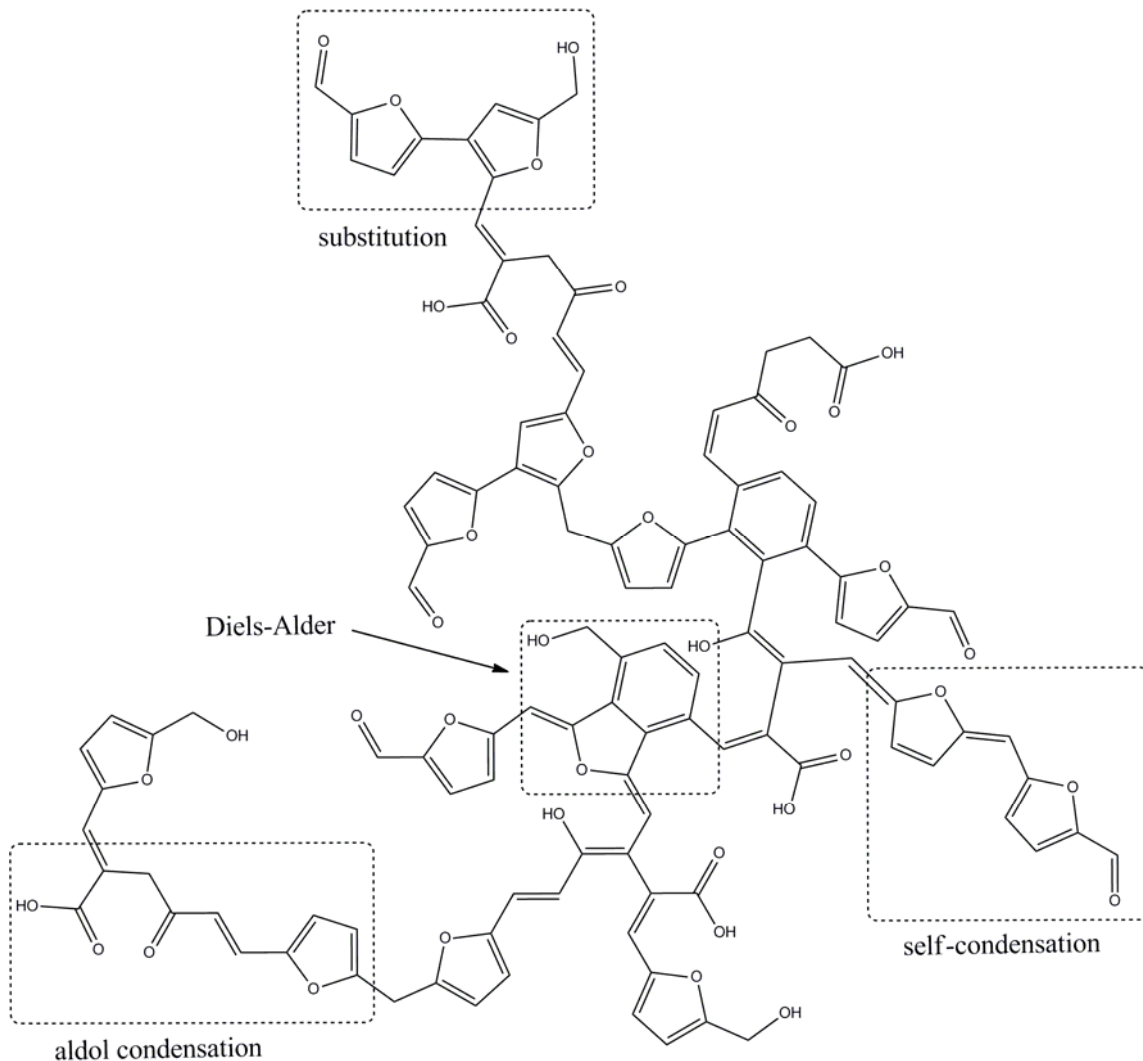


**Figure A6:** Model substructure of HTC. The reaction pathway involves etherifications with subsequent loss of formaldehyde, electrophilic substitutions, aldol condensations,  $H^+$  /  $H^-$  abstractions and Diels - Alder reactions.

One challenge is to understand the chemistry behind the hydrothermal carbonisation, in order to develop tools *e.g.* for the manipulation of the reaction process depending on the application targets. Similarly with regard to applications, a second great challenge is controlling the morphology of the hydrothermal carbon. The hydrothermal carbonisation is reminiscent of a very famous bottom - up approach to synthesise micron - sized carbonaceous materials: the polycondensation of resorcinol formaldehyde (RF) mixtures towards the respective resins with subsequent carbonisation.<sup>[59]</sup> The two main reaction steps, namely (1) building a reactive precursor followed by (2)

polymerisation, and the comparable particle morphology generated in water as solvent, indicate mechanistic similarities for the respective material formation (Figure A7).

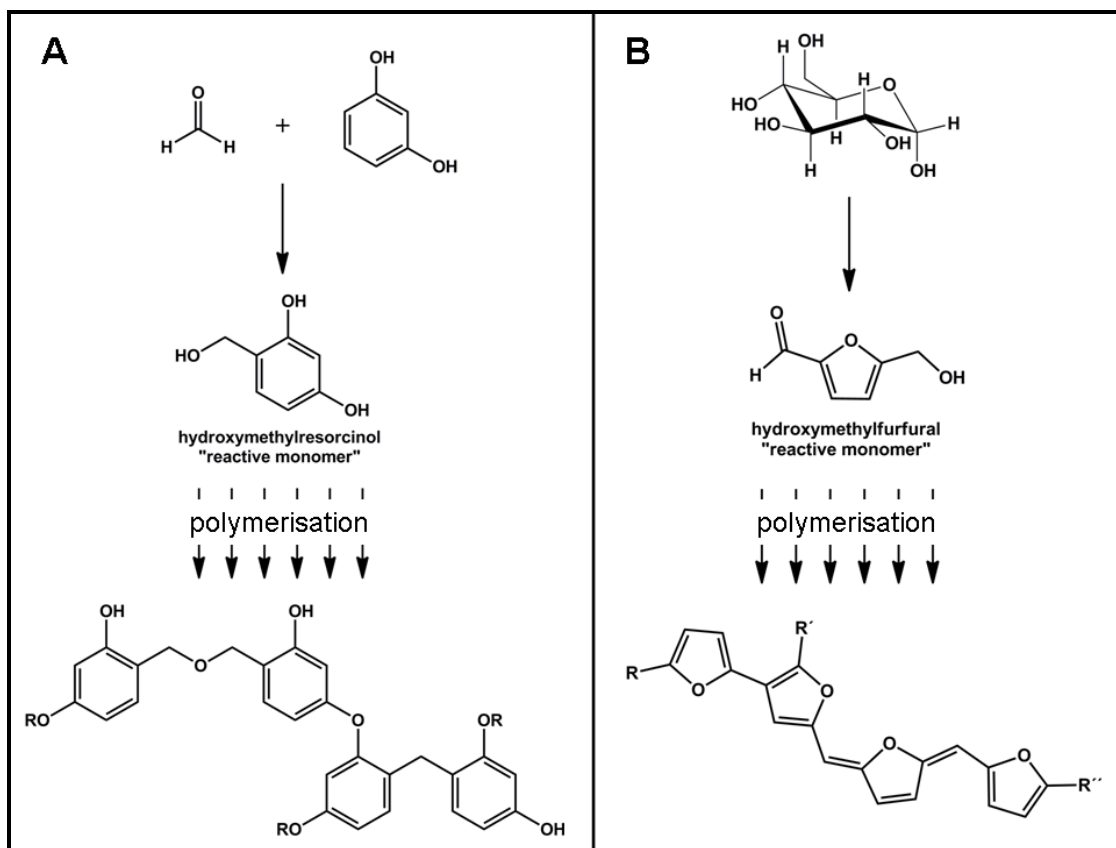


**Figure A7:** Two - step reaction as precondition for resinification chemistry in “classical” RF system (A) and schematic HC system (B).

Without doubt, the classical RF polycondensation, occurring at comparatively low temperatures, has certain advantages. Nevertheless, when comparing both processes the sustainability of the HC process has to be emphasised, since all precursors in the RF system are harmful and not produced in a sustainable fashion. Additionally, RF resins show restricted chemical variability leading to limitations in their potential uses. In the structural context, it is interesting that RF - based resins in aqueous solution tend to form gels due to the interconnection of growing particles. In contrast, the very similar phenol / formaldehyde (PF) system forms precipitates composed of separated spheres similar to standard HTC products. The curiosity can be explained by the stronger interaction of RF resins with water, originating from the larger amount of hydroxyl

functions, which allows the well - dispersed particles to condense throughout the whole reaction mixture.<sup>[59, 60]</sup> However, the scheme for HC represents a very simplified mechanism, which can only be used to explain the formation of morphological characteristics of the final material. RF resins are found with a chemically well - defined connectivity, which depends on the pH during the synthesis. In contrary, the connectivity in HTC is much more versatile and allows for the possibility of achieving very different properties by chemical or physical (post-) modification, making the material interesting as sorption material for different purposes, such as filters or chromatography columns. At the same time the versatility of the process complicates the full understanding of the system, making it difficult to rationally modify the *in - situ* process. Since the most abundant chemical moiety in HTC is the furanic double bond, *in situ* - cycloaddition reactions were addressed to modify the functionality of hydrothermal carbon.<sup>[11, 61]</sup> Using this approach, highly efficient sorption materials for the removal of heavy metals from wastewater have been produced.<sup>[11]</sup> This method demonstrates the potential of easily obtaining functional CO<sub>2</sub> - negative carbonaceous materials using the HC process by simple adjustment of chemistry. However, the employment of real biomass would be beneficial and it can be expected that sorption capacities are still limited due to the large diameter, non - porous HTC particles. An increase of the specific surface area is therefore highly desired as it would not only enhance sorption capacities of the inexpensive and green material, but also open a wide field of further applications.

## A2 The Hydrothermal Carbonisation of Glucose, Catalysed by Borax

The previously described similarity of HC, as essentially being a resinification product of HMF under hydrothermal conditions, with the formation of resorcinol formaldehyde resins, suggests the validity of sol - gel concepts, such as the explanation of particle growth according to the LaMer diagram. Following the implications of LaMer, numerous sol - gel synthesis routes lead to monodisperse particles, given that an initial supersaturation of nucleating species, leading to the generation of seeds, is avoided in the following.<sup>[62]</sup> Continuous feeding of monomer to a fixed number of seeds allows uniform growth and therefore the desired monodispersity. If we apply the LaMer model to HC, we have to consider that for practical reasons no continuous feeding is achieved. A certain concentration of sugars is set before the autoclave is sealed. In principle, employing poly-/oligosaccharides with different hydrolysis kinetics at the same time could create such a system in HC, but cannot be considered as a worthwhile method.

Another implication of the LaMer diagram is exploited in nanoparticle synthesis in order to obtain very small particles. The stronger the supersaturation the more seeds are formed, under rapid depletion of the precursor concentration, leading to a smaller overall particle size. One way to induce this pathway is the so - called *hot injection technique* or shock precipitation, where a very fast temperature increase provokes the formation of highly concentrated, reactive species, leading to the formation of many seeds.<sup>[62]</sup> HMF is the reactive species in HC and its concentration should affect the number of “*seeds*”. Indeed, carrying out hydrothermal carbonisation from pure HMF leads to much smaller particles (~ 160 nm for 10 % solution, 180 °C and 16 h)<sup>[5]</sup> Unfortunately, up to now it was not possible to achieve such small particles *i.e.* high surface area from the hydrothermal carbonisation of carbohydrates, remaining one of the main challenges in the field.

In sol - gel synthesis, the same general effect of *hot injection* can be obtained by the employment of catalysts, for the accelerated formation of reactive species. The aforementioned PF system represents a valid example for this pathway. Herein, the formation of small particles occurs through the catalysed polycondensation of the reactive precursors in water.<sup>[60]</sup> While reactions free of catalyst lead to precipitation of



micrometer sized particles,<sup>[63]</sup> a material composed of significantly smaller particles can be achieved either by acid or base catalysis. The molar ratio of phenol to catalyst allows the control of the final particle size, basically by adjusting the number of “seeds”.<sup>[64]</sup> The more catalyst is used, the smaller the final particle size. In the case of the equivalent (RF) system, even more interesting materials are achieved due to gelation throughout the whole reaction mixture (Figure A7). Low density organic aerogels, which can be converted into conductive carbon aerogels, can be produced this way. At constant precursor concentration the particle size (*i.e.* specific surface area and porosity) can be controlled by adjusting both the amount of catalyst added and the solvent volume employed (Figure A8).

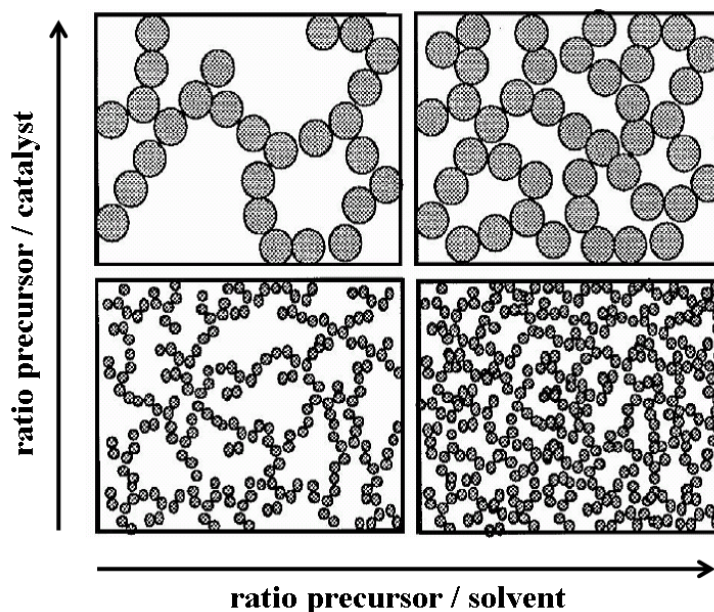


**Figure A8:** Structural trends of the resorcinol formaldehyde (RF) system depending on the ratio of precursor to catalyst. (Adapted from reference <sup>[59]</sup>)

In the context of catalysis, borates, (*e.g.* boric acid and borax) are well - known for their strong interaction with vicinal - dihydroxy compounds, such as glucose and fructose. Negatively charged borate - diol and borate - didiol complexes are formed which change the reactivity and physical properties of the sugar solutions.<sup>[65, 66]</sup> Investigations on the impact of borax representing borates on the hydrothermal carbonisation of glucose were therefore carried out and lead to highly interesting

observations: As an example, hydrothermal treatment of 20 ml of 30 % glucose solution with 500 mg of borax at 200 °C for 20 h resulted in the formation of dark brown, mechanically stable monoliths (Figure A9).

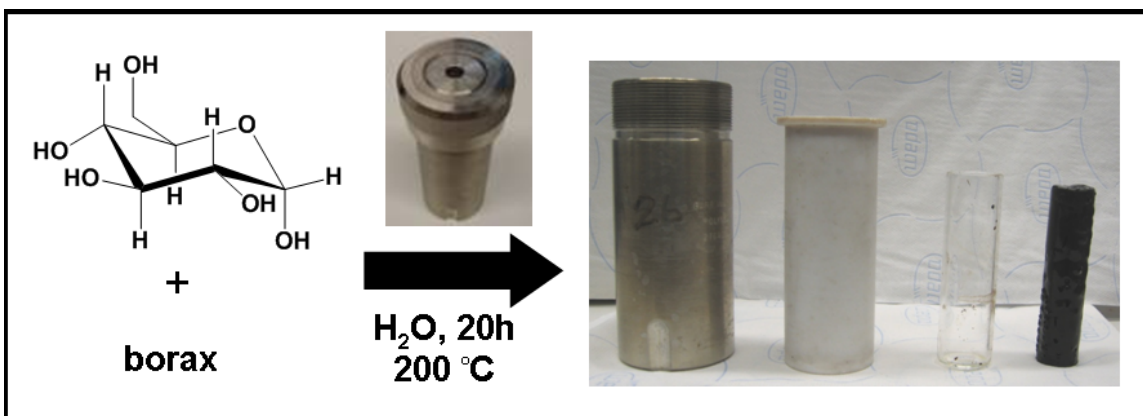


**Figure A9:** Scheme of the hydrothermal reaction of glucose in presence of borax resulting in a black monolith

SEM images revealed the monolith to be composed of aggregated nanometre sized spherical particles, leading to a colloidal hydrogel (Figure A10). Macro- and mesoporosity can be observed generating a lightweight carbon material exhibiting hierarchical porosity. After purification by extraction with water and ethanol, elemental analysis demonstrated a chemical composition similar to conventional HTC (*i.e.* ~ 64 % C; ~ 5 % H).

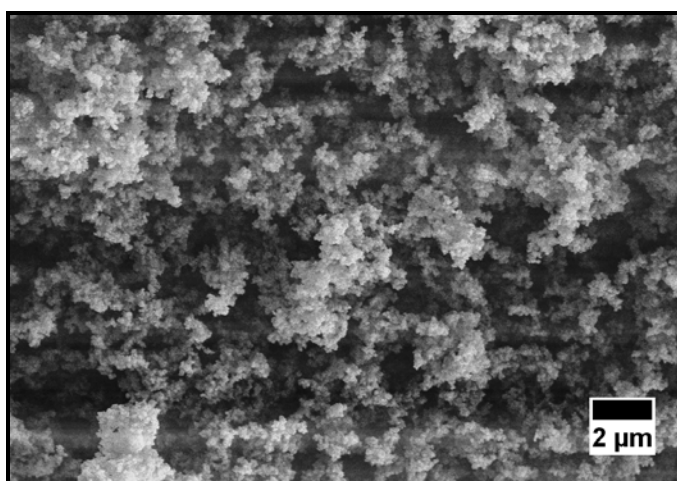


**Figure A10:** Scanning electron micrograph of the HTC monolith from glucose and borax

Considering that borax can be quantitatively removed after synthesis, whilst the gels retain their mechanical stability, the covalent cross - linking within the hydrothermal carbon must be promoted as well. FT - IR measurements confirms the very similar chemical composition of borax mediated HTC gels to classical glucose - derived hydrothermal carbon (Figure A11/left). Only the C = O band, representing keto- and aldehyde groups, shows an increased intensity. Supercritical drying was applied to retain the structure and minimise pore collapse for further investigations. Afterwards, nitrogen sorption measurements were carried out to investigate the porosity and evaluate the specific surface area by applying the BET method. The type IV - like nitrogen sorption isotherm is in accordance with the hierarchical porosity as observed *via* SEM (Figure A11/right)<sup>i</sup>. Together, a simple, inexpensive, and green route towards the production of porous, high surface area HTC was developed. With respect to high surface area / porosity being crucial properties for carbon applications, these results are of considerable importance for the concept of carbon storage and recycling employing HC.

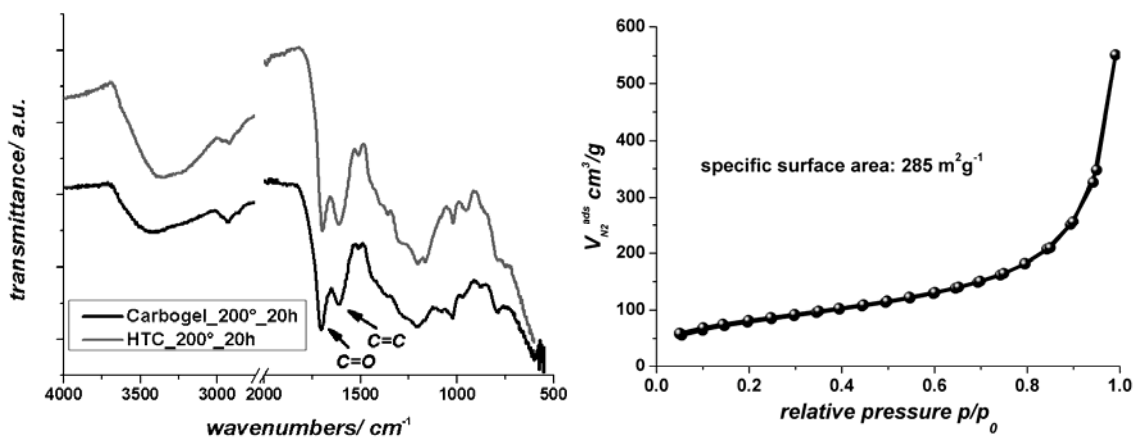


**Figure A11:** Comparison of FT - IR spectra of HTC monolith with reference HTC without borax (left) and nitrogen sorption isotherm of supercritical dried HTC monolith (right)

Since additionally the yield was clearly improved compared to hydrothermal treatment of pure glucose under the same reaction conditions, studies of the reaction time were carried out (solid yield improved from 26 % to 44 %, carbon yield from 42 % to 73 % for HC of 20 ml 30 % glucose solution at 200 °C for 19 h). 20 ml of 30 % aqueous glucose solutions with and without 500 mg borax were heat treated at 200 °C for 1, 2, 3,

<sup>i</sup> With the used nitrogen sorption parameters in this example, no hysteresis and therefore no pore-size information was obtained.

and 4 hours for comparison. Evidently the addition of borax, results in catalysis of the hydrothermal carbonisation of glucose (Figure A12).



**Figures A12:** Comparison of HC products from glucose with and without the addition of borax after different reaction times. Shown are results from 20 ml glucose solutions (30 %) with (cat.) and without (ref.) the addition of 500 mg of borax for 1, 2, 3 and 4 hours at 200 °C.

From these observations it can be concluded that mechanistically the role of borax in our system appears to be rather complex. The accelerated carbonisation by borax, (*i.e.* higher yields in shorter times with an onset at lower temperatures), could be explained by catalysis of glucose dehydration. Referring to the well - known reactivity of borax with sugars,<sup>[65, 66]</sup> one can expect that the interaction of borax with the vicinal diols leads to negatively charged boron - diol or boron - didiol complexes, enhancing the reactivity in the dehydration of glucose to HMF. Concurrently with the work presented in this thesis, Riisager *et al.* have presented a study describing the impact of boric acid on the hydrothermal dehydration of glucose, confirming the proposition that borax does in fact catalyse the dehydration of glucose.<sup>[30]</sup> A detailed study of the same working group proposes the catalytic activity to arise from the stabilisation of intermediates appearing within the isomerisation of glucose to fructose mediated by negatively charged boron - diol complexes (Figure A13),<sup>[67]</sup> with their results correlating with the lowered activation energy to the corresponding coordinated intermediate structures.

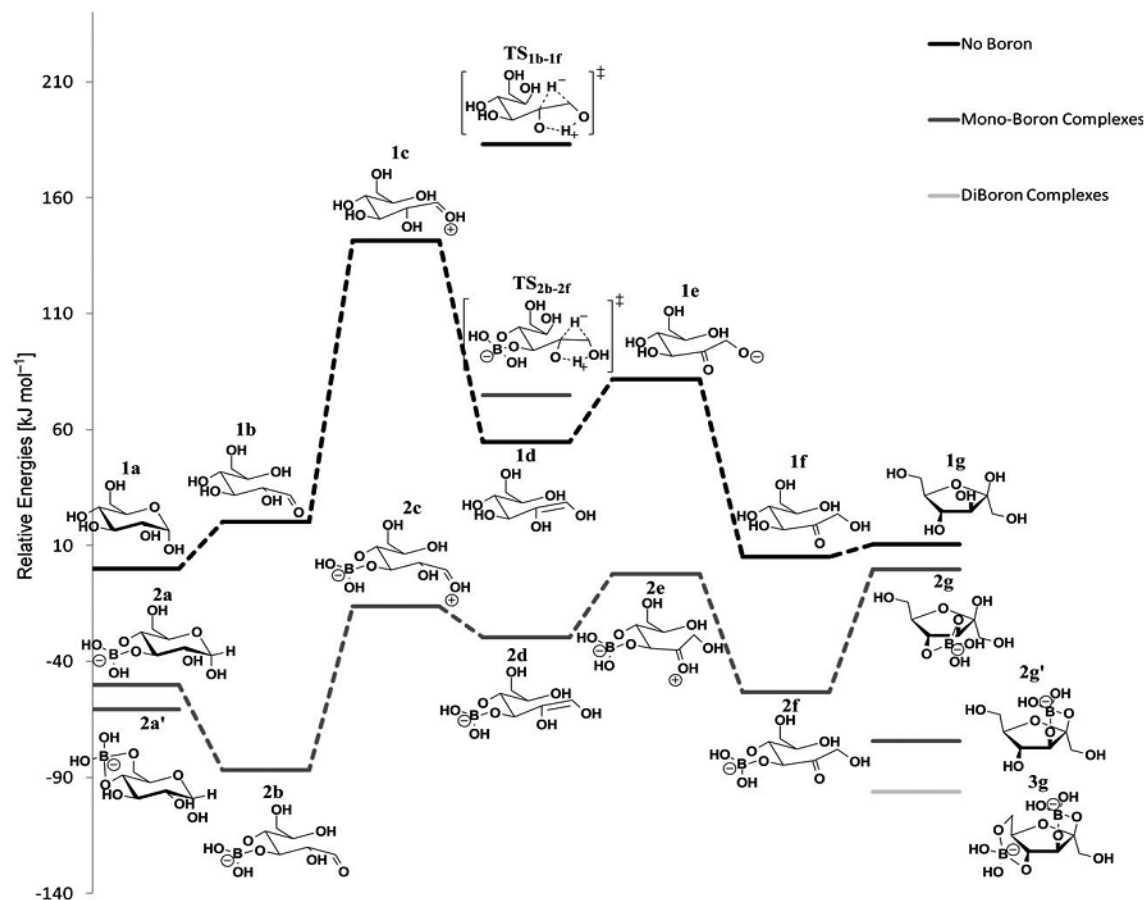


**Figure A13:** Thermodynamic inspection of the isomerisation of glucose into fructose depending on the presence of boron - diol complexes. (Inserted from reference<sup>[67]</sup>)

However, under hydrothermal conditions, the Lobry de Bruyn - Alberda van Ekstein isomerisation already converts glucose into fructose.<sup>[15]</sup> Compared to the dehydration of fructose, the hydrothermal carbonisation is a rather slow process and therefore should not be affected by the accelerated isomerisation. The fact that the particle size is even smaller as compared to HC of pure HMF corroborates this statement. To further investigate the role of borax, a HC system employing borax and fructose as precursor was investigated, whereby 20 ml of 30 % aqueous fructose solutions with and without 500 mg borax were heat treated at 140 °C for 2, 3, and 4 hours for comparison (Figure A14). It is clear that in this case, borax also accelerates the hydrothermal carbonisation of fructose. In addition to the improved dehydration of glucose, the subsequent carbonisation / resinification reactions are catalysed, as well.



**Figures A14:** Comparison of HC products from fructose with and without the addition of borax after different reaction times. Shown are results from 20 ml glucose solutions (30 %) with (cat.) and without (ref.) the addition of 500 mg of borax for 1, 2, 3 and 4 hours at 140 °C.

As mentioned before, particle aggregation indicates that borax also promotes cross - linking, which is essential for the gelation process. Regarding more conventional PF and RF systems, where RF forms gels due to an increased interaction and therefore stabilisation with water, a similar effect can be assumed in the borax system, but has to be investigated in more detail. It has to be mentioned, that HC of pure HMF with borax as additive leads to perfect gels as well. Importantly, borax salts are not permanently bound to the surface in the final product and can be easily washed out at the end of the process, essentially to be recycled for the next catalysis cycle.

Regarding the mechanism of the catalysis it is to be mentioned that borates are known to catalyse esterification<sup>[68]</sup> and decarboxylation.<sup>[69]</sup> However, these properties at least do not obviously affect the hydrothermal carbonisation reaction pathways. One characteristic, also in the context of HC, is the formation of boron - dioxo complexes. Taking into account the carbonisation pathway as introduced in the present thesis, the acetalisation is the only reaction which would obviously be affected by borax addition. It is therefore proposed that borax most likely coordinates sugars and thereby competes with the aldehyde - protecting acetalisation reaction of sugars with HMF, promoting aldol condensations of the “free” HMF. However, acetalisation also partially increases HMFs reactivity (electrophilic reactions and carbocation formation; see section A1). Therefore, borax in effect, changes the relative importance or sequence of different reactions, but still accelerating the overall process.

### **A3 Carbon Aerogels with Optimised Surface Area and Transport Porosity via Borax-Mediated Hydrothermal Carbonisation of Glucose**

Aerogels are known in a great variety of compositions and are used in a manifold of high - end applications including chromatography, adsorption, separation, gas storage, detectors, heat insulation, as supports and ion exchange materials.<sup>[70-72]</sup> Without doubt, silica aerogels are the most prominent and developed materials in this field, as they have revolutionised high pressure liquid chromatography (HPLC), allowing highest resolution and fast separation at the same time.<sup>[73]</sup> Silica however also has some chemical disadvantages, and in 1987, Pekala *et al.* described for the first time organic aerogels as an interesting alternative.<sup>[60]</sup> Aerogels are defined by the *IUPAC* as non - fluid networks composed of interconnected colloidal particles as the dispersed phase in a gas which is usually air. Typically an aerogel is formed by supercritical drying of the wet colloidal gel. Their characteristics include interconnected large diameter mesopores, low material density ( $\rho \sim 0.004 - 0.5 \text{ g cm}^{-3}$ ) and high specific surface area. The formation of colloidal gels is a “*bottom up*” synthetic process following the well - established sol - gel chemistry where colloidal particles form at first and then are aligned and condensed by thermodynamic forces.<sup>[74]</sup> Therefore the aerogel synthesis, achieved *via* the HC processing of sugars, is of significant interest, not only from the viewpoint of green chemistry but also with application potential in mind. The exciting new HC system was further investigated, especially in terms of particle size and porosity control. The results should be related to the well - known trends in the RF system. Additionally, the conversion into conductive carbon aerogels and their potential use in electrochemical applications are addressed.

Hierarchically structured but also inexpensive porous organic aerogels are capable of competing with their inorganic (*e.g.* silica) counterparts in sorption and insulation applications.<sup>[71, 72]</sup> The most common organic aerogels are the aforementioned RF systems. Here the formation of the gel phase occurs through the catalysed polycondensation of the reactive precursors in water.<sup>[60]</sup> The whole gel formation can take several days. A well - developed microstructure is also crucial for the following drying procedure to achieve the organic aerogels. The solvent has to be removed from the

pores, while the structure has to withstand capillary forces induced by evaporation. Some investigations on this topic have been summarised by Job *et al.*<sup>[75]</sup> So far supercritical drying is still the most prominent procedure used to minimise the effects of capillary collapse.

Besides being highly porous and lightweight, another advantage of organic aerogels is the possibility to introduce electric conductivity by converting them into carbon aerogels, thus accessing electrical / electrochemical applications like batteries,<sup>[76]</sup> supercapacitors,<sup>[77]</sup> and as conductive supports.<sup>[78]</sup> For those applications, it is important to have additional control over micro- and mesoporosity development. As it is possible to subtly influence and design material nanoscale structuring by chemical means, such that carbon aerogels can also be classified as nanostructured carbon.<sup>[64]</sup> To convert polymer into carbon aerogels, usually pyrolysis is employed (*e.g.*  $T > 500\text{ }^{\circ}\text{C}$ ). The carbonisation process leads to a loss of oxygen and hydrogen functionalities and therefore more condensed carbon structures.<sup>[64, 79]</sup> Finally, depending on the pyrolysis temperature and the respective precursor chemistry (“graphitisability”) of the former organic structure, an electrically conductive carbon network is achieved and can be used for a wide range of applications. A review article on RF - based organic and carbon aerogels was published by Al - Muhtaseb *et al.*<sup>[80]</sup>

The more flexible, green and sustainable approach of HC using inexpensive and renewable resources and a less harmful synthesis,<sup>[81]</sup> is advantageous, serving both the economic and ecologic point of view.<sup>[82]</sup> However, there is still no simple route which allows subtle control over textural properties (*e.g.* surface area) and, in the context of this section, the ability to direct and reduce sugar - derived pure hydrothermal carbon particle size to the nano - range. Analogous to previous aerogel recipes, experimental parameters are adjusted to control both material micro- and nanostructure, as particle size like for the classical RF system should depend on the ratio of precursor / catalyst *i.e.* sugar / borax, while porosity depends on overall concentration. Similarly to traditional RF - based systems, the HTC hydrogels can be dried *via* diverse routes (*e.g.* evaporative drying, supercritical CO<sub>2</sub> extraction or freeze drying) to achieve HTC aerogels, which after carbonisation should give carbon aerogels, all together herein sub - summarised under the term “*Carbogels*”.



In the third section of this thesis, different glucose / borax - derived hierarchically structured carbon aerogels are produced. After simple freeze - drying electron microscopy and sorption techniques are applied to characterise the texture and the hierarchical pore system of the carbonaceous aerogels in detail. Post - synthesis thermal carbonisation is also employed to obtain carbon monoliths and introduce electric conductivity. Preliminary tests of the electric conductivity and properties as porous electrodes are conducted. Representative of our reported system, four *Carbogel* examples were synthesised at different sugar / borax ratios denoted as *Carbogels X*, where *X* corresponds to the used amount of borax in milligrams while the amount of water and glucose was kept the same (20 ml 30 % glucose solutions). The *Carbogels* were produced by hydrothermal treatment of the solutions at 180 °C for 8 hours. Shorter reaction times resulted in the formation of unstable gels or sol - like suspensions. Mechanically stable and brown- to black - coloured monoliths were obtained (Figure A15; monolith V was strongly shrinking within the drying process).



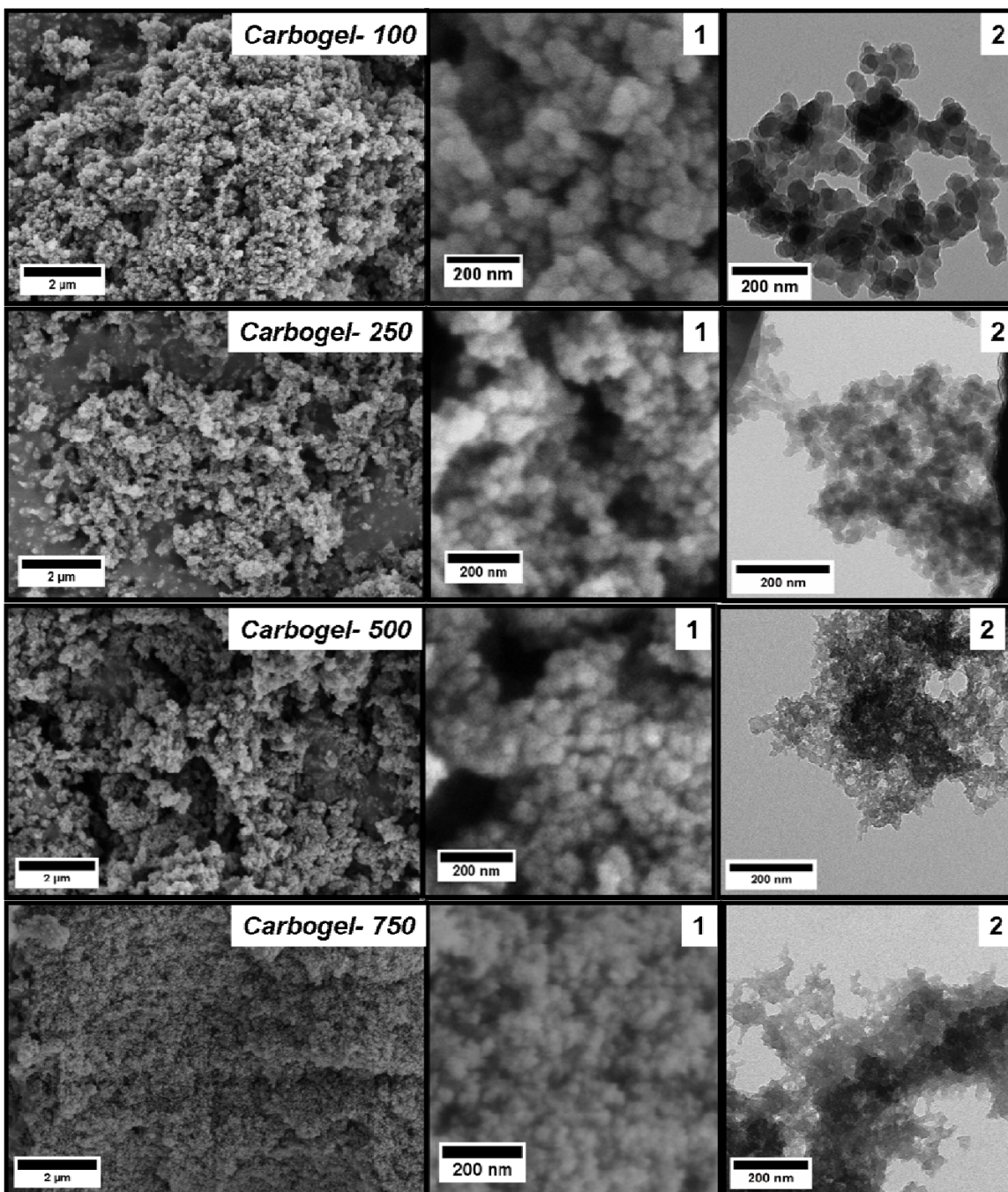
**Figure A15:** Image of representative *Carbogels* achieved from different amounts of borax added to a standard HTC recipe. Borax content: I) 100 mg, II) 250 mg, III) 500 mg, IV) 750 mg, V) 1000 mg. To show the gelation through the whole volume the glass vial *i.e.* reaction vessel is shown. A 2 Euro coin is added as size scale.

Non - incorporated soluble compounds including borax were then removed by H<sub>2</sub>O and ethanol extraction (until the extraction solvent was colourless), followed by further solvent exchange with excess H<sub>2</sub>O prior to freeze drying. Under the reported reaction conditions, low density (*e.g.*  $\rho \sim 0.12 \text{ g cm}^{-3}$ ) *Carbogels* were produced of  $\sim 3.1 \text{ g}$  mass with a carbon content of  $\sim 64 \%$  (thus resulting in  $80 \%$  carbon yield with respect to glucose, the volume fraction of pores is  $\Phi \approx 0.94$ ). SEM and TEM image analysis of the resulting aerogels revealed the presence of very small, spherical HTC nanoparticles, aggregating to create a gel structure with hierarchical porosity. With increasing system borax concentration, the microstructure becomes increasingly finer due to decrease in primary particle size (Figure A16). The decreasing particle size with decreasing sugar / borax ratio is in accordance to the structure control trends in the classical RF system (Figure A8, section A2). Regarding previously described sol – gel principles, this does not only indicate similar nucleation in between the two systems, but also corroborates the role of borax being a catalyst in the process of HC.<sup>ii</sup> The particle diameter of *Carbogel - 100* was calculated as  $\sim 41 \text{ nm}$ , decreasing to  $< 7 \text{ nm}$  with increasing borax concentration (*e.g.* *Carbogel - 750*; Table 1). Both SEM and TEM images reveal the *Carbogel* network to be composed of monodisperse, aggregated, spherical nanoparticles generating the desired hierarchical porous network, well suited for application in catalysis, electrochemical applications (*e.g.* electrocatalysis, batteries and supercapacitors) or chromatography, where fast mass transport through the pore system plays a crucial role. It has to be mentioned that the gel structure shrinks at lower sugar / borax ratios throughout freeze - drying, indicating that the more fragile,  $7 \text{ nm}$  thick carbon walls cannot withstand the higher capillary pressures. (Note that with an overall downscaling of the structure the wall stability is less, while the capillary pressures increase.) Further worth to mention is, that the particle size control is not limited to the sub -  $50 \text{ nm}$  range. Experiments with less borax and / or longer reaction times lead to gels with particle size bigger than  $100 \text{ nm}$  range and therefore very likely cover the whole possible range underneath classical HTC particle dimensions.

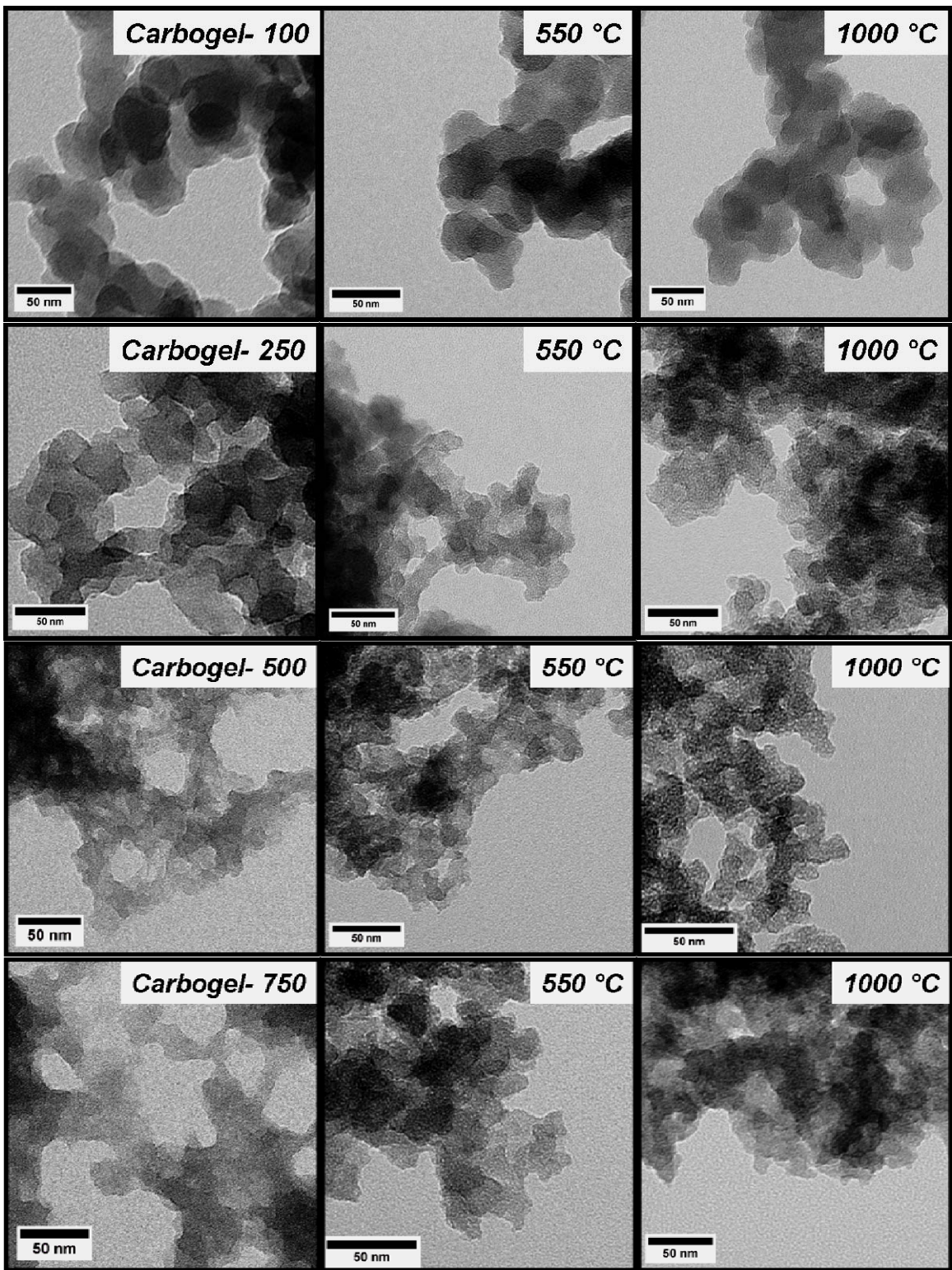
---

<sup>ii</sup> Porosity control depending on the ratio of precursor / solvent, like in the classical RF system, was confirmed with  $15 \text{ wt.}\%$  glucose solutions, which also leads to gelation throughout the whole reaction volume. However, the detailed results are herein not presented.

Thermal treatment of the dried hydrophilic gels under nitrogen atmosphere at 550 °C and 1000 °C (heating rate = 10 K min<sup>-1</sup> followed by an isothermal period of 5h) leads to uniform dimensional shrinkage of the monolith macrostructure with preservation of the overall cylindrical shape. As observed *via* TEM, at higher sugar / borax ratios the local nano- and microstructure in terms of particle shape and connectivity are also retained upon heating to these carbonisation temperatures (Figure A17). However, aerogels composed of very fine, sub - 10 nm particles do not completely withstand the carbonisation process and shrink to more condensed systems. Determination of the particle size *via* TEM (Figure A17 / *Carbogel 750@1000 °C*) indicates that also the primary particle size decreases upon carbonisation, in accordance with the mass loss throughout carbonisation. Elemental analysis indicates the loss of oxygen and hydrogen from the carbonaceous material structure, with the carbon content increasing from ~ 64 wt. % (as - prepared) to ~ 94 wt.% (@ 550 °C) and ~ 97 wt.% (@ 1000 °C).



**Figures A16:** SEM and TEM images of *Carbogels* -  $X$  prepared from different amounts  $X$  of borax (in mg), with the same amount of water and glucose. SEM overview images are presented on the left side, while higher resolved SEM and TEM images are for each *Carbogel* indicated as 1 and 2.



**Figures A17:** Comparison of TEM images of as - prepared *Carbogels* - *X* and the respective post - carbonised samples at 550 °C and 1000 °C, where *X* stands for the used amount of borax within the synthesis protocol.

In addition, nitrogen sorption measurements were carried out to investigate the porosity of the as - formed hierarchical carbon structures (Table 1). With increasing sugar / borax ratio, the aerogels show an increasing gas uptake and a higher specific surface area due to the presence of smaller primary nanoparticles. *Carbogel - 750* breaks this trend, as the  $S_{\text{BET}} = 209 \text{ m}^2 \text{ g}^{-1}$  is decreased compared to  $233 \text{ m}^2 \text{ g}^{-1}$  for *Carbogel - 500*. In accordance with the TEM images (Figure A17), this reflects the collapse of the very fine structure within the freeze drying process, *i.e.* 7 nm disordered carbon cannot withstand the capillary forces of a pore of similar size. This is well known from corresponding, even rigid polymer structures.<sup>[83]</sup>

Regarding gas sorption behaviour for the post - carbonised systems, a strong increase of the specific surface area especially after thermal treatment at  $550 \text{ }^\circ\text{C} / \text{N}_2$  is observed. High surface area materials exhibiting  $\sim 600 \text{ m}^2 \text{ g}^{-1}$  (*Carbogel - 250 @ 550 }^\circ\text{C}*) are accessible even without chemical activation using the relatively simple synthetic route and conditions. Mechanistically *retro* - Diels - Alder reactions are expected to be involved into this very interesting property of HTC. Diels - Alder reactions provoke cross - linking of substructures (potentially of the size of micropores), are reversible and high temperatures / low pressures support the *retro* direction. The carbonised *Carbogel - 100* and *Carbogel - 250* samples again show a trend of increasing surface area with increasing sugar / borax ratio, the result of a reduction in the primary particle size. The high borax structures are again already too fine to withstand carbonisation completely, resulting in partial structure collapse and a marked reduction of the accessible surface and overall porosity. The interplay of enhancement of surface area and fragility of the architecture is also nicely reflected in the high temperature data: carbonisation at higher temperatures (*i.e.*  $1000 \text{ }^\circ\text{C}$ ) produces lower surface area materials, although the primary particle size has been dramatically decreased.

**Table 1.** Specific surface area and particle size (TEM) for representative *Carbogels* prepared at 180 °C and material post - carbonised at 550 °C and 1000 °C.

Sample Name	180 °C		550 °C		1000 °C	
	<sup>a</sup> S <sub>BET</sub> , m <sup>2</sup> g <sup>-1</sup>	<sup>b</sup> Particle diameter, nm	<sup>a</sup> S <sub>BET</sub> , m <sup>2</sup> g <sup>-1</sup>	<sup>b</sup> Particle diameter, nm	<sup>a</sup> S <sub>BET</sub> , m <sup>2</sup> g <sup>-1</sup>	<sup>b</sup> Particle diameter, nm
<i>Carbogel-100</i>	84	41	491	33	275	28
<i>Carbogel-250</i>	208	22	614	18	360	13
<i>Carbogel-500</i>	233	12	458	14	206	13
<i>Carbogel-750</i>	209	8	403	12	205	-

*<sup>a</sup>Specific Surface Area from BET method; <sup>b</sup>Diameters calculated in Image J software from TEM images*

A more quantitative porosimetry analysis of the so far optimal products, *Carbogel - 250* and the corresponding post - carbonised *Carbogels*, was performed (Table 2; Figure A18). Only marginal hysteresis and lack of defined plateau region as relative pressure reaches unity (*i.e.*  $p/p_0 \sim 1$ ) of the sorption profile, reflects the combination of a slit - type micropore structure combined with a high external surface area due to small, interconnected primary carbon nanoparticles (Figure A18). The “*exploding*” sorption capacity at relative pressures near unity reflects the presence of excessive large diameter mesoporosity and macroporosity, which can be expected from a material with 94 vol. % overall porosity.

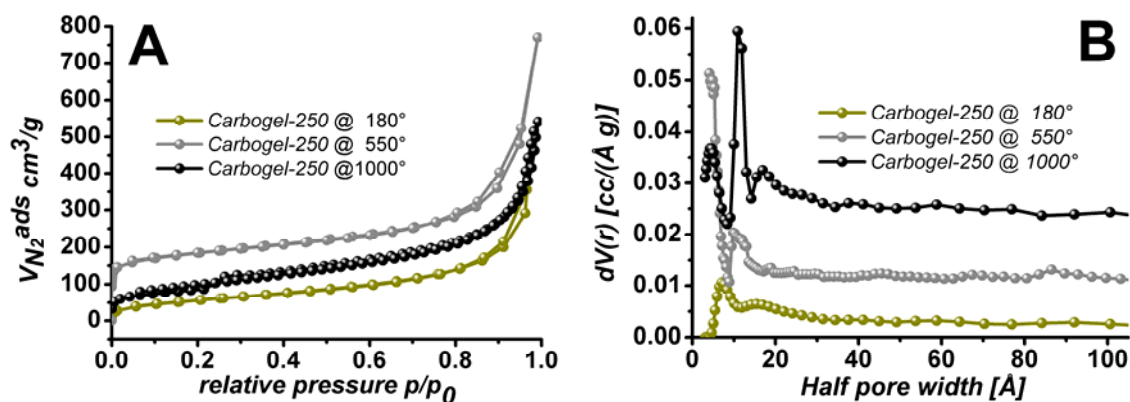


**Figure A18:** Comparison of nitrogen sorption analysis of as - prepared *Carbogel - 250* and the respective products from post - carbonisation at 550 °C and 1000 °C. A) Nitrogen sorption isotherms B) Pore size distributions

As - prepared *Carbogels* show in general limited microporosity ( $V_{micro} \leq 0.10$   $cm^3g^{-1}$ ; Table 2), which is very typical for ductile, polymer - like behaviour of the walls.<sup>[83]</sup> Heat treatment at 550 °C significantly increases this micropore content to about  $0.25$   $cm^3g^{-1}$ , which means that the material now behaves as a rigid carbon scaffold post - carbonised carbon aerogels showing isotherms (left) and pore size distributions (right).

**Table 2.** Nitrogen sorption data and electrical conductivity for *Carbogel - 250* prepared at 180 °C and post - carbonised at 550 °C and 1000 °C.

Sample Name	<sup>a</sup> $S_{BET}$ , $m^2g^{-1}$	<sup>b</sup> Pore volume, $ccg^{-1}$	<sup>b</sup> Micropore volume, $ccg^{-1}$	<sup>b</sup> Mesopore volume, $ccg^{-1}$	<sup>b</sup> APD, nm	Specific conductivity, S/m
<i>Carbogel-250@180 °C</i>	208	0.43	0.10	0.34	1.56	$0.7 \cdot 10^{-3}$
<i>Carbogel-250@550 °C</i>	614	0.81	0.24	0.57	0.82	60
<i>Carbogel-250@1000 °C</i>	360	0.54	0.18	0.36	2.18	290

<sup>a</sup>Specific Surface Area from BET method; <sup>b</sup>Pore size characteristics obtained via the QSDFT model; <sup>c</sup>Potentiostatic Electrochemical Impedance Spectroscopy (1-1000Hz; R-Model)



Also the mesopore volume is observed to increase nicely upon carbonisation at 550 °C ( $V_{\text{meso}} > 0.5 \text{ cm}^3\text{g}^{-1}$  @ 550 °C; Table 2), most likely as the result of material contraction / condensation processes opening up interstitial porosity between the primary particles, which was closed ahead by ductile deformation. Interestingly, nitrogen sorption at *Carbogel - 250* @ 1000 °C shows a loss both of micro- and mesoporosity. This means that the structure rearrangements observed by TEM on a larger scale are also found on the molecular and low nanometre scale: the whole structure simply sinters due to temperature induced carbon - carbon rearrangements.

To investigate the applicability in electrochemical applications (*i.e.* as electrode materials in various systems), the electrical conductivities of pulverised and pressed *Carbogel - 250* before and after thermal treatment under inert atmosphere was measured. Electrochemical measurements were carried out with Gamry Reference 600 potentiostat (Gamry Instruments) and Gamry EIS 300 / Physical Electrochemistry software. The electrical conductivity was evaluated applying a simple resistor - model on potentiostatic impedance spectroscopy at 1 - 1000 Hz using a two electrode setup. The specific conductivities increase with increasing carbonisation temperature reaching 290 S m<sup>-1</sup> at 1000 °C (Table 2). These values are, considering the high porosity of the materials, comparably high and absolutely sufficient to support an electrode application. The hierarchical porosity of the monolithic Carbogels suggest the use of the material as electrodes for fast processes, where mass transport takes a crucial role.

## **A4 Functional Carbon Spheres *via* Hydrothermal Carbonisation of Biowaste**

As previously mentioned a challenge in HC is the employment of natural appearing biomass to achieve useful - meaning applicable - carbon materials. In the present study for the purpose of demonstrating the general applicability of “real” biomass, watermelon juice was investigated in a short series of experiments as natural feedstock for advanced functional carbon materials within the process of hydrothermal carbonisation. The high carbon efficiency of the process could therefore lead to effective carbon capture. The well - defined shape of carbonaceous spheres from HC of watermelon juice will be shown to be indicative for an undisturbed process, which is applicable for the production of advanced functional materials. This is presented by further applying watermelon juice as precursor for hybrid material, known to be active as adsorbent for the removal of heavy metals from water.

Apart from sugar cane, food or fodder is generally not considered as feedstock of chemicals / materials, as competition between nutrition and production should be avoided. However, watermelons are worth to venture a more detailed look at, due to the following facts:

1. Each year about twenty percent of the whole watermelon crop is wasted due to surface blemishes or misshapen specimens.<sup>[84]</sup> For the 2009 growing season, this amounted to around 20 million tons worldwide (14 million tons/China; 0.6 million tons /E.U.; 0.4 million tons /U.S.).<sup>[85]</sup> This cull is left in the field and eventually digested mainly to CO<sub>2</sub> and nutrient salt. Therefore, the Agricultural Research Service of the U.S. Department of Agriculture already suggests the use of this biomass economically.
2. Watermelons contain the nutraceuticals lycopene and L - citrulline. Lycopene, a polyene and red dye in the fruits, is a powerful antioxidant and important in prostate health.<sup>[86]</sup> L - citrulline is involved in the detoxification of catabolic

ammonia and in the production of the circulatory vasodilator, nitric oxide.<sup>[87]</sup> The extraction of both nutraceuticals generates a waste stream of 500 litres of watermelon juice per ton of watermelons.<sup>[84]</sup> This can be understood as purified precursor solution for HC.

Herein freshly squeezed and lycopene - purified watermelon juice as precursor for the production of functional hydrothermal carbon is investigated. Purified watermelon juice essentially is a solution of ~ 10 % simple carbohydrates disposed into glucose, fructose and sucrose. Especially glucose and fructose are intensively investigated as model precursors in HC.<sup>[88]</sup> All three sugars solely used as carbon precursor can be converted into structurally well - defined and also chemically high quality hydrothermal carbon.<sup>[89]</sup>

In the present study, first simple hydrothermal carbon was synthesised from watermelon juice. After a thorough characterisation of the resulting product, the watermelon biowaste is then applied for the production of a hybrid material with an increased number of distinct functional groups in a second step. Hydrothermal carbonisation was carried out by sealing 20 ml of the juice / solution into an open - end glass vial (~ 25 ml) inside a typical Teflon<sup>®</sup> - lined autoclave system (~ 45 ml). For the synthesis of functional hybrid carbon 5, 10 and 20 wt. % of acrylic acid were added to the watermelon juice, respectively. The autoclaves were heated to 200 °C for 20 hours. After reaction the autoclave was allowed to cool down to room temperature. The solid product was washed with 750 ml of distilled water and vacuum dried at 70 °C over night.

#### 1) Watermelon juice as precursor for hydrothermal carbon

By extraction of lycopene and amino acid (*i.e.* L - citrulline) one converts watermelon juice basically into a solution of ~ 10 % glucose, fructose and sucrose. Centrifugation predominantly separates the hydrophobic lycopene from the solution. Therefore additionally amino acids, in a concentration of up to 15 - 35  $\mu\text{mol mL}^{-1}$ <sup>[84]</sup>, have to be considered.

The defined spherical shape of the carbonaceous material is assumed to be an indicator for an undisturbed process, which can be employed for advanced synthesis *e.g.* functional hybrid materials for special applications.

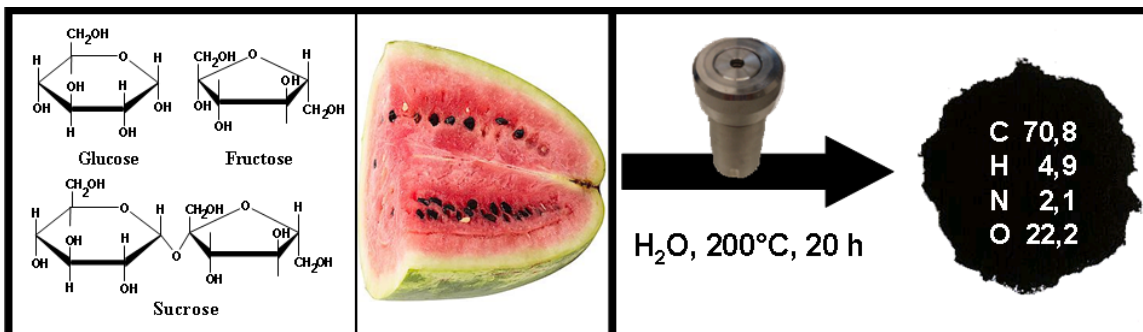


**Figure A19:** Schematic visualisation of the hydrothermal carbonisation process using purified watermelon (a solution of different sugars) showing the elemental composition of the resulting products.

The elemental composition of watermelon juice derived hydrothermal carbon (wm - HTC) is typical for sugar - derived hydrothermal carbon (Figure A19). The nitrogen content of  $\sim 2\%$  can be explained by the incorporation of the non - proteinogenic L - citrulline. The presence of nitrogen can be understood as a potential considering that nitrogen containing materials recently found important applications as electrodes in supercapacitors<sup>[90]</sup> or even as catalysts for oxygen reduction reaction.<sup>[91, 92]</sup> Scanning electron microscopy (SEM) shows the well - defined spherical shape of most of the particles with only minor appearance of interconnected particles (Figure A20/left).

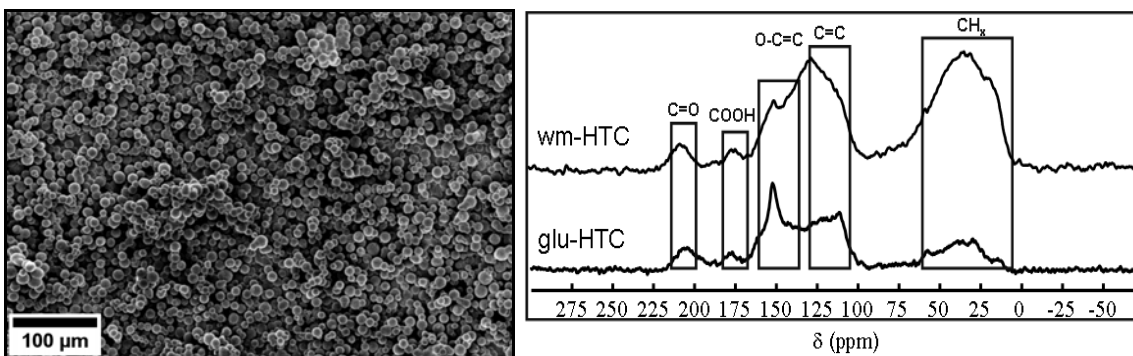


**Figure A20:** Representative SEM picture of wm - HTC (left) and the corresponding solid - state NMR spectrum (wm - HTC) compared to glucose - derived hydrothermal carbon (glu - HTC) (right).

However, the particle size is a curiosity. While typical carbonaceous spheres from HC of sugars in water are around two micrometers in diameter,<sup>[3]</sup> wm - HTC is composed of particles of 5 to 10  $\mu\text{m}$  size. This is a range particularly interesting for chromatographic applications. Regarding the former described reactions, involved in the hydrothermal carbonisation of sugars, being strongly sensitive towards nucleophiles (aldehyde group, hydroxy leaving group and aldol condensation) one can assume, that L - citrullin react comparably fast and thereby creates nucleation seeds relatively early. These early nuclei consequently grow larger within the proceeding carbonisation.

To further investigate the chemical composition of the product  $^{13}\text{C}$  solid - state magic angle spinning (MAS) NMR spectroscopy was applied. Classical hydrothermal carbon from glucose (glu - HTC) representing hexoses, was produced under same conditions as wm - HTC. Figure A21/right provides a comparison of the resulting NMR spectra.

Although for wm - HTC one could expect an analogue spectrum to glucose *i.e.* representative for hexoses a clear similarity to spectra of nitrogen doped HTC (*e.g.* from N - Acetylglucosamine) can be observed.<sup>[90, 93]</sup> Therefore, chemically HC of watermelon juice leads to typical nitrogen - doped hydrothermal carbon, which corroborates the considered role of L - citrulline on the particle size. Characteristics are the pronounced aromatic ( $\sim 120 - 130$  ppm) and aliphatic region ( $\sim 10 - 40$  ppm), which both can be explained by involved L - citrulline. The aromatic peak is induced by the inherent nitrogen content, while the aliphatic signal arises from the alkylene substructure of the amino acid. Presumably the amino acid, present in watermelon, enters the reaction pathway in a typical Maillard type chemistry, well known from food industry.<sup>[94]</sup> The intermediate imines form electron - rich dienophiles subsequently reacting in Diels - Alder reactions to further originate aromatisation. NMR spectroscopy confirms the results of elemental analysis and electron microscopy. Therefore it is concluded that lycopene - purified watermelon juice is sufficiently suitable as feedstock for the process of hydrothermal carbonisation. In terms of product quality no obstacles for the employment of watermelon juice for advanced processes, such as the production of functional hybrid materials, can be foreseen.

## 2) Watermelon juice as precursor for advanced functional hybrid products

To affirm the previous conclusion and therefore the assumption of a well - defined structure being an indicator for an undisturbed carbonisation process, watermelon juice was further applied to the synthesis of carboxylate - rich carbonaceous hybrid material, which is known to be an active adsorbent for the removal of heavy metals from aqueous solutions.<sup>[11]</sup> The desired properties of this functional carbon aroused from a dramatic change in the particle morphology and chemical surface functionalities. Instead of typical smooth particles of hydrothermal carbon a “raspberry” - like, rough texture was observed. The spherical particles of the hybrid material were clearly enriched in carboxylic groups.

Analogue to the established method<sup>[11]</sup> 5, 10 and 20 wt. % of acrylic acid (corresponding to 10 wt. % sugar in watermelon juice) were added to the watermelon juice as additional “monomer” and hydrothermal carbonisation under aforementioned conditions was carried out. The products are denoted as wm - AAX (X being the amount of acrylic acid). The electron microscopically investigation demonstrates the expected change in the particle morphology confirming the role of acrylic acid as structure directing, even with the sustainable employment of watermelon juice as main carbon source (Figure A21).

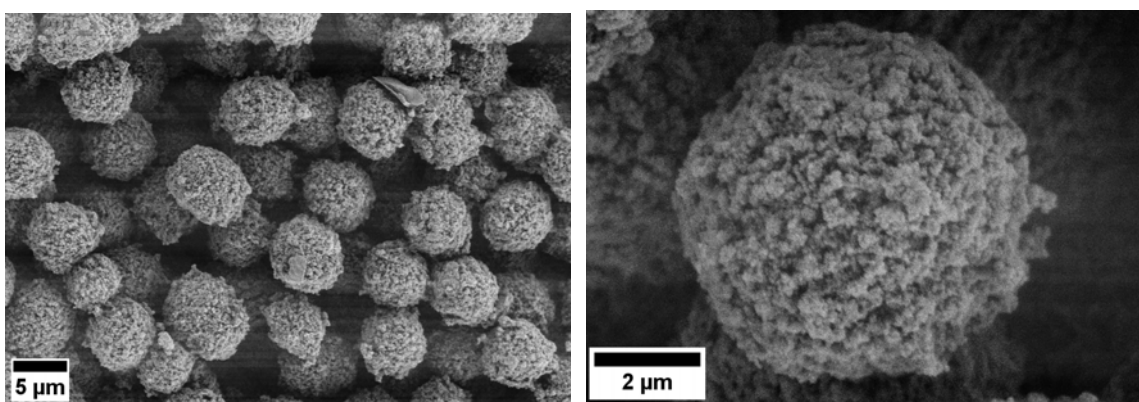


**Figure A21:** Representative SEM pictures of functional hybrid carbon from watermelon juice and acrylic acid (wm - AA20).

Like for wm - HTC the particle size of watermelon juice derived product is enhanced from 2  $\mu\text{m}$  to 5  $\mu\text{m}$ . To investigate the chemical composition, FT - IR and  $^{13}\text{C}$  solid - state NMR spectroscopy were applied. The FT - IR comparison of wm - HTC and the hybrid products with increasing amount of acrylic acid shows the characteristic peaks for carboxylic acid function, which are the acidic O - H<sub>stretch</sub> ( $\sim 2500 - 3500 \text{ cm}^{-1}$ ), acidic C = O<sub>stretch</sub> ( $\sim 1700 \text{ cm}^{-1}$ ) and the acidic C - O<sub>stretch</sub> band ( $\sim 1200 \text{ cm}^{-1}$ ) (Figure A22/left). A successive increase in intensity from wm - HTC to wm - AA20 is observed. An additional shoulder at 2800 - 3000  $\text{cm}^{-1}$  successively appears. This aliphatic C - H<sub>stretch</sub> peak can be explained by (co-) polymerisation of acrylic acid giving an aliphatic backbone decorated with carboxylic acid functions.

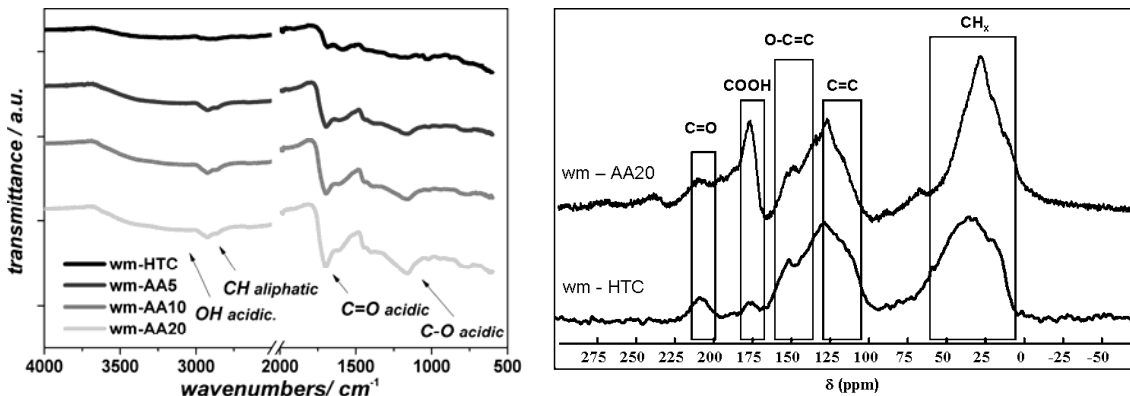


**Figure A22:** Comparison of FT - IR spectra of wm - HTC with wm - AA5 - 20 (left) and representative  $^{13}\text{C}$  solid - state NMR spectra of wm - AA20 with hydrothermal carbon wm - HTC (right).

Figure A22/right presents the NMR spectrum of wm - AA20 representative for the functional hybrid product in comparison with the former described one of wm - HTC. Both spectra show the typical profile of nitrogen - doped hydrothermal carbon with a pronounced aromatic peak at  $\sim 120 - 130 \text{ ppm}$ .<sup>[93]</sup> For wm - AA20 a strong and sharp peak at around 175 ppm, which is characteristic for carboxylic acid functional groups, can be observed. This is clearly showing the strong carboxyl enrichment of the hybrid material being crucial for its functionality in heavy metal adsorption. Additionally, a stronger and well - defined aliphatic peak ( $\sim 10 - 40 \text{ ppm}$ ) appears in wm - AA20 compared to wm - HTC. Again, this can be explained by (co-) polymerisation of acrylic acid within the synthesis. However,  $^{13}\text{C}$  solid - state NMR investigations mirror the FT -

IR results and together reveal the desired improvement of the chemical structure from hydrothermal carbon to the hybrid material by the employment of watermelon juice as “real” biomass precursor. Except for the particle size the particle morphology of wm - AA is similar to the products from acrylic acid and pure sugar. This is interesting, as wm - HTC and glu - HTC are very different hydrothermal carbons as shown by solid - state NMR (Figure A21/right). Therefore it is assumed that the hydrothermal carbonisation mostly proceeds separated from the acrylic acid polymerisation. Like proposed in A1, expanded conjugated HTC networks, either nitrogen – doped or not, may form and subsequently facilitate ionic and radical reactions, which can initiate the acrylic acid polymerisation. This would lead to a block - co - polymer type of product, which could explain the raspberry - like morphology as obtained by SEM measurements.



# **B Ionic Liquid-Derived Heteroatom-Containing Carbons – Synthesis, structure control and potential as non-metal electrocatalysts in the oxygen reduction reaction**

## **Basics and State-of-the-Art**

### **1) The Oxygen Reduction Reaction (ORR)**

The oxygen reduction reaction is essential to life being the main reaction in biological respiration. Additionally it plays a key role in the synthesis of hydrogen peroxide and as the cathode reaction in the energy conversion occurring in fuel cells, such as polymer electrolyte membrane fuel cells (PEMFCs) and direct methanol fuel cells (DMFCs). In aqueous solutions, there are two predominant mechanisms:

- The direct 4 electron reduction pathway from dioxygen ( $O_2$ ) to water ( $H_2O$ )  
*and*
- The 2 electron reduction pathway to produce hydrogen peroxide ( $H_2O_2$ ) instead of  $H_2O$ .

The 1 electron oxygen reduction to superoxide ( $O_2^-$ ) is also possible in aprotic solvents or basic aqueous solutions.<sup>[95]</sup> The elementary reactions depending on the pathway are rather sluggish (Table 3). Without ignition oxygen / hydrogen mixtures do not react under standard conditions, due to the high activation energy. Same counts for the electrochemical reaction and the respective over - potential. In practical terms a catalyst is employed to accelerate the reaction. Still mainly precious metal - based catalysts (*e.g.* platinum nanoparticles) are used.<sup>[96]</sup> In this context, a significant quantity of research has been performed on non - precious metal catalysts and non - metal catalysts to improve the cost - benefit ratio of fuel cell systems with the primary aim of making them profitable and accessible on a mass market level. The electron transfer number herein is crucial to be 4, as precious metal catalysts typically degrade under

exposure to hydrogen peroxide. Therefore the production of hydrogen peroxide needs to be avoided in context with such catalysts. However, this research also aims to develop ORR catalysts suitable for the efficient production of hydrogen peroxide.<sup>[97]</sup>

**Table 3:** Elementary reactions in the electrochemical reduction of oxygen<sup>[95]</sup>

<b>Electrolyte</b>	<b>ORR reactions</b>
Acidic aqueous solutions	$\text{O}_2 + 4 \text{H}^+ + 4 \text{e}^- \rightarrow 2 \text{H}_2\text{O}$ $\text{O}_2 + 2 \text{H}^+ + 2 \text{e}^- \rightarrow \text{H}_2\text{O}_2$ $\text{H}_2\text{O}_2 + 2 \text{H}^+ + 2 \text{e}^- \rightarrow 2 \text{H}_2\text{O}$
Alkaline aqueous solutions	$\text{O}_2 + 2 \text{H}_2\text{O} + 4 \text{e}^- \rightarrow 4 \text{OH}^-$ $\text{O}_2 + \text{H}_2\text{O} + 2 \text{e}^- \rightarrow \text{HO}_2^- + \text{OH}^-$ $\text{HO}_2^- + \text{H}_2\text{O} + 2 \text{e}^- \rightarrow 3 \text{OH}^-$

## 2) Electrocatalysis

Our present energy and environment situation and the related increasing importance of energy conversion technologies put electrochemistry into focus. Common processes to generate electrical power through energy conversion show efficiencies not much higher than 30 %, because the heat engine related power plants use processes like combustion to create mechanical energy, which is then converted into electrical energy. These processes are bound to the Carnot efficiency. The electrochemical energy conversion encountered in batteries, fuel cells and supercapacitors is due to interfacial energy or charge transfer and can therefore be of much higher thermodynamic efficiency.<sup>[1]</sup> As such electrocatalysis is described as the accomplishment of an electrochemical reaction employing an appropriate catalyst, which is either decorated on the electrode or it can be the electrode itself. However, in electrochemical reactions the full utilisation of the thermodynamic potential is hindered by so - called over - potentials. Therefore, the aim of electrocatalysis is to reduce or minimise these over - potentials.

In 1963 *W. T. Grubb* introduced the term “*electrocatalysis*” (originally suggested by *Liebhaufsky*) in context with his fuel cell research to the academic community.<sup>[98]</sup> Today the polymer electrolyte fuel cell is still the most prominent example of electrocatalysis. In

the cathode reaction of the cell the former described oxygen reduction reaction (ORR) takes place. The relatively high over - potential of the ORR is the reason why the reaction rate is still sluggish and fuels cells suffer from inefficiency even with the very expensive precious - metal catalysts. In the following fundamental electrochemical tests for the investigation of electrocatalysts are introduced.

### ***Potential Sweep Techniques***

The most widely used methods to investigate electrode processes are the potential sweep techniques representing the supergroup of cyclic voltammetry (CV) and linear sweep voltammetry (LSV). Time - varying potentials are applied to the working electrode. The resulting faradaic and capacitive currents are due to potential - dependent chemical and physical processes, which are oxidation / reduction of electroactive species and adsorption phenomena or double - layer charging. Beside physical and chemical processes one can additionally distinguish between reversible and irreversible processes. The different processes give rise to versatile possible applications. Supercapacitors are based on reversible double - layer charging, while pseudo - capacitors additionally profit from very fast reversible chemical reactions at the solid surface. Re - chargeable batteries in this context work due to reversible reactions and fuel cells convert chemical energy from irreversible reactions into electrical energy. As carbon materials are applied in each of these applications the need to separate single effects and investigate only one distinct phenomenon is obvious. The catalytic activity for the ORR can be tested with CV, although LSV is sufficient, because only irreversible cathode currents are important. An additional reduction peak emerges by purging the former deoxygenated electrolyte with oxygen or air. However, onset potential and peak currents might be overlapped by capacitive current contributions, especially in the case of high surface area carbons. Therefore special single potential sweep measurements are typically used to illustrate ORR activity. To distinguish different current - contributing effects here one can change process - specific parameters. To investigate the ORR activity the availability of oxygen at the electrode is varied using the rotating - disc electrode.

### ***Rotating - Disc Electrode***

Transportation of reactants from or to the electrode generally proceeds *via* diffusion or convection. The main and limiting process for mass transport around the surface of an electrode is diffusion. An increased mass transport can be achieved by forced convection through a controlled motion of the electrode relative to the electrolyte using the rotating disc electrode (RDE). Even if the electrode is rotating, causing transport of reactants to the electrode and transport of products away from the electrode, there still remains a stagnant reaction layer where mass transport happens through diffusion. The thickness of this layer is controlled by the rotation rate of the electrode. The increasing velocity leads to a reduced layer thickness. In a linear sweep experiment, the potential of the working electrode is scanned from potentials where no reaction occurs to potentials where high reaction rates are achieved. Combined with the controlled mass transport of the RDE a steady - state diffusion - controlled current can be achieved at a certain potential for each rotation rate. This is when  $C/L$ ,  $C$  being the bulk concentration of the reactant and  $L$  being the diffusion layer thickness, is constant and the concentration of the reactant at the surface is zero. The steady - state diffusion - controlled current  $i_d$  is described by the Levich equation.<sup>[99]</sup>

$$i_d = 0.62 \cdot z \cdot F \cdot A \cdot D^{\frac{2}{3}} \cdot \nu^{-\frac{1}{6}} \cdot C \cdot \omega^{\frac{1}{2}}$$

**Formula 1:** Levich equation of the steady - state diffusion - controlled current

Where  $z$  is the number of transferred electrons,  $F$  is the Faraday constant,  $A$  the electrode area,  $D$  the diffusion constant of the reactant,  $\nu$  the kinematic viscosity of the electrolyte, and  $\omega$  the rotation rate. At the onset potential the current is controlled by the reaction kinetics and in between the onset potential and  $i_d$  both the mass transport and the kinetic current  $i_k$  contribute. In the whole potential range the current can be described by the Koutecky - Levich equation, where  $i$  represent the disc current and  $i_k$  the kinetic current:

$$\frac{1}{i} = \frac{1}{i_d} + \frac{1}{i_k}$$

**Formula 2:** Koutecky - Levich equation for the rotating - disc technique

Plotting of  $1/i$  against  $1/\omega^{1/2}$ , the so - called Koutecky - Levich plot (KL plot), gives a linear graph with the kinetic current as the intercept and the slope being characteristic of the electron transfer number. Commonly, the KL plot is used to visualise the reaction mechanism, by comparing it to lines with slopes of theoretical 2 and 4 electron processes. The actual electron number can be calculated from the so - called B parameter, which is the inverse slope in the KL plot.

### 3) Heteroatom - containing Carbons from Ionic Liquid Precursors

The introduction of secondary lightweight elements, such as nitrogen or boron, into the chemical structure of carbon alters its properties, depending on the heteroatom amount and the nature of bonding. It is well known that the introduction of boron or nitrogen into a pool of  $sp^2$  - bonded graphitic carbon atoms leads to distinctly different carbon material properties. Improved electric conductivity and increased chemical stability are just two of the potential benefits.<sup>[100]</sup> While nitrogen, which is surface - attached *via* functional groups mostly changes chemical properties and is therefore called chemical nitrogen, structural nitrogen (incorporated into the graphitic sheets) shows also high impact on the physical properties of the final carbon material. A very popular property amplification achieved by such nitrogen introduction is the increase of electric conductivity.<sup>[101-104]</sup> Doping with the electron - rich nitrogen atoms modifies the band structure of the material:<sup>[105]</sup> the valence band is lowered, thus the material is chemically more stable, and the electron density at the Fermi level is increasing. This has experimentally been shown to induce a metallic character in nitrogen - doped CNTs.<sup>[106]</sup> Practical observations could also be supported by quantum mechanical calculations by *Carvalho et al.*<sup>[107]</sup>

The simultaneous incorporation of boron and nitrogen into graphitic carbon to give B/N - doped carbon to boron carbon nitrides is of certain interest as well. The

influence of the addition of  $sp^2$ -BN, which is isoelectronic to graphitic carbon, on physical properties should allow the successive alteration of properties between graphite and hexagonal boron nitride ( $h$ -BN). Indeed it is known that boron and nitrogen containing graphitic compounds reveal semiconducting properties combined with a lower band gap compared to pure  $h$ -BN.<sup>[108]</sup> For B/N-doped carbons or boron carbon nitrides desired properties like an adjustable band gap were reported also.<sup>[109]</sup>

In addition to improved physical properties, introduction of chemical functionality at the surface *via* boron and / or nitrogen hetero doping and at the same time keeping highly favourable properties of carbon such as electric conductivity, chemical stability and high surface area, can be expected to lead to high performance materials. Therefore, porous carbon-based materials are known for their versatile applicability in gas separation, water purification and catalyst supports as well as important new areas in electrochemistry (*e.g.* electrodes for batteries). Nitrogen doping not only influences the physical properties but also the chemical properties, as observed by an increase in material basicity. While layer edge chemical nitrogen functionalities give rise to a Brønsted-basidity due to *e.g.* amine groups, structural nitrogen induces an increasing Lewis-basidity, which tailors nitrogen-doped carbon materials for applications in catalysis.<sup>[110]</sup> Recent reports have shown that porous carbon with structurally integrated nitrogen act as an inexpensive and metal-free catalyst in the oxygen reduction reaction (ORR), used in PEMFCs.<sup>[111]</sup> The ionic character of the BN bond and the mechanical stress induced by incorporated  $sp^2$ -BN moieties into graphitic carbon are expected to lead to further interesting properties for sorption purposes and metal-free catalytic applications.<sup>[112, 113]</sup> Recent reports have also demonstrated the potential applicability of boron-doped catalytic materials for the ORR.<sup>[113-115]</sup> Generally, heteroatom introduction into the carbon structure can also enhance material performance in the double-layer electrode in supercapacitors due to the so-called pseudo-capacitive effect.<sup>[116, 117]</sup>

*In-situ* processes that derive the final material directly from nitrogen-rich precursors, either by thermolysis or pyrolysis or by chemical vapour deposition (CVD) are the main synthesis routes to nitrogen-doped carbons with high contents of structural nitrogen.<sup>[118, 119]</sup> Commonly used precursors are aminosugars,<sup>[120]</sup> melamine,<sup>[121, 122]</sup> benzylamine,<sup>[123]</sup> nitrogen containing heterocycles<sup>[105, 124, 125]</sup> or phthalocyanines<sup>[126]</sup>. In

the case of boron - doped graphitic carbons CVD is usually applied to produce films and coatings.<sup>[100, 127]</sup> Thermolysis and pyrolysis procedures using carbon precursors and boron - rich additives usually generate materials, which rather should be denoted as boronated carbon or B(O) - doped carbons.<sup>[128, 129]</sup> Several  $B_xC_yN_z$  compositions could be successfully synthesised with solid - gas reactions<sup>[130]</sup>, CVD methods<sup>[100, 108]</sup> or by pyrolysis<sup>[131]</sup>. However it has to be noted that in the younger literature BCN(O) materials were confusingly named boron carbon nitrides as well. Like in the case of nitrogen - doped carbon there is also a lot of research, but in this case almost exclusively focussed, on boron and nitrogen enriched graphenes<sup>[132-134]</sup> and nanotubes,<sup>[135, 136]</sup> pseudo - graphenes and BCN nanotubes. Also not much is reported on porous bulk BCN materials, showing the difficulty to modulate the shape of such materials.<sup>[137]</sup> Thermolysis of self - assembled block - co - polymers<sup>[138]</sup> and hard templating based on porous silicas in a CVD setup<sup>[139]</sup> lead to mesoporous BCN materials. Portehault *et al.* recently reported on mesoporous BCN and the respective hydrogen storage.<sup>[137, 140]</sup> They reported as yet the highest achieved specific surface area ( $1560 \text{ m}^2 \text{ g}^{-1}$ ) for BN - rich boron carbon nitrides.<sup>[137]</sup> Wang *et al.* have recently applied boron - doped carbon nitride as metal - free catalyst for aliphatic C - H bond oxidation.<sup>[141]</sup>

Recently, we and others employed carbonisable (*e.g.* cyano containing) ionic liquids (ILs) as direct precursor for the synthesis of bulk material such as nitrogen - doped carbon<sup>[118, 119, 142, 143]</sup> and sulphur - doped carbon<sup>[143]</sup>. ILs are almost non - evaporating and there is no need to apply high pressure, making the synthesis highly facile without technical efforts. Carbons with nitrogen contents as high as 10.4 % with an electronic conductivity superior to graphite and an oxidation stability higher than carbon nanotubes were obtained. This approach has recently been extended *via* careful mechanic analysis on the formation mechanism.<sup>[118]</sup> ILs have the advantage, as stated above, that they are both liquid and due to the salt structure of the substances exhibit a negligible vapour pressure.<sup>[144, 145]</sup> In addition ILs show strong interaction with inorganic surfaces *i.e.* very good wettability. These are very preferable precursor properties, which enable simply processing and shaping without causing safety concerns and high pressure equipment. That way, the precursor may be dip - coated, spun, printed, sprayed or

templated towards nanostructures before or throughout conversion to the final nitrogen - doped carbon in simple inert gas ovens.<sup>[119]</sup>

Interestingly, IL - based carbon materials show up with a comparably low long - range order, nevertheless impressing with properties like electric conductivity and stability, where a high degree of order is expected to be important. Commonly ILs are chosen in a way, that the cation already contains structural nitrogen, *e.g.* pyridinium, pyrrolidinium or imidazolium, while the anion preferentially carries cyano functionalities, because only few, and in particular cyano - containing, ILs can be used for material synthesis without the application of pressure or nanoconfinement.<sup>[143]</sup> The role of cyano - functions is therefore apparently the most important, permitting the first and essential step of materials formation in terms of non - volatility and thermostability. However, nitrogen - rich cations (*e.g.* imidazolium or pyridinium) are highly favourable to achieve nitrogen - doped graphite - like carbons. The pyrolytic treatment of certain ILs leads to carbonaceous materials with different properties, which strongly depend on the reaction temperature.

From the viewpoint of synthesis, IL carbonisation is fairly different from other pyrolysis approaches. First of all, the ionic character itself is promoting the formation of carbonaceous products as no evaporative loss of precursors occurs until the reaction / decomposition temperature is reached. Additionally, the decomposition products may keep the ionic character to a certain extent being trapped for further reactions by the coulomb attraction of the charged reaction medium. Carbonisation experiments with the uncharged relatives of the IL precursors resulted in no solid yield. The chemical characterisation of volatile decomposition products *via* coupled thermogravimetric analysis and mass spectrometry, but also infrared (IR) and nuclear magnetic resonance (NMR) spectroscopy and elemental analysis a condensation scheme have recently been reported. Initiated either by *reverse* Menschutkin reaction or alkyl fragmentation, nucleophilic attack of dicyanamides on aromatic cations together with triazine formation due to cycloaddition are expected to lead to a branched polymer - like network, which subsequently further carbonises into a graphitic nitrogen - doped carbon (Figure B1). However, there are discussions in literature about the required composition of ILs for the



generation of solid carbonaceous material, leaving space for more detailed investigations on the mechanism of solid formation.<sup>[118, 142]</sup>

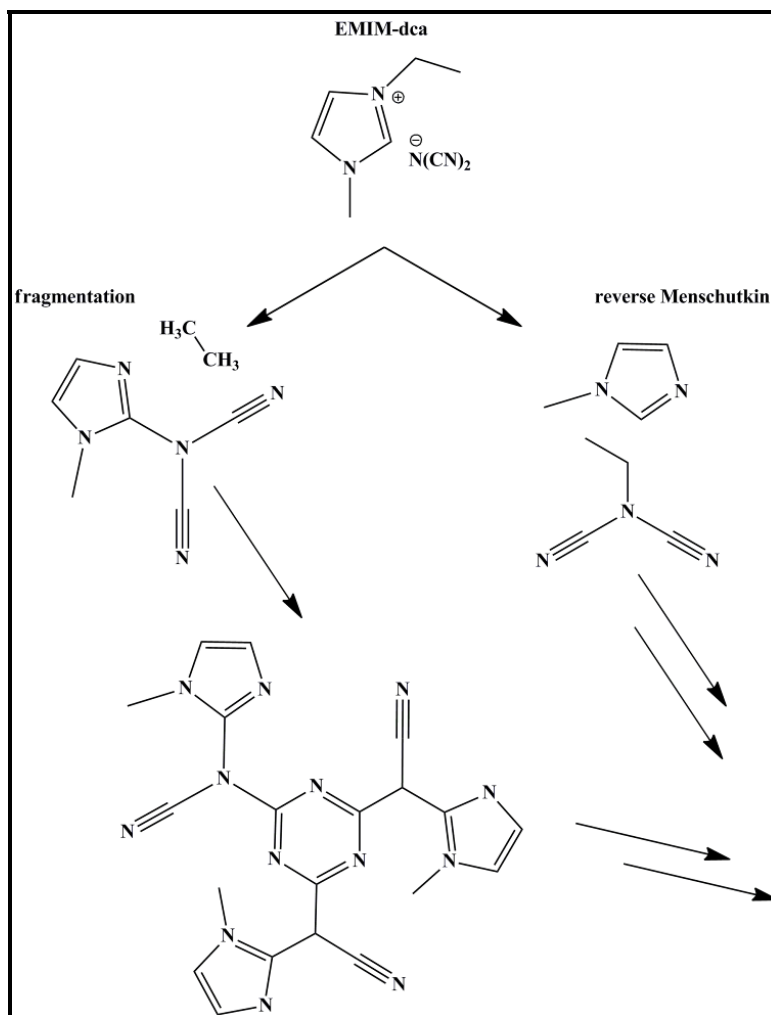


**Figure B1:** Simplified reaction scheme for the pyrolysis of dicyanamide anion - based ionic liquids.

As mentioned before, the good wetting behaviour of ILs on inorganic surfaces is promoting the employment of hard templating approaches. Briefly described the hard templating technique employs stable, often silica - based, solid porous backbone materials (hard templates), which can be infiltrated with precursors of the desired material. Conversion of the precursors produces first a hybrid material, which is further processed into the porous, structurally replicated new material. Successful production of various, highly porous replicas of silica architectures has already been reported,<sup>[119]</sup> opening the way to test these materials for applications (*i.e.* supercapacitors or

electrocatalysis), where accessible surface area and developed porosity are a necessity. However, the removal of the silica template commonly employs hazardous compounds like aqueous ammonium dihydrogen fluoride, representing a drawback in the synthesis of high surface area materials. Additionally, it is a challenge to subtly vary the nitrogen content in carbon materials towards carbon nitrides. Therefore the impact of different additives was studied. The dissolution of inert eutectic salt mixture (LiCl / KCl) in the IL precursors and typical high temperature treatment lead to mainly microporous nitrogen - doped carbon after washing. The salt was grinded and thoroughly mixed with the ionic liquid. The mixture was subsequently placed in an alumina crucible and carbonised in an inert oven under nitrogen flow, which is a standard procedure for the preparation of IL - based products. In this case a heating rate of  $10 \text{ K min}^{-1}$  and 1 h isothermal treatment @  $900 \text{ }^\circ\text{C}$  was used.

The strong interaction of the organic with the inorganic salt most likely only allows nanoseparation of the inorganic salt during the hydrophobicity - inducing ionic liquid condensation process.

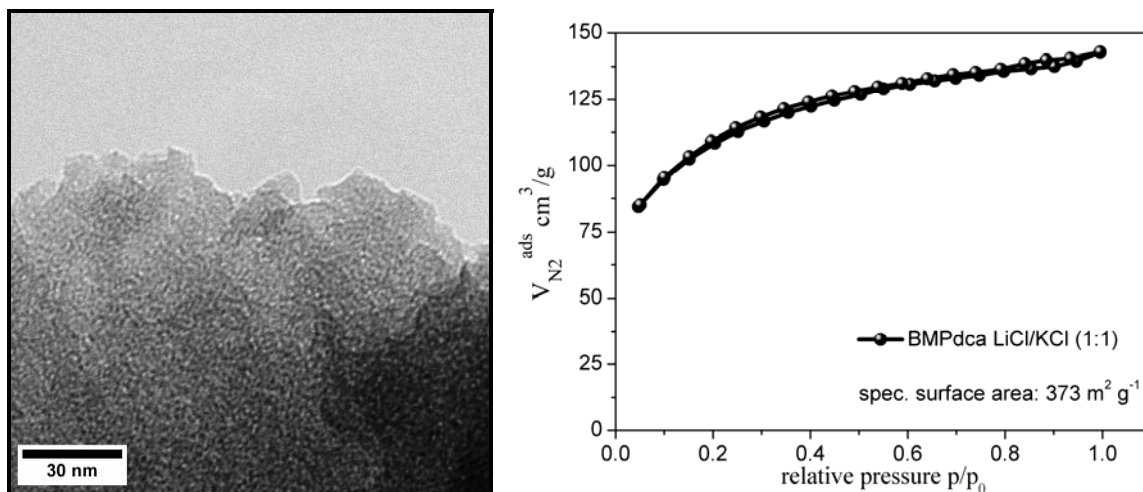


**Figure B2:** TEM image (left) and type I isotherm from nitrogen sorption analysis (right) of microporous nitrogen - doped carbon from “salt templating” approach with eutectic LiCl / KCl additive.

TEM images and nitrogen sorption isotherm of the resulting nitrogen - doped carbon (13 wt. % N) prepared from a 1 g : 1 g approach of the eutectic LiCl / KCl mixture ( $\text{LiCl} / (\text{LiCl} + \text{KCl}) = 0.592$ ) and BMP - dca at  $900 \text{ }^\circ\text{C}$  indicate the generation of

a homogeneous microporosity (Figure B2). The material (*micro* - BMP - dca - 900) presents a reversible type I isotherm (Figure B2/right), characteristic of microporous materials, corresponding to a specific surface area of  $373 \text{ m}^2 \text{ g}^{-1}$ . In the high relative pressure region ( $p / p_0 \sim 0.9$ ) a small hysteresis can be observed. Applying a NLDFT model for cylindrical / slit shaped pores revealed a mean pore diameter of 1.6 nm and a total pore volume of  $0.198 \text{ cm}^3 \text{ g}^{-1}$ . Major contribution to the volume accounts from the micropore region (*i.e.*  $0.178 \text{ cm}^3 \text{ g}^{-1}$ ), implying the minor role of mesoporosity. Ammonium chloride is known to decompose into ammonia and hydrochloric acid at  $338 \text{ }^\circ\text{C}$ . As this is close to the decomposition temperatures of the dca - containing ILs (Emim - dca:  $321 \text{ }^\circ\text{C}$ ; BMP - dca:  $288 \text{ }^\circ\text{C}$ ) experiments were performed employing the inorganic salt as reactive salt additive to the IL - based synthesis. The as - obtained dim grey powders showed enhanced nitrogen contents of up to 40 % and slightly developed microporosity ( $\sim 50 \text{ m}^2 \text{ g}^{-1}$ ). The products are in the context of the thesis not noteworthy, but imply certain reactivity of the developing IL - based condensation product with amines and the possibility to achieve microporosity and further nitrogen doping at the same time by using specific additives. This is of considerable interest in the engineering of sorption materials, but also for the optimisation of carbon electrode materials which can be applied in batteries, supercapacitors and fuel cells. It has to be mentioned that templated high surface area material, which is purified by washing with water had increased oxygen content, most likely caused by partial surface oxidation.

## **B1 Ionic Liquid-Based Nitrogen-Doped Carbons as Highly Active Non-Metal Catalysts for PEMFCs**

Developing catalytic materials for the electrocatalytic oxygen reduction reaction (ORR) is the current technological bottle-neck for the industrial development of polymer electrolyte membrane fuel cells (PEMFCs).<sup>[146-149]</sup> Up to now, the most efficient catalysts for ORR are still precious metal-based materials<sup>[148]</sup> such as platinum, palladium or respective alloys, and these catalysts are not even really feasible. On the one hand, they are characterised by high over-potentials.<sup>[148]</sup> Moreover, the high costs of the pure platinum hampers large-scale application of such fuel cells.<sup>[146-148]</sup> Therefore, the search for non-precious metal as well as metal-free catalysts for the ORR is one of the most active and competitive fields in chemistry.<sup>[91, 92, 146-148]</sup> Nitrogen-doped carbon is already known to enhance the ORR activity of pure carbon causing hope for a metal-free catalyst for the electrocatalytic oxygen reduction,<sup>[146-148],[92, 150-160]</sup> but still on a less competitive level. To achieve high currents at low over-potentials the exchange current density has to be improved. As this is related to the true electrode surface area turning to high surface area materials is a potential solution.<sup>[155, 159]</sup> This can be called “*mesoscopic structure control*”.

In addition, there is much disagreement on the nature of the active site for oxygen reduction in nitrogen-doped carbons. Some believe that transition metals may be “*accidentally*” incorporated during the fabricating process of the carbons materials and then play an important catalytic role during the ORR.<sup>[147, 148, 150, 155, 160]</sup> Others propose that transition metals may not be necessary and that nitrogen-doped carbons possess inherent active sites for ORR.<sup>[92, 146, 151-154]</sup> They propose a variety of N-C-N bonding patterns and local geometries being potentially active. Once the catalytic site is found, another chance for enhancement of the catalytic activity of these systems is increasing the surface density of catalytic sites.<sup>[148, 155, 159]</sup> Together, this can be called “*microscopic structure control*” and some theoretical work on this topic has recently been reported.<sup>[161, 162]</sup>

Improving ORR activity in metal-free nitrogen-doped carbon materials with high surface area would allow more detailed insight into precautions for ORR-active

sites.<sup>[92, 146, 152]</sup> Beside this rather scientific question also the application side may profit on this, as a non - precious metal catalyst based on simple carbon structures may enable the fabrication of cheap and sustainable next generation PEMFCs. Herein one could think of a concept were such carbons serve as support for metal - based catalysts, but at the same time contribute to the catalytic activity itself. In addition to the expected important features of novel non - metal catalysts, well - known important features for electrocatalysts such as electric conductivity and stability should be improved as well. As the former described nitrogen - doped carbons possess improved conductivity and stability compared to other carbons and are easy to design in their mesoscopic structure, electrochemical tests were expected to give interesting results.

Similar to previously reported commercial silica (*i.e.* Ludox<sup>®</sup> particles were employed as hard template),<sup>[119]</sup> we investigated a ratio of Emim - dca / silica of 1 g : 1 g and performed pyrolysis under nitrogen flow at 1000 °C (heating rate 10 K min<sup>-1</sup>, 1 h isothermal @ 300 °C and 1 h @ 1000 °C). Subsequent removal of the silica template employing 4 M NH<sub>4</sub>HF<sub>2</sub> solution (40 mL g<sup>-1</sup>) and washing with distilled water, gave the porous nitrogen doped replica, as fine black powder (*meso* - Emim - dca - 1000). TEM imaging showed the obvious mesoporosity of the carbon material (Figure B3/left). The replication of the silica nanoparticles can be clearly recognised.

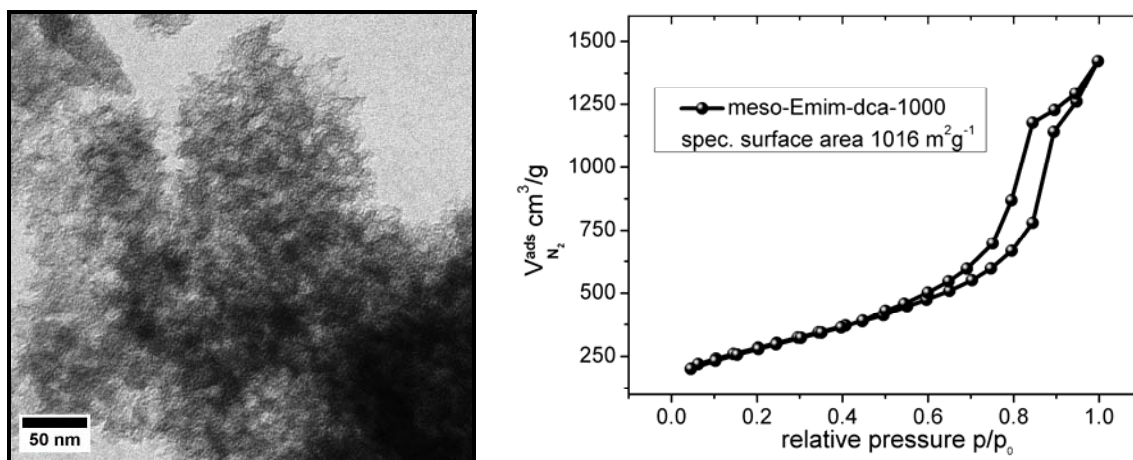


**Figure B3:** TEM image (left) and type IV nitrogen sorption isotherm (right) of *meso* - Emim - dca - 1000.

Gas sorption measurements were applied for more detailed investigation of the porosity (Figure B3/right). Confirming the observations from TEM, a specific surface

area of  $1016 \text{ m}^2 \text{ g}^{-1}$  was obtained. The characteristic reversible type IV isotherm (with significant hysteresis) indicates the mesoporous character of the material. Pore size analysis *via* a NLDFT model for cylindrical / slit shaped pores, gave a mean pore diameter of 13.5 nm. This value agrees with the electron microscopically observations and match the reported radius ( $r_g$ ) of 6.6 nm of the commercial silica particles very well.<sup>[163]</sup> A mesopore volume of  $1.84 \text{ cm}^3 \text{ g}^{-1}$  and a mesopore volume of  $1.68 \text{ cm}^3 \text{ g}^{-1}$  was obtained, demonstrating the majority of the porosity lays in the mesopore range. An elemental composition of 74.2 % C, 8.8 % N and 1.2 % H was determined (*via* elemental analysis), which again implies remarkable oxygen content, apparently characteristic for these high surface area carbon materials.

To perform electrochemical testing a standard ink was prepared from 5 mg of catalyst with 95  $\mu\text{l}$  Nafion® binder solution and 350  $\mu\text{l}$  of ethanol. A 7  $\mu\text{l}$  aliquot was applied to a freshly polished glassy carbon rotating - disc electrode (diameter  $\sim 5 \text{ mm}$ ) to prepare a catalyst thin film. Electrochemical tests were performed in 0.1 M KOH solution in a standard three - electrode setup with an Ag / AgCl reference electrode using Gamry Reference 600 potentiostat (Gamry Instruments) and Gamry EIS 300/Physical Electrochemistry software. Cyclic voltammogram (CV) and the LSV polarisation curves were recorded at various rotation rates and compared to a commercial platinum catalyst example (Figure B4). The cyclic voltammogram for *meso* - Emim - dca - 1000 shows a nearly rectangular shape, indicating the high conductivity of the material (Figure B6/left).

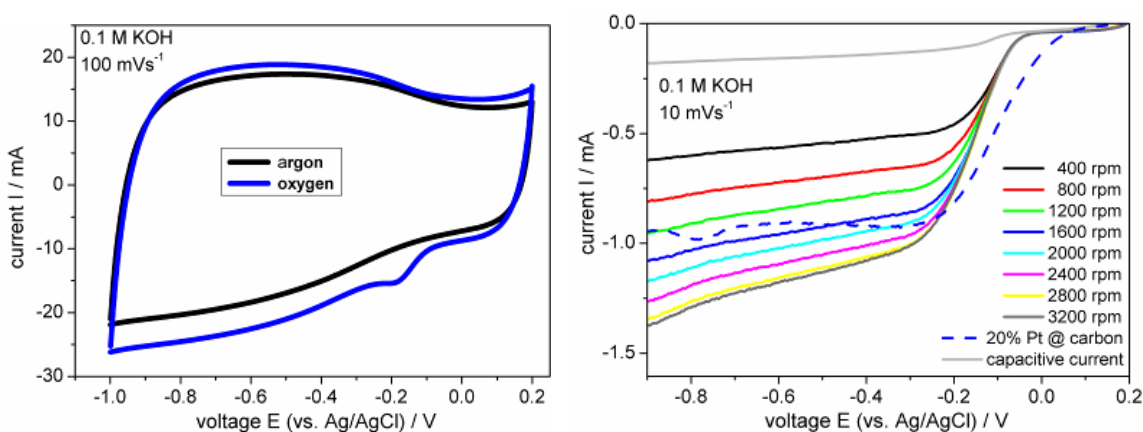


**Figure B4:** Cyclic voltammograms of *meso* - Emim - dca – 1000 in deaerated and oxygen - saturated 1 M aqueous KOH (left). RDE - LSV experiments with polarisation curves in oxygen - saturated 1 M aqueous KOH at different rotation rates compared to commercial 20 wt.% Pt on carbon catalyst right (right).

The absence of sharp redox peaks, which are expected for transition - metal compounds, can be regarded as a hint on the metal - free character of the catalyst. The appearance of a faradaic peak at rather high voltage (-183 mV) in the presence of oxygen indicates the high activity towards oxygen reduction. Remarkably, in the linear sweep experiments the catalyst reveals high current densities, which at low voltages ( $\sim -460$  mV) even exceeds commercial Pt catalyst (20 wt. % Pt @ carbon). The reaction sets in at  $\sim -15$  mV vs. Ag / AgCl. Employing the measured currents at -3.5 V in the RDE experiments, more detailed analysis of the reaction mechanism were carried out. A Koutecky - Levich Plot, where the actually measured characteristic slope is compared to the slopes of pure 2 and 4 electron processes indicates that the reaction is close to the ideal 4 electron process (Figure B5), with a value of  $n = 3.58$  for the electron transfer number of *meso* - Emim - dca - 1000.

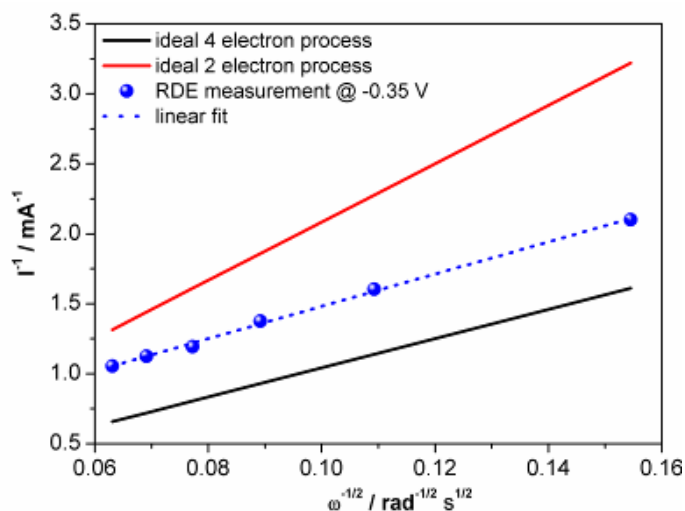


**Figure B5:** Kouteck - Levich plot derived from RDE experiments with *meso* - Emim - dca - 1000 at -3.5 V vs. Ag / AgCl .

The astonishing electrocatalytic performance of the IL - based material in alkaline medium corroborates the expected catalytic activity of nitrogen - doped carbons in a way, which strongly emphasises that C - N motifs create the active sites, and not residual trace metal content. Inductively coupled plasma optical emission spectrometry (ICP - OES) gave a value of 0.07 % Fe, which is in relation to the high catalytic activity very low. For further investigations of the above mentioned “*microscopical* and *mesoscopical structure*

*control*” nucleobases were employed as nitrogen donating additives, which at the same time create microporosity, like described on the example of ammonium chloride. According to XPS, surface nitrogen contents between 9.0 and 11.8 % could be achieved in templated materials prepared like meso - Em, which showed nitrogen content of 8.8 %. Specific surface areas could be enhanced to an excess of 1500 m<sup>2</sup>g<sup>-1</sup>. Detailed electrochemical testing showed slightly improved catalytic activity compared to the pure nitrogen - doped carbon equivalent. Further details can be reviewed in “Efficient Metal - Free Oxygen Reduction in Alkaline Medium on High - Surface - Area Mesoporous Nitrogen - Doped Carbons Made from Ionic Liquids and Nucleobases” (“*Journal of the American Chemical Society* 2011, 133, 206.).

High resolution N 1s XPS spectra revealed, that neither increased overall nor increased specific nitrogen contents such as pyridinic, pyrrolic, quaternary or N - oxidic (all present within all nucleobase - modified nitrogen - doped carbons) lead to the resulting extra activity.<sup>iii</sup> Contradicting results about the catalytic activity of pyridinic nitrogen sites were published recently, indicating a flourishing research area, which still suffers from the complexity of the chemically and structurally very broad materials.<sup>[164],[165]</sup> A representative N 1s XPS spectrum (*meso* - EmG with guanine used as additive) reveals the presence of pyridinic (40.8 % at 398.5 eV), pyrrolic (20.2 % at 399.8 eV), quaternary (26.0 % at 401.0 eV) and few N - oxidic (12.9 % at 403.1 eV) nitrogen (Figure B6).

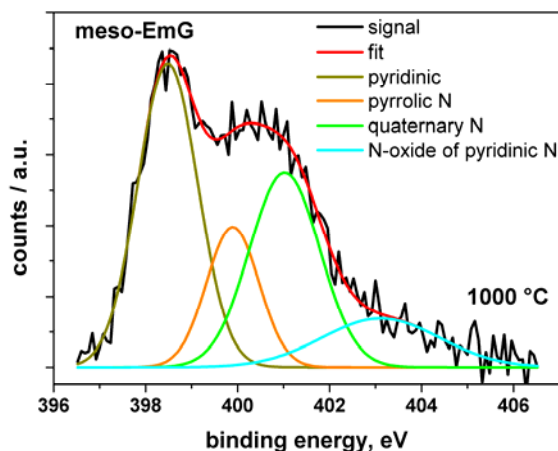


**Figure B6:** High resolution N 1s XPS spectrum of *meso* - EmG (Emim - dca / guanine - 1000).

<sup>iii</sup> A correlation of the ORR activity to the amount of metal traces was also not observed.



## **B2 Mesoporous Nitrogen – Doped Carbon for the Selective Electrocatalytic Synthesis of Hydrogen Peroxide**

The results of this section were achieved in collaboration with Dipl. - Chem. Frédéric Hasché and therefore will again be reported and discussed in a separate context.

Mechanistic analysis of the catalysed reduction of oxygen of the presented materials demonstrated that in most cases the number of transferred electrons was not four, like theoretically expected for the complete reduction of O<sub>2</sub> to H<sub>2</sub>O, but also lower, uneven values between  $n = 3.2 - 4$  were received. This information hints towards mixed processes indicative of the varying reactivity of different nitrogen - doped carbons, even if there was no clear dependence on specific C - N sites, such as pyridinic, pyrrolic or quaternary nitrogen, found. Nevertheless the observation causes the hope to find a selective and efficient electrocatalyst for a pure 2 electron process towards the conversion of oxygen into hydrogen peroxide on the basis of nitrogen containing conductive carbons. As respective catalysts showed impressive activities even in the acid medium,<sup>[91]</sup> the development of classical membrane reactors for the production of hydrogen peroxide appears reasonable.<sup>[166]</sup> Theoretical considerations on quaternary nitrogen in graphite layers (Sidik *et al.*) suggest a feasible reduction mechanism of oxygen. Activation of adsorbed oxygen by “*radical*“ carbon atoms strongly bound to nitrogen indicate a 2 electron mechanism.<sup>[167]</sup> Okamoto *et al.* were able to deduce an enforced adsorption of oxygen molecules on C=C double bonds from simulations, if the number of neighbouring nitrogen atoms is increased, suggesting participation of a 2 and 4 electron process in their system.<sup>[166]</sup>

Hydrogen peroxide (H<sub>2</sub>O<sub>2</sub>) is one of the most relevant chemicals of all. The fame of the pale blue liquid results from its unique properties as a “*green*” and at the same time highly efficient oxidising agent. Combined, these properties lead to almost ubiquitous applications (*e.g.* in water treatment, oxidation reactions in chemical industry, cleaning agents in household and industry or as propellant).<sup>[97, 168]</sup> Main consumers of this weak acid are the pulp and paper industry, where it is used as bleaching agent. Hydrogen peroxide is one of the 100 most important industrial produced chemicals worldwide.<sup>[169]</sup>

Today, hydrogen peroxide is mainly produced *via* the so - called anthraquinone oxidation (AO) process. The procedure includes sequential hydrogenation and oxidation in organic solvents followed by extraction and, depending on the desired product, distillation for purification of the as - prepared H<sub>2</sub>O<sub>2</sub>. This effort is still coupled to relatively high energy consumption and therefore a clearly improvable process.<sup>[97]</sup> Additionally, decomposition of anthraquinone leads to a further decreased efficiency.<sup>[170]</sup> For these reasons intensive research activities are ongoing to develop alternative production courses.<sup>[97]</sup>

The catalytic direct synthesis of H<sub>2</sub>O<sub>2</sub> from elemental hydrogen and oxygen would be a tremendous advancement and the most elegant way. The main problem in the catalytic formation of hydrogen peroxide lies in even its high oxidation potential. O<sub>2</sub> can react to H<sub>2</sub>O<sub>2</sub> by reductive hydrogenation (2 electron process) accompanied by the gain of energy. Similarly, H<sub>2</sub>O<sub>2</sub> can undergo reductive hydrogenation towards H<sub>2</sub>O (2 electron process), which is even more favoured. Commonly employed catalysts (Pd, Pt, Ag, Au)<sup>[171, 172]</sup> conduct both reaction pathways, and therefore the direct reduction to water (4 electron process) at the same time. Adjusting process parameters like the hydrogen partial pressure, hydrogen peroxide can be produced as kinetic product in a medium efficient way. However, the danger of explosion is dramatically increased that way. This is one reason why no direct industrial process has been implemented so far.<sup>[173]</sup>

Electrochemical processes avoid hazards, either by using electrons instead of hydrogen as reducing agent or by spatial detachment of the oxidation of hydrogen and the reduction of oxygen, like in polymer electrolyte membrane fuel cells (PEMFCs). This minimises the danger of explosion as well known from fuel cell technology. Glassy carbon and pyrolytic graphite catalyse the 2 electron process at high pH and can therefore be used to produce H<sub>2</sub>O<sub>2</sub> electrochemically.<sup>[170]</sup> However, the activity is rather low and leads to high over - potential, a direct measure for the energetic efficiency. Within the Dow process graphite plate electrodes are used this way to synthesise lower quality hydrogen peroxide solutions in basic medium at high working voltages of up to 2 V.<sup>[174, 175]</sup> The product of restricted quality is limited to the application of pulp bleaching.<sup>[168]</sup> An advantageous approach in the production of H<sub>2</sub>O<sub>2</sub> using fuel cell type of reactors.<sup>[176, 177]</sup> Significant optimisations on this technology, even at high pH values, encourage further catalyst research and commercial implementation.<sup>[173, 178]</sup> In previous catalyst research organic

modifiers (e.g. surfactants,<sup>[179]</sup> anthraquinone,<sup>[180]</sup> 2-ethylanthraquinone<sup>[181]</sup>) in combination with porous carbon electrodes were used to improve the efficiency. However, for the efficient electrochemical production of hydrogen peroxide there is still a lack of adequate and cheap catalyst.

In this section the synthesis of mesoporous nitrogen - rich carbon with high activity for the electrocatalytic reduction of oxygen to hydrogen peroxide even in acid medium is reported. According to the already in detail described method, BMP - dca was employed as direct precursor for the synthesis of metal - free nitrogen - rich carbon (BMP - 800) at 800 °C (heating rate: 10 K min<sup>-1</sup>, isothermal 1 h) again using Ludox® silica nanoparticles (1:1) as hard template.<sup>[119]</sup> High resolution transmission electron microscopy (HRTEM) revealed a low long - range ordered characteristic structure of nitrogen - doped carbons derived from ionic liquid precursors for BMP - 800 (Figure B7/A). Graphite - like sheets are bent due to the high amount of structurally integrated nitrogen (16.2 wt. %). As previously mentioned, doping leads to high electric conductivity and stability and therefore to highly desired properties for electrocatalysis in the case of BMP - dca already at synthesis temperatures of 800 °C.<sup>[119]</sup> Employing the previously discussed hard templating strategies (section B1), commercial silica nanoparticles (Ludox®HS40) were employed to introduce porosity into the IL - derived carbon, defining porosity and generating high specific surface area. The porous carbon produced is denoted as *meso* - BMP - 800. The successful introduction of mesopores was initially demonstrated *via* TEM imaging, demonstrating the replicated inorganic nanoparticles structure after carbonisation of the hybrid silica / ionic liquid material and subsequent removal of the template (Figure B7/B).

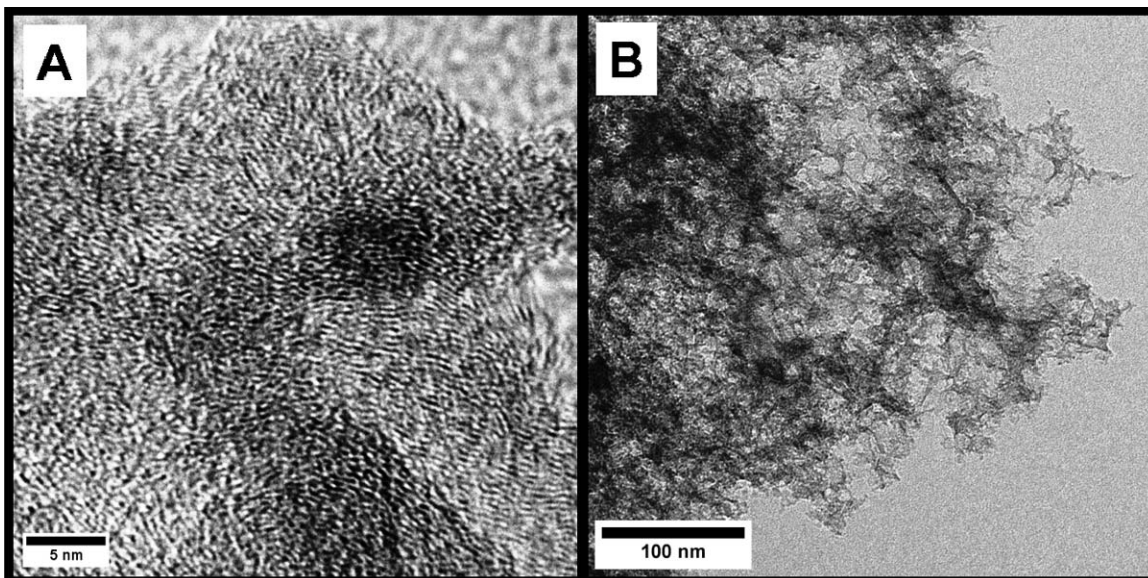


**Figure B7:** Transmission electron micrographs of (A) BMP - 800 and (B) *meso* - BMP - 800.

Nitrogen sorption measurements on *meso* - BMP - 800 confirm the high specific surface area of  $318 \text{ m}^2 \text{ g}^{-1}$ , which at the same time is the catalytically active surface. A type IV isotherm with distinct hysteresis was observed, indicating the abundance of mesopores (Figure B8/left). Pore analysis *via* a NLDFT model for slit and cylindrical shaped pores, reveals a mean pore diameter of 13.2 nm, corresponding well with pore diameters measured from TEM images and the reported radius  $r_g$  of 6.6 nm of the commercial silica particles.<sup>[163]</sup> Wide angle X - ray scattering (WAXS) show characteristic inter- (002) and intralayer (101) diffraction at  $2\Theta = 26.14^\circ$  und  $42.98^\circ$  and confirm the removal of silica template (Figure B8/right).

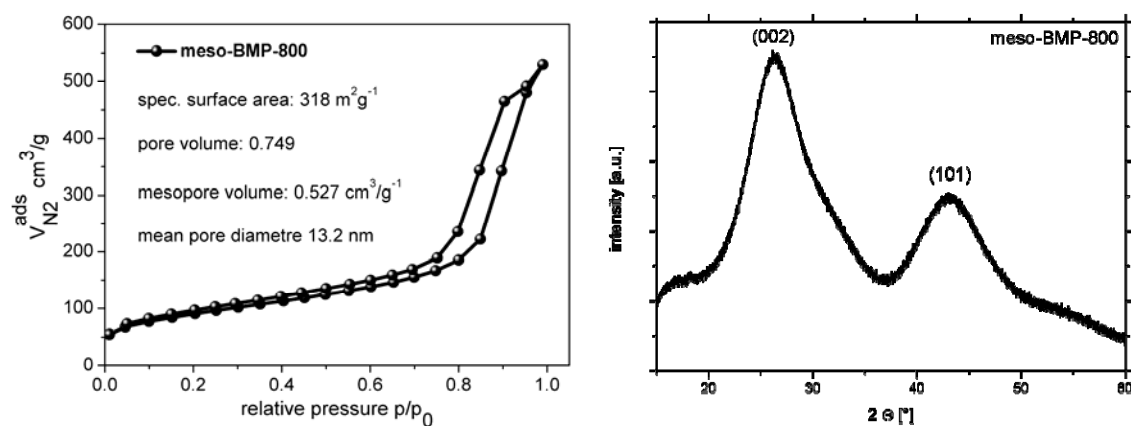


**Figure B8:** Nitrogen sorption isotherm (type IV) of *meso* - BMP - 800 (left). WAXS diffractogram of *meso* - BMP - 800 (right)

The mean interlayer distance of 340.6 pm is relatively long in comparison to graphite (335.4 pm), due to a bent carbon structuring (as observed by HRTEM). As evaluated by XPS and elemental analysis, the nitrogen content of 14.2 wt.% (XPS) / 17.17 wt.% (EA) is very high. The variation of the values can be explained by the surface specificity of XPS measurements. XPS measurements at the same time confirmed the metal - free character of the catalyst (Fe content 0 % and no indication on other metals; see Appendix).

For the electrochemical characterisation of the *meso* - BMP - 800 catalyst the rotating - disc electrode (RDE) technique was used (Figure B9/left). Well - polished glassy carbon electrodes were prepared, coated with the catalyst and employed in RDE experiments in 0.1 M HClO<sub>4</sub>. The polarisation curves at various rotation rates and the cyclic voltammogram (CV) were recorded. The CV profile for *meso* - BMP - 800 shows a nearly rectangular shape indicating the high conductivity of carbon and an increased capacitive current compared to the commercial carbon (Figure B9/left, inset).

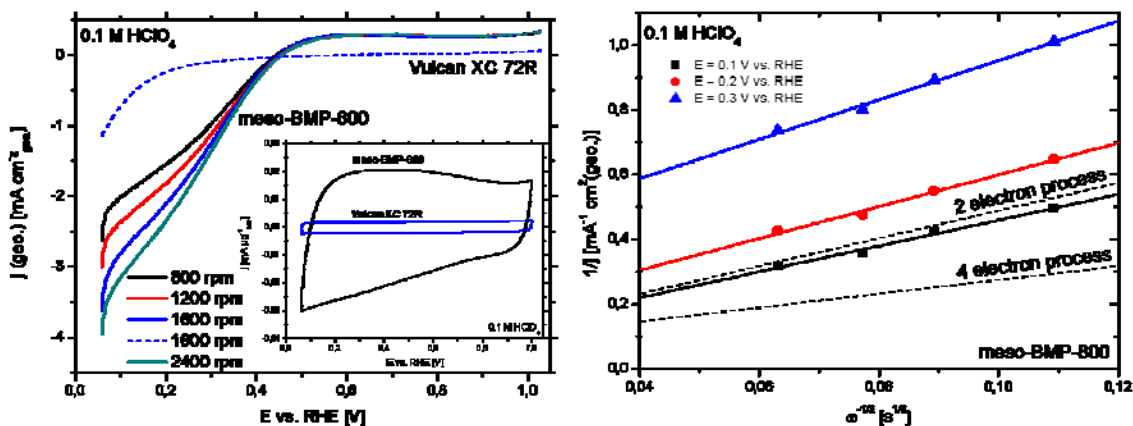
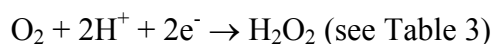


**Figure B9:** Electrochemical characterisation of the *meso* - BMP - 800 - catalyst compared with the commercial Vulcan XC 72R carbon: Polarisation curves at various rotation rates in oxygen - saturated 0.1 M HClO<sub>4</sub> and cyclic voltammogram (inset) in deaerated 0.1 M HClO<sub>4</sub> (left). Koutecky - Levich plot for the determination of the transferred electrons during the reaction (right).

The absence of any sharp redox peaks, as expected for transition - metal compounds, can again be interpreted as a hint to the metal - free nature of the catalyst generated by the synthesis strategy. Remarkably, in the presence of oxygen the catalyst reveals high current density polarisation curves and strongly reduced over - potentials as

compared to the commercial carbon (Vulcan XC 72R, specific surface area 208 m<sup>2</sup> g<sup>-1</sup>). Even if comparatively lower than the Emim - dca - based carbons produced at 1000 °C, *meso* - BMP - 800 exhibited high catalytic activity for the ORR, even in acidic medium. The KL plot for *meso* - BMP - 800 at various electrode voltages was recorded (Figure B9/right). It is observed that the experimental determined slope is in good agreement with the theoretical calculated slope for a 2 electron process. From the experimental data, the “*B factor*” is calculated to 0.21 ± 0.04 mA cm<sup>-2</sup> s<sup>1/2</sup>, exhibiting deviation of < 9 % compared to the theoretical value for a 2 electron process. Thus, the electrochemical analysis confirms the catalytic activity of *meso* - BMP - 800 for the selective hydrogen peroxide production with a 2 electron process in acid medium following the reaction equation:



High resolution XPS spectra of the nitrogen N1s signal show the presence of pyridinic (43.8 % at 398.4 eV), pyrrolic (17.8 % at 399.8 eV), quaternary (33 % at 401.0 eV) and few N - oxidic (6.1 % at 402.9 eV) nitrogen (Figure B10). The only difference compared to former described IL - derived porous carbons at 1000 °C is the increased relative appearance of pyridinic and quaternary nitrogen.<sup>[119]</sup> As such, a precise attribution of catalytic activity to a specific binding site seems rather speculative. Beside the importance of an increased nitrogen content retaining sufficient conductivity, (see Okamoto *et al.*<sup>[166]</sup>), another possible factor on the reactivity is the degree of graphitisation. Here, the polarisability of the graphitic layers should influence the adsorption properties, while the elongation of the conjugated  $\pi$  - system could determine crucial electronic properties. As the radical character of nitrogen - bound carbon, reference to Sidik *et al.*, supports the 2 electron process less conjugated  $\pi$  - systems should be more favoured for hydrogen peroxide synthesis.<sup>[167]</sup>

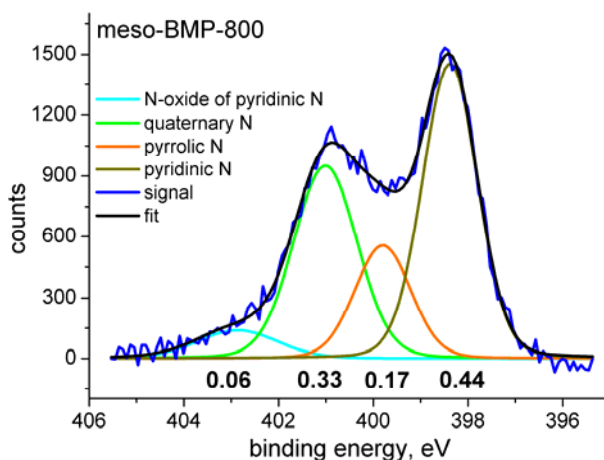


**Figure B10:** High resolution N 1s XPS spectrum of *meso* - BMP - 800. The values under the deconvoluted curves show the relative intensities of the respective binding motifs.

Further, the electrochemical  $\text{H}_2\text{O}_2$  production and accumulation with photometrical and colourimetric methods was further tested and verified (Figure B11). For that, the  $\text{H}_2\text{O}_2$  was produced in very small scale using the simple three electrode catalyst test setup with a rotation speed for the working electrode of  $1600 \text{ U min}^{-1}$  in acid medium and  $\sim 60 \mu\text{g}$  catalyst layer. The electrolyte ( $0.1 \text{ M HClO}_4$ ) was continuous gas flushed ( $226 \text{ ml min}^{-1}$ ) with  $\text{O}_2$  and the working voltage was set constant to  $U = 0.1 \text{ V (vs. RHE)}$ , the high yield range and the resulted current was  $-0.01 \text{ A mg}^{-1}$  catalyst. The  $\text{H}_2\text{O}_2$  production over time was also investigated *via* colorimetric test strips purchased from Merck KGaA. The clear blue colour of the strips confirmed the significant concentration of hydrogen peroxide after a few minutes in the test cell.

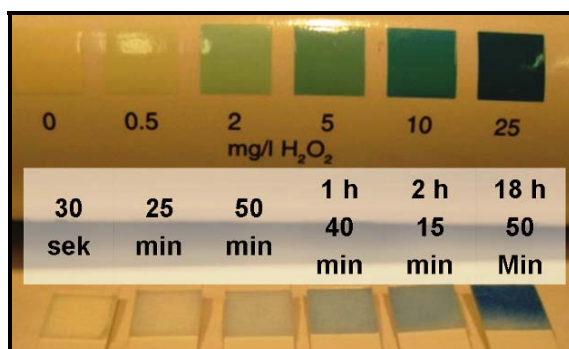


**Figure B11:** Colorimetric determination of  $\text{H}_2\text{O}_2$  (*via* Merck peroxide test strips) during the time. The  $\text{H}_2\text{O}_2$  was synthesised electrochemically with non - metal catalyst in  $0.1 \text{ M HClO}_4$ .

For more detailed quantification, samples were taken after certain points of time, neutralised, brought to colour reaction as instructed for the peroxide test with commercial peroxide test and measured photometrical (Figure B12), with the Beer - Lambert law used to evaluate the effective peroxide concentrations.

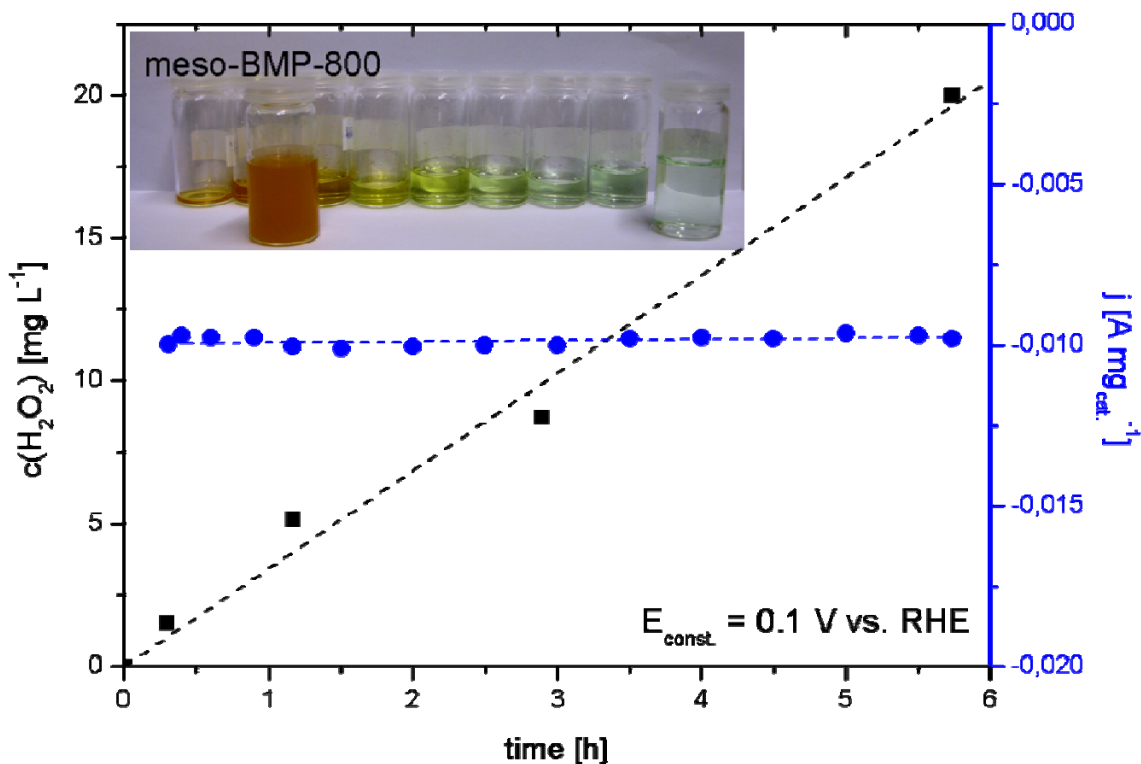


**Figure B12:** Current and concentration behaviour with time for the electrochemical  $\text{H}_2\text{O}_2$  production.

The electrochemical production of hydrogen peroxide with defined concentration (here up to  $20 \text{ mg l}^{-1}$ ) is possible at low operating voltage ( $0.1 \text{ V vs. RHE}$ ) in a few hours (Figure B12). Current and  $\text{H}_2\text{O}_2$  formation remain stable at constant working voltage over 5.5 hours. The theoretical specific electrical energy required to produce one gram of hydrogen peroxide is  $W_{\text{spec}} = 0.157 \text{ Wh g}^{-1}$ , with the number of transferred electrons ( $z = 2$ ; following the equation in Figure B13), the Faraday constant and the molar mass of  $\text{H}_2\text{O}_2$ . The actual (practical) energy expended is  $0.241 \text{ Wh g}^{-1}$  with the mean current  $I = 0.63 \text{ mA}$ , the reaction time  $t = 5.74 \text{ h}$ , the working voltage  $U = 0.1 \text{ V vs. RHE}$  and the resulted mass of  $\text{H}_2\text{O}_2$   $m = 1.5 \text{ mg}$  (calculated from concentration and electrolyte volume). Hence the Faraday efficiency  $\epsilon_f$  was found to be 65.15 %.



$$W_{spec} = \frac{z \cdot F \cdot U}{M} = \frac{Q \cdot U}{m} = \frac{I \cdot t \cdot U}{\epsilon_f \cdot c_m \cdot V}$$

theoretical ↙  
practical ↘

**Figure B13:** Equation for the specific electrical energy  $W_{spec}$ . Number of transferred electron -  $z$ , Faraday constant -  $F$ , voltage -  $U$ , molar mass -  $M$ , electrical charge -  $Q$ , mass -  $m$ , current -  $I$ , time -  $t$ , Faraday efficiency -  $\epsilon_f$ , mass concentration -  $c_m$  and volume -  $V$ .

The use of as-presented cheap non-metal electrocatalysts in an adequate production setup, such as a fuel cell type flow reactor is especially, but not exclusively attractive in terms of flexibility. Hydrogen peroxide could be synthesised in small amounts directly at the place of need (e.g. in a washing machine)<sup>iv</sup> and at the right point of time. Additionally, the method is very cheap (regarding electricity 2.4 EUR cents  $\text{kg}^{-1}$   $\text{H}_2\text{O}_2$  at 10 EUR cents per  $\text{kWh}^{-1}$  industry price), while costs for the transport of liquid hazardous  $\text{H}_2\text{O}_2$  could fall apart.

<sup>iv</sup> As the washing process is carried out at basic pH it is mentioned, that equivalent electrochemical tests were also carried out in 0.1 M KOH, giving even higher catalytic activity. This can be expected for carbon materials, however typical fuel cells run in acidic medium and at high pH peroxides rather than precisely hydrogen peroxide are produced.

### **B3 Ionothermal Synthesis of Graphitic Boron Carbon Nitride: Reaction mechanism, chemical structure and physicochemical properties**

In the last two sections, highly efficient non-metal catalysts derived from ILs have been discussed. Such carbons, reaching the activity of commercial precious metal catalysts, were produced for the 4 electron pathway desired in hydrogen fuel cells and for the 2 electron pathway, which is desired in hydrogen peroxide synthesis. The materials present interesting and partly contradictive appearing properties. Although possessing a bent graphitic and therefore rather unordered structure, the products show high order-related properties like high electric conductivity and oxidation stability.<sup>[118, 119]</sup> A structural impact on the highly desired electrochemical properties cannot be excluded. Generally, the IL route is not limited to nitrogen-doped carbons. Boron, as well as Sulphur-doped carbons were already reported but not well investigated.<sup>[143]</sup>

With increasing amount of boron and nitrogen, B / N co-doped CNTs (BNCNTs),<sup>[182-184]</sup> boron carbon nitride nanotubes (BCNNTs)<sup>[185, 186]</sup> and boron nitride nanotubes (BNNTs)<sup>[187-189]</sup> are reported in literature. They enrich the manifold of nanostructures each contributing with individual properties. Ozaki *et al.* reported on the ORR activity of B / N-doped carbons.<sup>[112]</sup> In this context surprisingly nothing is reported on the electrocatalytic properties of boron carbon nitride nanostructures, neither the respective bulk material.

Like previously mentioned IL-based materials are exceptional in some points. Beside the simplicity of synthesis, templating strategies are easy to employ. This can lead to mesostructure designed carbons. The microscopic structure, although apparently unordered leads to highly desired physical and chemical properties. To get further insight into the interdependence of structure and property, the new synthesis concept was expanded on boron- and nitrogen-rich carbon *i.e.* the synthesis of boron carbon nitrides applying 1-Ethyl-3-methylimidazolium-tetracyanoborate (Emim-TCB) as cyano-containing, liquid ionic; direct boron, carbon and nitrogen precursor for solid material synthesis. As mentioned, only few and in particular cyano-containing ILs can be used for material synthesis without the application of *e.g.* pressure or nanoconfinement.<sup>[143]</sup> It was stated, that cycloaddition of cyanide species, forming triazine networks, is the

fundamental solid formation step.<sup>[118, 119]</sup> Fulfilling all the essential features, *i.e.* being a non - evaporating liquid salt at room temperature, exhibiting cyano - functions and nitrogen - rich cations, we chose Emim - TCB (Figure B14) as direct precursor for the generation of solid nitrogen - containing carbon. The additional boron content was expected to lead to B / N - containing carbon material.

Structural product features, like order or crystallinity are investigated applying wide - angle X - ray scattering (WAXS) and high resolution transmission electron microscopy (HRTEM) of the derived material. Further on, the chemical composition and electronic properties of the material are determined *via* Raman spectroscopy, electron energy loss spectroscopy (EELS), nuclear magnetic resonance (NMR) spectroscopy, and X - ray photoelectron spectroscopy (XPS). Thermogravimetric analysis coupled with infrared spectroscopy and elemental analysis is further used to investigate the mechanism of solid formation. Finally, a porous boron carbon nitride is produced by the employment of “salt templating” strategies and tested in a standard rotating - disc electrode (RDE) setup for the electrocatalytic oxygen reduction reaction (ORR).

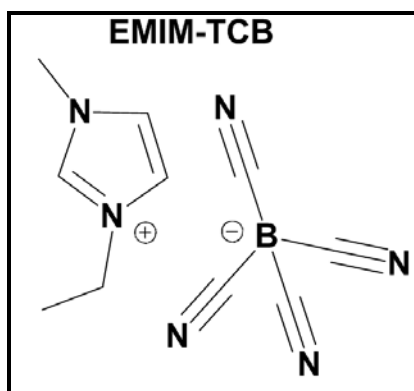
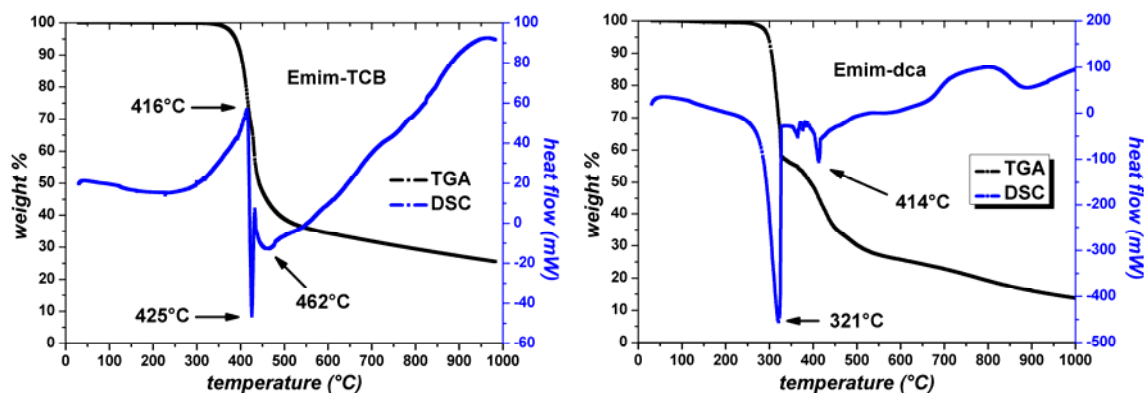


**Figure B14:** Molecular structure of *N,N'* - ethylmethyl - imidazolium - tetracyanoborate (EMIM - TCB)

Although detailed investigations on the mechanism of material formation by IL pyrolysis were recently reported, there are still discussions in literature about the required composition of ILs. Lee *et al.* reported on carbonisation of ILs with cyano - functionalised cations,<sup>[142, 190]</sup> which appeared contradictory to results of Paraknowitsch *et al.*, who observed total decomposition into volatile species in such cases. As Emim - TCB is structurally close to already well - understood ILs and not yet investigated in detail, it is worth to have a detailed look on the mechanistic differences between the

already reported (dicyanamide) and the tetracyanoborate anions.<sup>[118, 142]</sup> To compare Emim - TCB with Emim - dca, coupled thermogravimetric analysis (TGA) and differential scanning calorimetry (DSC) measurements under nitrogen gas were first applied to achieve a better understanding of the decomposition / condensation scheme (Figure B15). Characteristic temperatures for the TGA measurement were evaluated from the first derivative of the mass loss with temperature.



**Figures B15:** TGA / DSC analysis between 0 and 1000 °C of Emim - TCB (left) and Emim - dca (right) under nitrogen gas.

The exothermic decomposition of Emim - TCB sets in at around 250 °C reaching a maximum heat flow at 416 °C (see DSC). The exothermic reaction leads to a strong mass loss of ~ 50 % reaching its maximum at 416 °C in agreement with the calorimetric results (see DSC). In context with the starting decomposition an endothermic peak can be observed at 425 °C in the calorigram. Obviously, the decomposition creates volatile species, but leaves reactive non - volatile fragments, which subsequently condensate to form a glassy, black solid. Potentially, the ionic character is retained and facilitates the solid materials formation due to coulomb attraction. A second endothermic decomposition / condensation step sets in at ~ 431 °C, reaches the maximum heat flow at 462 °C and causes a weaker mass loss of ~ 10 % at 462 °C (TGA). This second reaction creates a comparably broad peak, which seems to contain other distinct peaks, emerging as weak shoulders. The broadening may be explained, either by an overlapping manifold of occurring reactions or by constricted diffusion caused delayed reactions. Hence, the mentioned reaction(s) occur in a rather viscous or glass - like state, which should still

offer certain mobility. Across the higher temperature range, a further small but steady mass loss can be observed. At 1000 °C, a shiny black solid residual mass can be obtained in 25.5 % yield. The already well - investigated pyrolysis of Emim - dca sets in with an endothermic peak already at 205 °C reaching a maximum heat flow at 321 °C (see DSC). The endothermic reaction leads to a first mass loss of ~ 40 % reaching its maximum at 321 °C in agreement with the calorimetric results (see DSC). Two more endothermic peaks occur at temperatures of 365 °C and 414 °C leading to a second mass loss of another 30 %. Like for Emim - TCB an ongoing small but steady mass loss can be observed with further increasing temperatures. In contrast to Emim - TCB accompanied by an exothermic broad shoulder between 700 °C and 900 °C. At 1000 °C the thermal decomposition yields 13.6 % residual mass. Because of the compositional similarity it can be naively expected, that the additional cyano - function causes the higher yield of Emim - TCB. This would corroborate the key role of cycloadditions in the generation of solid.

Despite the increased pyrolysis yield of Emim - TCB and the almost opposite enthalpic behaviour to Emim - dca, another remarkable difference is the characteristic decomposition temperature of 416 °C, which is compared to 315 °C strongly shifted to higher temperatures. Obviously, the cyanide complex with the less electronegative boron leads to a reduced reactivity towards decomposition compared to the covalently nitrogen bound derivative *i.e.* the dicyanamide. As the first DSC signal in both cases is directly accompanied with mass loss the proposed cycloaddition sets in after first decomposition steps. However, the exceptional stability of Emim - TCB opens the possibility to come even closer to the regime of bond pyrolysis still within the liquid state, where mobility compared to typical solid - state pyrolysis reactions is strongly increased due to convection. This might open up access to kinetic high temperature products.

As the concept of using ionic liquids as carbon precursors is rather new, there is only little literature about the materials formation and its mechanism. The broad interests in the thermostability of ionic liquids lead to some investigations on decomposition reactions. The mainly reported decomposition pathway of liquid ionic cyanides is the *reverse* Menshutkin reaction, where *e.g.* the dicyanamide is alkylated under formation of volatile N - alkylimidazole.<sup>[118, 119, 191]</sup>

The maximally coordinated and therefore non - nucleophilic and very stable TCB anion is not reactive in that sense. Ohtani *et al.* investigated thermal decomposition behaviours of other imidazolium - type ionic liquids.<sup>[192]</sup> According to their results there are generally two pathways. The first pathway is the dealkylation of N,N' - dialkylimidazolium is *via* Hofmann elimination to form volatile alkenes and N - alkylimidazole *i.e.* ethane and N - methylimidazole in the case of Emim. Within the second pathway, nucleophilic anions undergo *reverse* Menshutkin reaction like described for other cyano - containing ILs. Interestingly, in all described cases the imidazole ring structure is retained at 550 °C, showing its remarkable stability. Methylated rings are more common decomposition products than ethylated ones. However, the preferred course is dependent on the anions nature. In case of non - nucleophilic anions, such as fully coordinated complexes *i.e.* PF<sub>6</sub><sup>-</sup> and BF<sub>4</sub><sup>-</sup>, the anion needs to decompose into reactive derivatives to initiate one of the pathways. Unfortunately the fact, that the anion needs to act as proton abstracting base to induce Hofmann elimination is poorly discussed. Therefore, ionic liquids with less nucleophilic, but rather Brønstedt basic anions preferentially decompose *via* pathway one, while rather nucleophilic anion lead to the *reverse* Menshutkin reaction.

Obviously, a known decomposition behaviour, nucleophilicity and brønstedt basicity of the TCB anion is important to know to predict the decomposition behaviour Emim - TCB. The TCB anion, which was first described in year 2000 shows up with an exceptional stability, presumably coming from the only weak electrophilicity of the cyano - C atom.<sup>[193, 194]</sup> Küppers *et al.* reported on tetracyanoboric acids finding H[B(CN)<sub>4</sub>] to be a strong acid, implying weak basicity of the anion due to acid - base theory. The colourless powder decomposes under release of HCN to a brownish polymeric compound of the stoichiometry [B(CN)<sub>3</sub>]<sub>n</sub>. The very stable, non - nucleophilic nature of the TCB anion and the weak basicity, can explain the onset of decomposition at comparably high temperatures, not preferring one or the other pathway. In the presence of protons, TCB can decompose into HCN and a polymeric cyanoborate species, while at higher temperatures the autodissociation / pyrolysis of the complex can be expected. Based on the former described information we can propose a decomposition scheme for Emim - TCB (Figure B16). As the TCB anion is neither nucleophilic nor basic, a non -

classic decomposition pathway is expected. Like in the case of other fully coordinated complexes the anion pyrolysis should initiate the decomposition. However, the high stability of the TCB anion can cause serious changes, transferring the reaction to a regime of bond pyrolysis, where even imidazole decomposition may occur.

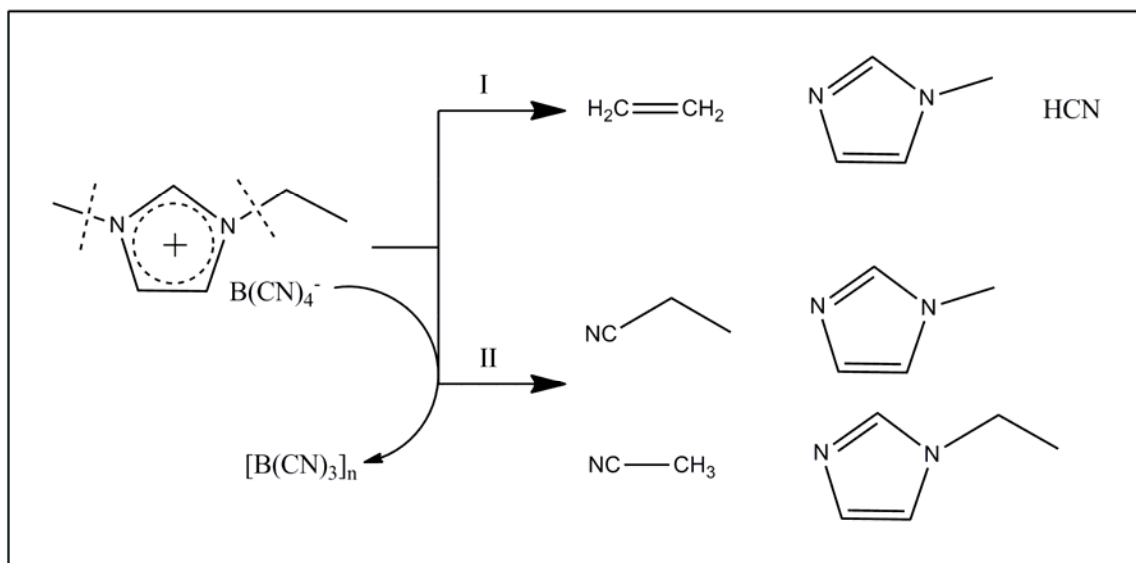


**Figure B16:** Proposed decomposition scheme for Emim - TCB. Adapted from Othani *et al.*<sup>[192]</sup>

As related research is currently focussed on ionic liquids as solvents<sup>[195, 196]</sup> rather than material precursors, it is not much known about decomposition and rearrangement reactions and the whole solid formation. For cyano - containing ILs cycloaddition is expected to be crucial before rearrangements and functional group release leads to further carbonisation. However, in the high temperature range (600 - 1000 °C), bond pyrolysis takes place and directs further decomposition and condensation / rearrangement steps. To get an idea of the driving forces in that context, Table 4 lists present (**bold**) and potential bonds (*italic*) ordered by their standard building enthalpies.

**Table 4:** Binding energies of a selection of appearing and potential bond within the decomposition of Emim - TCB<sup>[197]</sup>

<b>Bond</b>	$\Delta H_b / \text{kJ mol}^{-1}$	<b>Bond</b>	$\Delta H_b / \text{kJ mol}^{-1}$
<b>C=C</b>	<b>266</b>	<b>B-C</b>	<b>352</b>
<b>C≡N</b>	<b>276</b>	<i>B-H</i>	<i>372</i>
<b>C-N</b>	<b>293</b>	<i>N-H</i>	<i>391</i>
<i>B-B</i>	<i>310</i>	<b>C-H</b>	<b>413</b>
<b>C=N</b>	<b>322</b>	<i>H-H</i>	<i>436</i>
<b>C-C</b>	<b>348</b>	<i>B-N</i>	<i>500</i>

Concerning solid formation it can be expected that aromatic addition (*e.g.* hydrocyanation) and pericyclic *i.e.* cycloaddition reactions may happen due to the relative weakness of double and triple bonds. In agreement with expected *reverse* Menschutkin reaction and Hofmann elimination the weakest single bond, which is the C - N bond, is expected to break first. Imidazole decomposition products thereby may be incorporated into the triazine network, explaining the cations influence on the final product composition, but not the vanishing yield by reaction of the same anions with other cations. Despite its remarkable stability, decomposition reactions of imidazoles at appropriate high temperatures (*i.e.* > 550 °C) should occur. Regarding the anion, cleavage of the relatively strong B - C bonds should lead to thermodynamically even stronger B - N bonds. It has to be mentioned that the very stable B - O bond (~ 540 kJ mol<sup>-1</sup>) - explaining the strong oxophilicity of boron - usually leads to BCN(O) materials at temperatures underneath 900 °C. Even attentive exclusion of oxygen during the synthesis still ends in the formation of metastable compounds, which oxidise after cooling in the presence of oxygen / water. Therefore, a reshuffling from B - C to B - N, but also to B - O bonds after synthesis must be considered.

To aid elucidation of the reaction mechanism, the pure precursor Emim - TCB was heated under nitrogen gas flow to different temperatures (heating rate: 10 K min<sup>-1</sup>, isothermal period at T<sub>max</sub> for 1 hour) and analysed towards the B, C, N and H elemental



composition of the product (Figure B17). The glassy solid product of the first decomposition / condensation steps, produced at 450 °C denoted as *Emim - TCB - 450* (B, 8.4; C, 36.2; N, 27.0; H, 3.6), shows a drastically reduced hydrogen, nitrogen and carbon content compared to *Emim - TCB* (B, 4.78; C, 53.13; N, 37.18; H, 4.9), whereas the relative boron content is clearly increased. This is in accordance with the expected decomposition mechanism as no volatile boron compound is released. With increasing temperatures of up to 1000 °C the loss of hydrogen and nitrogen follows this trend, whereas the carbon and boron content are increasing. The overall mass of the presented data (B, C, N and H) does not reach 100 %, most likely due to the former described post-synthesis oxidation. So far the products are therefore best described as BCN(O) materials. However, exceeding 1000 °C the description as BCN materials gets reasonable, obviously due to the release of oxygen, which could explain the step at this temperature in the diagram (Figure B17), caused by the increased relative amount of B, C and N. While the nitrogen content of nitrogen-doped carbon drastically decreases with increasing temperatures, the presence of boron keeps the nitrogen within the structure. At such high temperatures elemental analysis approaches a ratio of one between B and N. This well-known curiosity can be explained by the strong B - N bond, which also makes boron nitrides chemically and thermally extraordinary stable. The final material, prepared at 1400 °C has the composition of  $BC_{3.1}N_{0.96}$  (B, 16.5; C, 56.67; N, 20.44; H, 0.83).

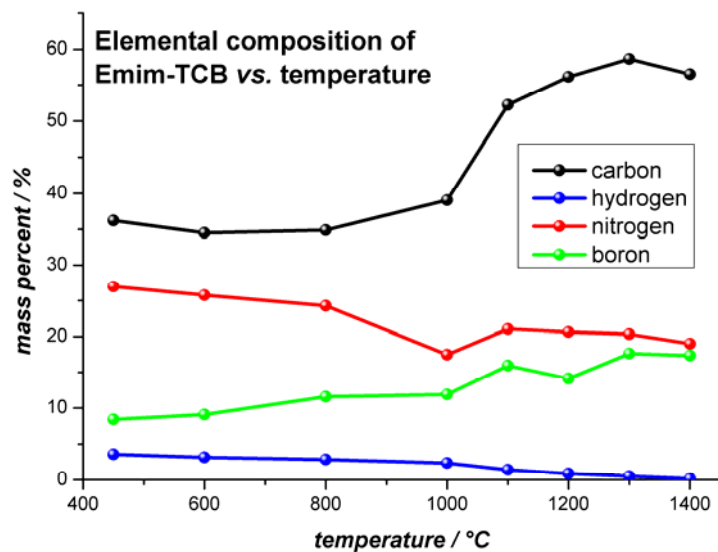
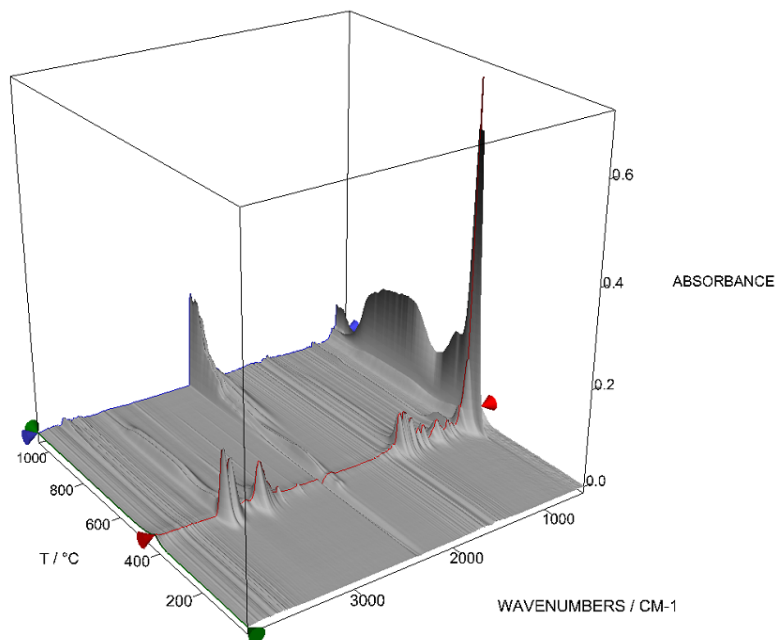


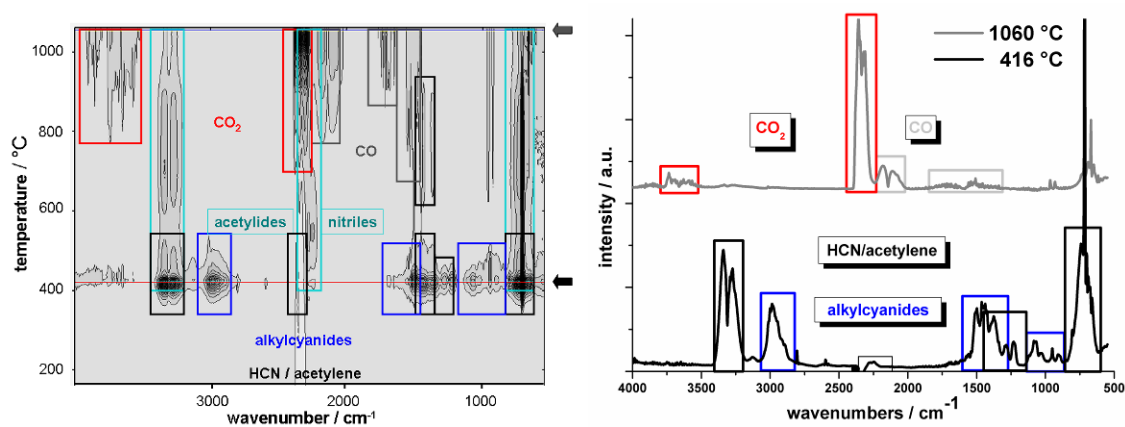
**Figure B17:** Elemental composition (BCHN) of the pyrolysis products of Emim - TCB at increasing preparation temperatures.

A coupled measurement for thermogravimetric analysis and infrared spectroscopy (TG - IR) has been employed to investigate the outgoing volatile decomposition products (Figure B18). The achieved results will be discussed regarding the proposed decomposition pathway, which can give important hints on the actual formation of solid. In accordance with the discussion of the TGA, where a strong mass loss appeared at 416 °C intensive infrared signals can be detected in the range of this temperature. Pronounced peaks at this point are mainly found in the fingerprint region and in between 2800  $\text{cm}^{-1}$  and 3400  $\text{cm}^{-1}$ . With increasing temperature almost continuous signals of lower intensity in the region of 2000 - 2500  $\text{cm}^{-1}$  and 600 - 800  $\text{cm}^{-1}$  are obtained. Reaching high temperatures above 900 °C signals at 2000 - 2500  $\text{cm}^{-1}$  are strongly increased. Over the whole temperature range an impurity  $\text{CO}_2$  band (2300 - 2400  $\text{cm}^{-1}$ ) with negative intensity has to be taken into account. Most likely, this originates from a baseline achieved with impurities in the nitrogen gas flow.



**FigureB18:** 3D plot of TG - IR measurement of headgas components of the decomposition of Emim - TCB between 20 and 1060 °C under nitrogen gas.

To summarise the following interpretation Figure B20/left illustrates the described results in a two dimensional contour plot. Observed signals herein are already assigned to decomposition products. In Figure B19/right single spectra at representative temperatures of 416 °C and 1060 °C are presented.



**Figures B19:** 2D contour plot of TG - IR spectra of the decomposition headgas of Emim - TCB (left). Selected IR - spectra, characteristic for main volatile decomposition products of Emim - TCB.

Interestingly, some of the expected decomposition products are not obtained in the experimental results. Only characteristic peak sets of HCN (black), indicating pathway I, and acetonitrile / propionitrile depicted as alkylnitriles (blue), indicating pathway II, are observed in context with the strong decomposition step at 416 °C. Most likely, Hofman elimination and *reversible* Menschutkin reaction both are involved in the decomposition of Emim - TCB. However, corresponding imidazole signals are not observed, indicating the compounds remaining in the condensed phase.<sup>v</sup> Astonishing is the occurrence of acetylene signals (also black, but characteristic at  $\sim 1250 \text{ cm}^{-1}$ ) at these temperatures, while ethane is not detected at all! Harsh conditions and metal catalysts are usually applied for oxidative dehydrogenation of alkanes for the  $\text{CO}_x$ -free generation of hydrogen, which is highly desired for the implementation of fuel cell technology.<sup>[198]</sup>

With increasing temperature at a much lower level characteristic signals of acetylides and cyanides are observed. Unfortunately, the negative peaks of the baseline ( $\sim 2350 \text{ cm}^{-1}$ ) disturb the assignment of the weak signal in such a way, that the release of HCN remains unclear. The appearing, slightly red - shifted C - N stretch signals, are still characteristic for cyanides, but remain unassigned to literature known compounds. In contrast to other N,N' - dialkyimidazolium ionic liquids no, or at least much less N - alkylimidazole is evaporated, while the appearance of alkylcyanates hints on imidazole decomposition. However, aromatic addition reactions could produce volatile cyanides as well. Hence, these species strongly contribute to the formation of residual mass. Most likely, the improved stability of the TCB anion, compared to other common anions, delays the process of decomposition to temperatures, where even the very stable imidazole structure undergoes cross - linking forming non - evaporating solid. On the one hand this may explain why Lee *et al.* achieved solid mass from the pyrolysis of ionic liquids without cyano - containing anions, contradicting the decomposition model of Paraknowitsch.<sup>[199]</sup> On the other hand it also clearly shows that the reaction scheme of Lee *et al.* is by far too simple, as they most likely form polyimidazole - type of networks instead of triazine networks, which are then further carbonised.<sup>[142, 190]</sup>

---

<sup>v</sup> A *retro* - Diels – Alder decomposition can be imagined as well, however as the respective signals are below 550 °C this would contradict the results of Ohtani *et al.*<sup>[192]</sup>

As a fact of the measurement we also have to consider missing IR - inactive species or signals. For instance molecular hydrogen, which is most likely generated together with acetylene, but also molecular nitrogen (often released at high temperatures) are not detectable with this method. The results of the lower temperature range lead to a first decomposition scheme (Figure B20). Undetected products are shown in grey.

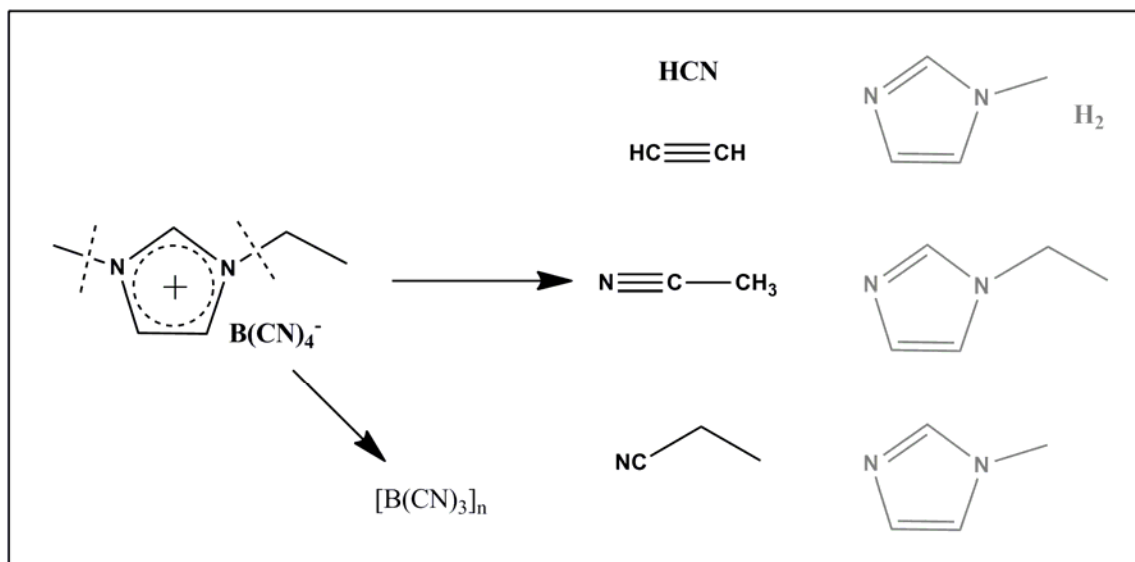


**Figure B20:** Decomposition scheme for the “low” temperature (< 600 °C) evolution of volatiles at the pyrolysis of Emim - TCB.

Between 800 and 1000 °C elemental analysis is showing a step, which was expected to be due to oxygen release. Exactly at these temperatures (above ~ 800 °C) the release of carbon monoxide and carbon dioxide can be detected. The intensity even increases with temperature. Obviously, the highly oxophilic boron within Emim - TCB was reacting with oxygen/water impurities of the IL or the carrier gas within the TG - IR measurement. The release of CO and CO<sub>2</sub> is in perfect accordance with the observations from elemental analysis, explaining the formation of BCN materials only at high temperatures. From former TG - MS studies it can be expected that molecular hydrogen and nitrogen are released within this typical process of carbonisation / rearrangement as well.<sup>[118]</sup>

To get further insight into the mechanistic course we applied FT - IR spectroscopy on products synthesised at 450, 600, 800 and 1000 °C (Figure B21). The spectrum of *Emim - TCB - 450* (grey) clearly shows the appearance of a strong and broad developed shoulder at 2000 - 3750  $\text{cm}^{-1}$ . The characteristic imidazole signals in the fingerprint region are retained, showing that imidazoles indeed remain within the solid, contributing to the materials formation. Interestingly this is not correlated to ring - opening decomposition and subsequent polymerisation. At the same time the mentioned signals appear strongly broadened. The shoulder might be due to N - H vibrations and therefore events like the protonation of N - alkylimidazoles or the formation of tertiary amines. Additionally, oxidised boron, especially at edge sites of the material, may contribute to the signal *via* B - O - H groups. The broadened fingerprint region indicates condensation towards a  $\pi$  - conjugated polyimidazole - type of network. In fact obvious similarities to the vibrational spectrum of poly - biimidazole - 5,5' - diyl can be observed.<sup>[200]</sup>

The second and as reported most important material generating reaction is the cycloaddition of the cyanides *i.e.* the triazine building reaction. The characteristic C - N stretch signal (2200 - 2260  $\text{cm}^{-1}$ ) can still be detected in *Emim - TCB - 450* (grey) and *Emim - TCB - 600* (blue) indicating the presence of non - reacted cyano - functions. However, the ongoing cycloaddition can be concluded by the successive disappearance of this characteristic peak. In accordance with the conclusions from TG - IR measurements, polymeric imidazoles are formed and aromatic addition reactions, like hydrocyanation, most likely provoke an intermixed network. The intensity of the N - H / O - H band and the characteristic fingerprint successively decrease with increasing temperatures, indicating the carbonisation of the whole material. This is in accordance with the steady reduction of the amount of hydrogen and nitrogen in elemental analysis, whereas the carbon content is slightly increased. For *Emim - TCB - 800* (red) no functional groups, namely the broad N - H / O - H vibrations (2000 - 3750  $\text{cm}^{-1}$ ) and cyanide signals (2200 - 2260  $\text{cm}^{-1}$ ) can be detected anymore. This is the typical situation for carbonised material.

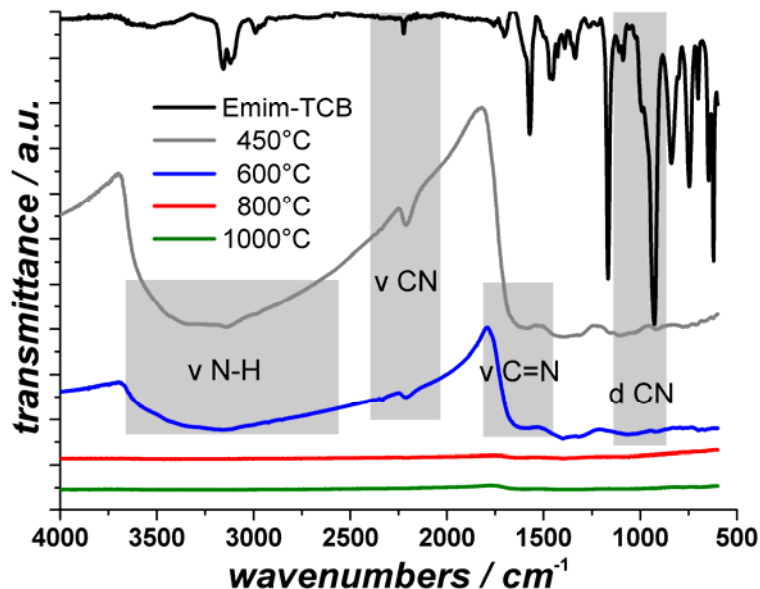


**Figure B21:** FT - IR spectra of the solid product from pyrolysis of Emim - TCB at different temperatures.

Additional information about the formation of insoluble solid can be gained using  $^{13}\text{C}$  solid - state NMR by comparison of the pure liquid spectrum of Emim - TCB with the solid spectra of *Emim - TCB - 450*, *-600* and *-800* (Figure B22). The spectra can be divided into aliphatic signals with low chemical shifts ( $< 50$  ppm), which belong only to Emim and aromatic / cyanide signals with high chemical shifts ( $> 110$  ppm). A strong decay of intensity of the aliphatic signals is observed for *Emim - TCB - 450* (grey), while signals in the aromatic / cyanide region get relative importance. In accordance with the former discussion this can be explained by aliphatic rests forming volatiles within the decomposition process, while the TCB anions and the imidazoles both contribute to the formation of solid. The characteristic peaks for imidazoles are found at  $\sim 125$  ppm and  $\sim 147$  ppm. At  $450^\circ\text{C}$  these signals are clearly broadened, showing the generation of extended polymeric solid *i.e.* polyimidazole - type networks. Due to the nuclear Overhauser effect the carbon peak of TCB is comparably weak, as there is no proximal hydrogen. However, the emerging triazine peak at  $\sim 160$  ppm can be observed in *Emim - TCB - 600* (blue). As already present at  $450^\circ\text{C}$  the formation of polyimidazole obviously initiates the solidification process, while cycloaddition reactions of the anions, appearing at  $600^\circ\text{C}$ , are starting later. Together both reactions lead to an intermixed polymeric network, which can be carbonised in the following. Another emerging peak at  $\sim 120$  ppm

can be observed in the spectrum of *Emim* - *TCB* - 600. As this region is characteristic for alkenes and cyanides, it can be expected, that incorporated imidazole decomposition products cause the signal. Generally, an accentuated broadening, due to condensation, and decrease of intensity, due to the loss of hydrogen, can be observed with increased temperature, as a result of carbonisation.

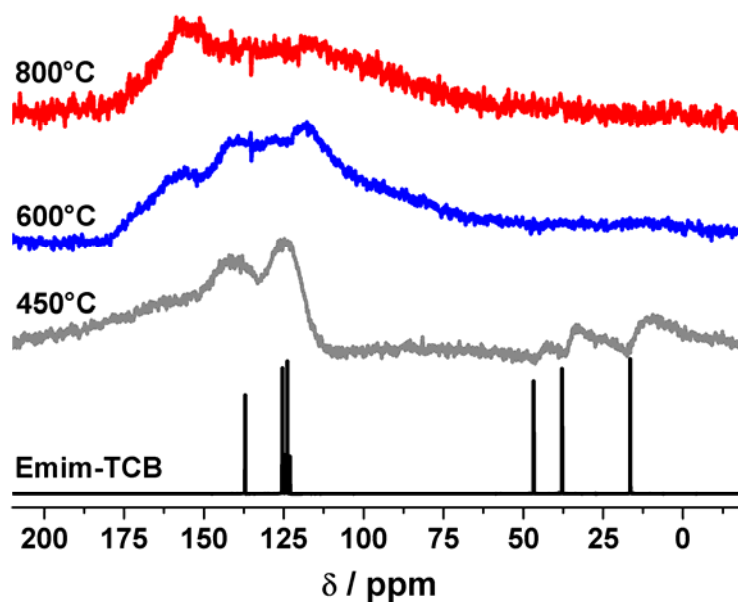


**Figure B22:** Comparison of the liquid  $^{13}\text{C}$  - NMR spectrum of *Emim* - *TCB* with solid - state NMR spectra of solid pyrolysis products at different temperatures.

Summarised it can be stated, that the stability of *Emim* - *TCB* leads to a late decomposition of the ionic liquid, as Hofman elimination and *reverse* Menshutkin reaction cannot take place directly. The decomposition is initiated by degradation of the *TCB* anion at very high temperatures *i.e.*  $\sim 420$  °C. While almost only alkylcyanides, acetylene and HCN can be detected as outgoing volatiles, two main reactions lead to the formation of solid. First the formation of polyimidazole - type networks, which most probably can only develop at such elevated decomposition temperatures, and second the already reported cycloaddition of cyanides to triazine - based networks. Clearly, aromatic substitution or addition reactions, in context with decomposition of imidazoles, may cause cross - linked, intermixed networks. With increasing temperatures bond pyrolysis



conditions are approached. The accompanied loss of functional groups leads to further condensation / carbonisation and successive formation of BCN material.

Carbon (C) and the isoelectric boron nitride (BN), both show structurally equivalent allotropes plus an amorphous and a turbostratic phase. Nitrogen - doped carbon from ionic liquid precursors exhibit  $sp^2$  - hybridised graphite - like carbon. Considering the planar cyano - containing anions dicyanamide and the likewise condensed triazine network this could be expected. In the case of tetrahedral coordinated TCB anions, thus  $sp^3$  - hybridised boron, the situation is different. To get an idea of the actual morphology of the produced BCN material, Raman spectroscopy, electron energy loss spectroscopy (EELS) and wide angle X - ray scattering (WAXS) were applied. The Raman spectrum of *Emim - TCB - 1400* received from irradiation with a green laser (532 nm) clearly indicates graphite - like material (Figure B23). The *G* - band appears at  $1605\text{ cm}^{-1}$ , while the *D* - band, which is also the  $E_{2g}$  band for unsymmetrical systems such as *h* - BN, shows up at  $1343\text{ cm}^{-1}$ . The *D* - band is even broader than the *G* - band, obviously caused by the contribution of both, the asymmetric B - N bonds and defect sites. Likewise, the *D* - band intensity clearly exceeds the intensity of the *G* - band, discriminating *Emim - TCB - 1400* from typical disordered carbon materials. At higher wavenumbers second - order scattering shows the respective overtone bands *D\** and *G\** as well as combination oscillations. The *D* - band is red shifted by  $27\text{ cm}^{-1}$ , whereas the *G* - band is blue shifted by  $32\text{ cm}^{-1}$ . The energetic positions of the signals are determined by the bond strength. C - C bonds are weaker than B - N bond and shift the *h* - BN - type *D* - band to lower energies. The opposite influence is given by B - N bonds to the graphite - type *G* - band. Both shifts together indicate the interaction of B, C and N bonds and therefore the homogeneous character of the materials, which consequently can be denoted as graphitic boron carbon nitride (*g* - BCN).

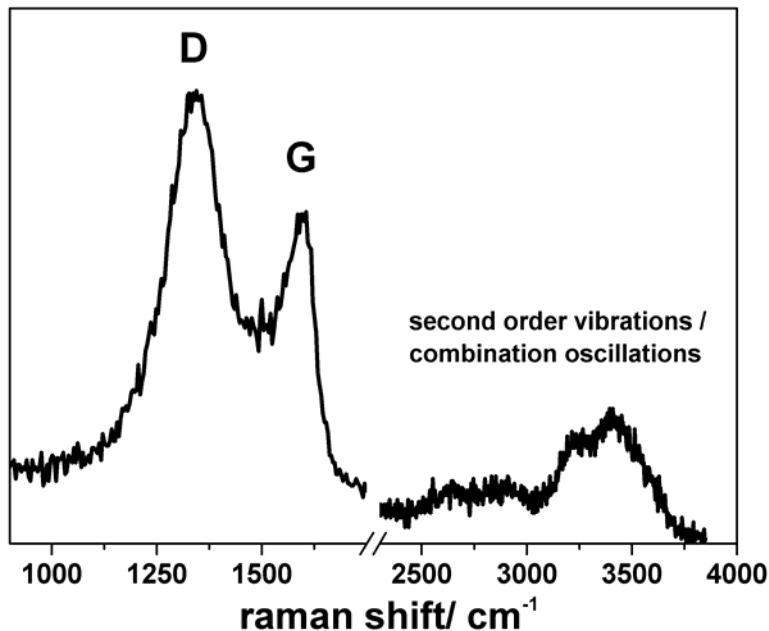


**Figure B23:** Raman spectrum of Emim - TCB - 1400 measured with green laser ( $\lambda = 532$  nm).

The EELS mode in a TEM can perform structural and chemical composition studies at the nanometre scale. Respective measurements of the core loss region give access to the chemical and electronic structure. Therefore measurements of *Emim - TCB - 1400* were carried out to give evidence to the hybridisation of atoms and the homogeneity of the material. As an indication on the homogeneity of the sample the chemical composition measured by the spatially high resolved (0.1 - 1 nm) EELS is in agreement with the bulk composition of *Emim - TCB - 1400*. The results, reflecting the electronic environment of each atom (Figure B24) indeed support the concepts of graphitic incorporation of all three elements, with very sharp  $\pi^*$  - transitions, typically for delocalised  $\pi$  - electron pools, as can be seen from the well - defined structure caused by long - range  $sp^2$  - hybridisation.

This especially has to be underlined for the B - atoms, which seems to be conjugated to larger extents.

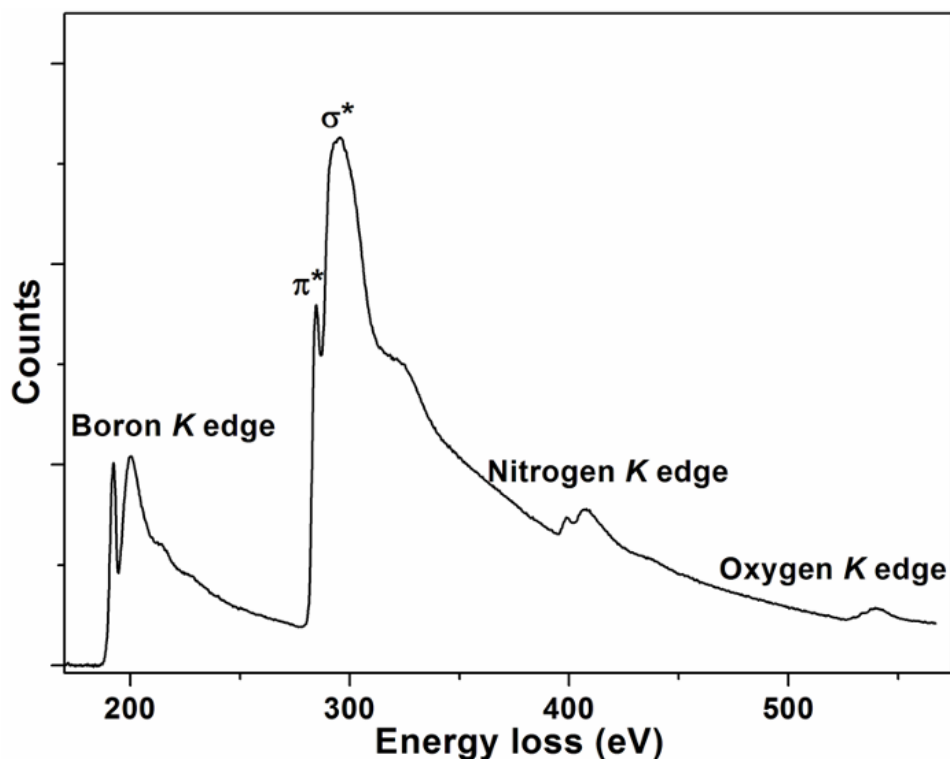


**Figure B24:** EELS spectrum of core loss region of boron, carbon, and nitrogen within Emim - TCB - 1400.

WAXS measurements additionally give evidence to the graphite - like structure (Figure B25/left). The ongoing condensation of the polymeric BCN system at higher temperatures towards graphitic material can be nicely followed by the corresponding WAXS patterns in dependence of the condensation temperature. With increasing temperature (from 600 °C to 1300 °C) typically broadened (002) and (100) peaks, characteristic for inter- and intraplane distances in graphitic materials develop. In contrast to nitrogen - doped graphitic carbons the development of graphitic ordering, appearing as a strong increase and sharpening of the mentioned (002) and (100) peaks, are only observed above 1000 °C. The loss of oxygen starting at such high temperatures according to TG – IR / elemental analysis results can be expected to be the reason for this curiosity. Bound into the structure, it might hinder the formation of graphite - like morphology, most likely due to  $sp^3$  - hybridised oxygen and the respective tetragonal binding motif.

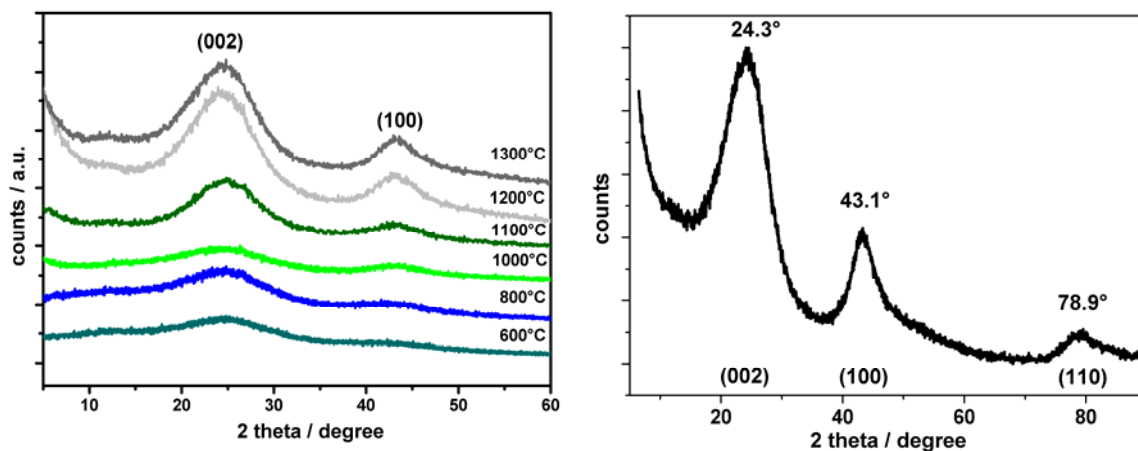


**Figure B25:** WAXS - patterns of pyrolysed Emim - TCB in dependence of carbonisation temperature (left) and of Emim - TCB - 1400 (right).

The typical patterns for non - crystalline graphitic carbons are well - defined at 1400 °C (Figure B25/right). Comparable with IL - derived nitrogen - doped carbon materials broadened (002)- at  $2\theta = 24.3^\circ$  ( $d = 3.64 \text{ \AA}$ ), (100) - peaks at  $2\theta = 43.20^\circ$  ( $d = 2.05 \text{ \AA}$ ) and (110) - peaks at  $2\theta = 78.9^\circ$  ( $d = 1.21 \text{ \AA}$ ) are obtained. The presence of the (110) peak indicates the high conjugation within the material. A certain broadening and peak shifting can be explained by the presence of unequal bonds, such as C - C and C - N bonds for the nitrogen - doped carbon, plus B - N and B - C bonds in the case of  $B_xC_yN_x$  materials. However, broadening is also attributed to a low degree of crystalline order. Notably, the (002) peak is shifted towards smaller angles, indicating a larger interlayer distance of  $3.64 \text{ \AA}$  compared to  $3.33 \text{ \AA}$  for *h* - BN and  $3.35 \text{ \AA}$  for graphite.<sup>[201]</sup> Like in the case of nanotubes, which also show increased interlayer spacing - depending on their diameter - this can be interpreted as measure for the curvature.<sup>[202]</sup> Together the features of the diffractograms remind on the results for nitrogen - doped carbons underlining the structural similarities towards the IL - based boron carbon nitride and with no indication on mixed phases.

X - ray photoelectron spectroscopy (XPS) experiments were applied to further investigate the “step” phenomenon at around 1000 °C and to achieve more detailed insight into the chemical bonding within the interesting material (Figure B26).

Even more detailed information about the chemical composition and the certain binding motifs *i.e.* the actual connectivity within *Emim - TCB - 1400* can be achieved applying

XPS. The measurements revealed a chemical composition of the boron carbon nitride of  $B_{1.42}C_{3.1}N$ . As XPS is a surface - sensitive technique the comparison with the elemental analysis results ( $BC_{3.1}N_{0.96}$ ) indicating increased boron content close to the surface. Additionally, 6.4 % of oxygen and small silicon impurities (0.4 %) are detected. Importantly, like the metal - free synthesis procedure promises, no other metal impurities such as iron are found.

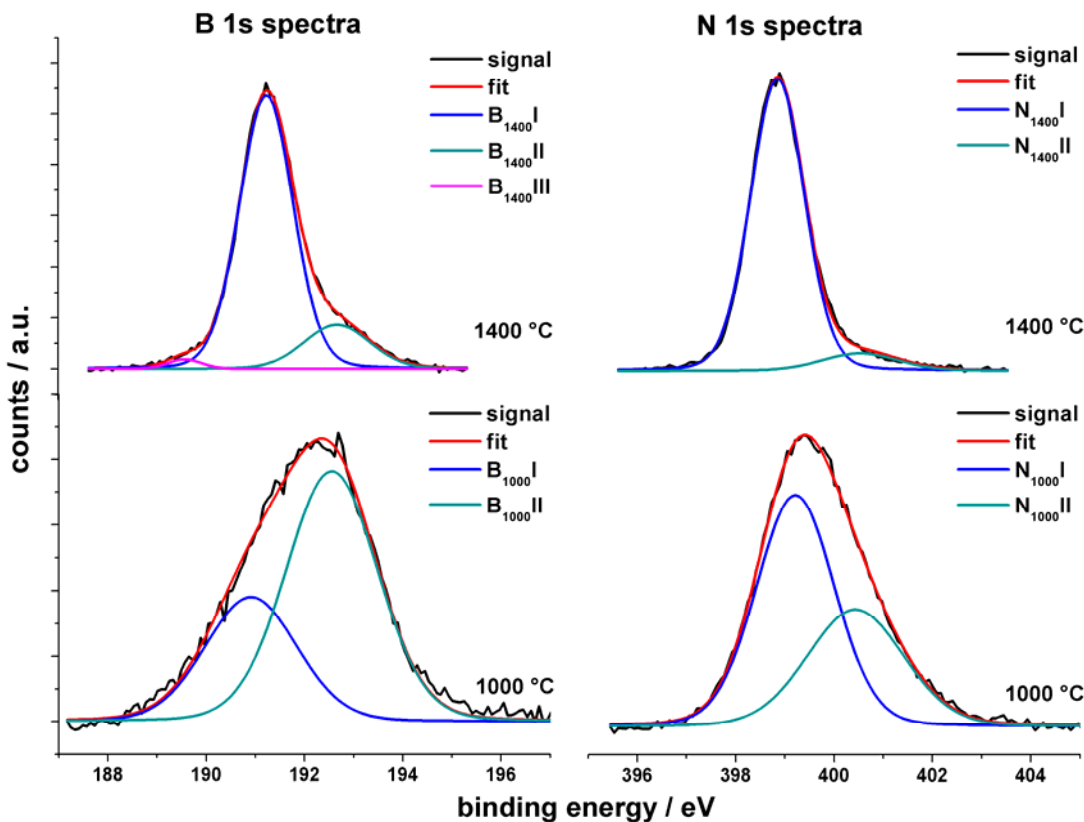


**Figure B26:** High resolution XPS spectra (B 1s and N 1s) of *Emim - TCB - 1000* and *Emim - TCB - 1400*.

With increasing synthesis temperature the XPS signals are clearly shifted to lower binding energies, due to decreased peak intensities at higher binding energy and increased peak intensities at low binding energies. This indicates more pronounced bonding to electropositive elements.

The B 1s spectra mainly show two peaks. While BI ( $B_{1000}I@191.1$  eV;  $B_{1400}I@191.0$  eV) is strongly increased at 1400 °C, becoming the dominant peak, BII ( $B_{1000}II@192.6$  eV;  $B_{1400}II@192.7$  eV) rapidly decreases in intensity with increasing

temperature. In accordance with the expected positions due to the lower electronegativity of boron compared to oxygen BI can be assigned to the BCN binding motive, while BII is assigned to oxygenated boron (B - O). A third, but comparably weak peak at 189.8 eV (B<sub>1400</sub>III) is observed for *Emim - TCB - 1400*, due to the electropositive carbon assigned to a B - C binding motif.

The N 1s spectra are composed of two peaks. NI is dominating, but at higher temperatures even more intensive. Again in agreement with the comparably electropositive boron the peak can be denoted as characteristic BCN peak at 398.8 eV (N<sub>1000</sub>I /N<sub>1400</sub>I). A low fraction of (pyrrolic - type) nitrogen bound to carbon can explain peak NII (N<sub>1000</sub>II@400.4; eV N<sub>1400</sub>II@400.5 eV).

Together the XPS data clearly support the assumption that the release of oxygen - containing volatiles (*i.e.* CO<sub>2</sub> and CO as known from TG - IR) allows the arrangement of a boron carbon nitride in a graphitic form, which could be observed *via* Raman and WAXS measurements. Also, it can be stated that XPS nicely supports the structural incorporation of both B and N into the graphitic structure. Contrary to the precursor, where boron is solely bound to carbon, most boron atoms in the final material referred to the XPS measurements are however bound to nitrogen, *i.e.* the local bonds are reshuffled. After high temperature treatment the remaining nitrogen is predominantly bound to boron. This underlines the isoelectric concept *i.e.* the stability of BN moieties integrated into graphitic carbon compared to the respective single dopants. The higher abundance of boron *versus* nitrogen at the surface (measured with XPS) compared to the bulk (measured with elemental analysis) can therefore be explained by the presence of oxygen, *i.e.* surface oxidised boron carbon nitride. The oxygenation disrupts the B - N bonding. Oxygen - terminated boron is stable up to temperatures above 1000 °C, whereas nitrogen not bound to boron is readily released, causing a decreased N / B ratio at the surface. The appearance of the B<sub>1400</sub>III peak at 1400 °C indicates the conversion of B - O bonds at least partly into B - C instead of B - N bonds at even higher temperatures.

The structural characteristics are finally investigated by HRTEM. A comparison of the highly resolved structure for the products derived at temperatures of 800, 1000, 1200 and

1400 °C is provided (Figure B27). *Emim - TCB - 800* and *Emim - TCB - 1000* can hardly be distinguished from amorphous carbon (see Appendix).

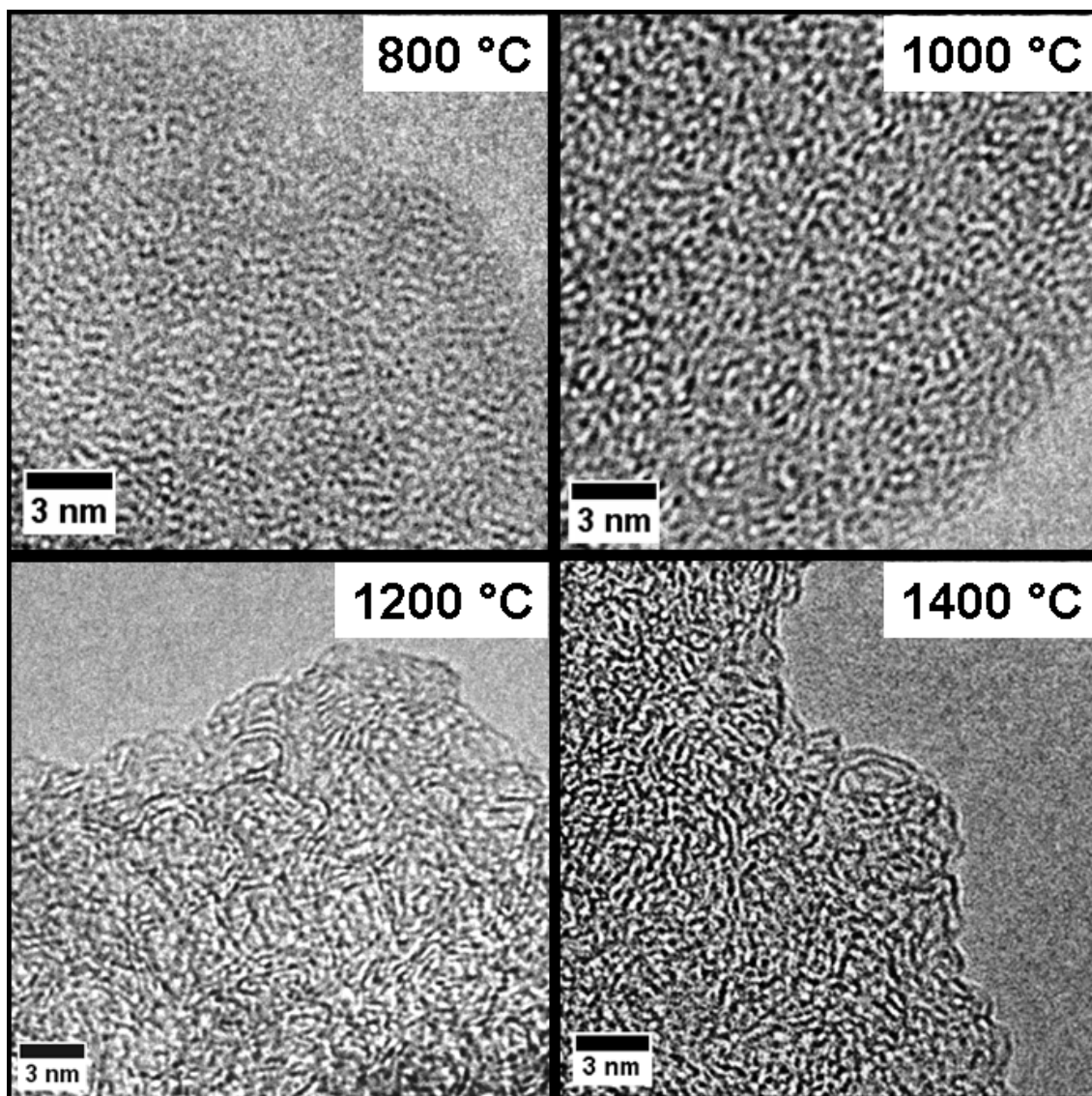


**Figure B27:** HRTEM images of the solid products of the carbonisation of *Emim - TCB* synthesised at 800, 1000, 1200 and 1400 °C.

The successive development of interesting features is indicated by the image of *Emim - TCB - 1200*. Different curved morphologies most likely being bent graphitic layers are observed. Further heat treatment increases condensation, which leads to the cauliflower - like appearance. However, the curvature remains the same meaning that no alignment is observed. Apparently, a condensed bulk material made of intermingled nanosheets is formed. The lack of long - range order is in perfect agreement with the

presented WAXS data, while the curvature, which is comparable to carbon nanotubes or -onions explains the increased interlayer distance leading to the negatively shifted (002) peak. The high defect density, from the viewpoint of crystalline nanomaterials, can indeed explain the additional intensity and broadening of the Raman - *D* - band. In accordance with the increasing (100) intensity the length of the layered worm - like domains increases with temperature. In conclusion the structures are very similar, but even more bent than nitrogen - doped carbons from ILs.

IL - based nitrogen - doped carbon materials, even if rather non - crystalline, have been reported to exhibit advanced electric conductivity compared to graphite powder.<sup>[101-107, 203]</sup> Crystalline, graphitic  $B_xC_yN_z$  materials were reported to have a basal - plane resistivity of  $7.81 \cdot 10^{-3} \Omega \text{ m}$  (BCN(H)) and  $0.11 \cdot 10^{-3} \Omega \text{ m}$  ( $BC_3N(H)$ ) at room temperature,<sup>[130]</sup> which is very low for semiconductors, but not compared to graphite ( $\rho$  (silicon):  $6.4 \cdot 10^2 \Omega \text{ m}$  @  $20 \text{ }^\circ\text{C}$ ;  $\rho$  (graphite, basal plane):  $2.5 - 5 \cdot 10^{-6} \Omega \text{ m}$  @  $20 \text{ }^\circ\text{C}$ ).<sup>[201, 204]</sup> However, as *h* - BN, being a structural part of the BCN material, is known to be insulating, this value is considerably high. To find out more about the relation of structure and properties of the nanostructure - like curved IL - based materials powders of the *Emim - TCB - 1400* and nitrogen - doped carbon, prepared like previously reported from BMP - dca @  $1000^\circ\text{C}$ , where spark - plasma sintered to homogeneous monolithic pellets (Figure B28, inset) and then characterised with respect to their electronic properties *i.e.* Seebeck coefficients and resistivity.

Evaluation of Seebeck coefficients  $\alpha$  (see Appendix) indicates the expected n - type character of the nitrogen - doped carbon ( $\alpha < 0$ ), while the B / N - doped carbon (*Emim - TCB - 1400*) turns out to be a p - type semiconductor ( $\alpha > 0$ ). This can be explained by the slightly exceeding boron content compared to the nitrogen content within the sample.<sup>[205]</sup> The low values of Seebeck coefficients ( $\alpha$  (nitrogen - doped carbon):  $-2 - (-10) \mu\text{VK}^{-1}$ ;  $\alpha$  (*Emim - TCB - 1400*):  $10 - 30 \mu\text{VK}^{-1}$ ) indicate a high concentration of charge carriers, one of the two main factors for electrical conductivity.

The electric resistivity in the temperature range from  $0 \text{ }^\circ\text{C} - 950 \text{ }^\circ\text{C}$  indicate the semiconducting behaviour of both products, showing the typical decreasing resistivity with increasing temperature (Figure B28). For semiconductors the electrical resistivities



of the materials are very low ( $\rho$  (amorphous carbon) =  $50 - 80 \cdot 10^{-3} \Omega \text{ m}$  @  $20 \text{ }^\circ\text{C}$ ).<sup>[204]</sup> *BMP - dca - 1000* has a resistivity of  $\sim 0.08 \cdot 10^{-3} \Omega \text{ m}$  @ room temperature, while *Emim - TCB - 1400* ( $\rho \sim 0.14 \cdot 10^{-3} \Omega \text{ m}$  @ room temperature) shows up with an electrical resistivity, which is only 1.75 times less than the nitrogen - doped carbon, therefore being in the range of crystalline BCN materials.<sup>[130, 205]</sup>

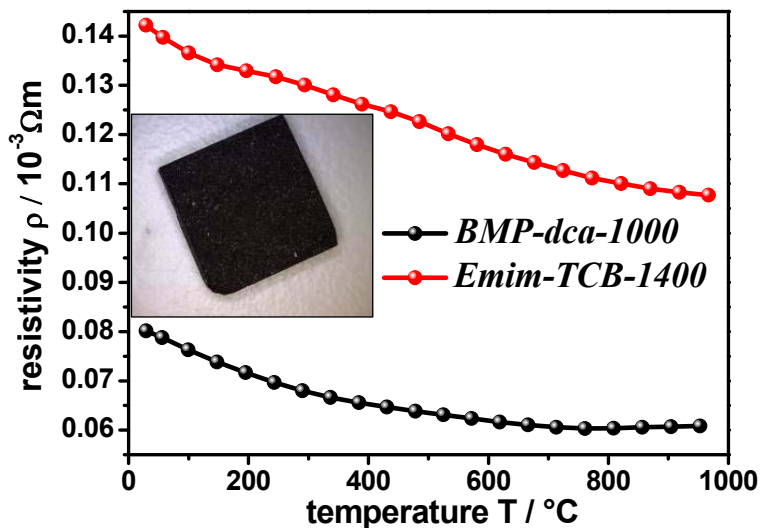


**Figure B28:** Electrical resistivity measurement of *Emim - TCB - 1400* and *BMP - dca - 1000* between 25 and 950 °C using standard 4 point probe setup.

These data indeed make present materials highly promising for various potential applications. Chemical functionalities at the surface, such as the BCN binding motif, might induce interesting reactivity due to acidic and basic characters. At the same time a high electrical conductivity tailors the materials especially for the field of electrochemistry and electrocatalysis. For the introduction of certain surface area, a precaution for the application in heterogeneous catalysis, again the common silica hard templating approach was employed. Although there are reports on mesoporous BCN materials using silica templates in combination with CVD methods<sup>[139]</sup> no boron carbon nitride replicas were achieved using *Emim - TCB* as precursor in standard recipes. More successful results were achieved by the “salt templating” approach, which was described above (see section B; basics and state-of-the-art) on the example of *LiCl / KCl* with the *dca* - based ILs. Concurrently to this thesis in our group Nina Fechner was successfully

employing caesium salts as salt templates to the synthesis of highly microporous ionic liquid based hybrid materials. Referring to her results caesium acetate (30 wt. %) was used and found to be a suitable salt templating additive within the boron carbon nitride synthesis at 1400 °C. Starting from a solution / mixed salt melt the acetate nanoseparates from the ionic liquid - based polymerisation product within the condensation reaction at high temperatures. After high temperature treatment caesium oxide is expected to form and mostly evaporate. Residual salt is removed by washing with water. TEM imaging and nitrogen sorption of the resulting product indicate the generation of microporosity (Figure B29). A type I nitrogen sorption isotherm, characteristic for microporous materials is observed. A specific surface area of  $\sim 817 \text{ m}^2 \text{ g}^{-1}$ , evaluated using BET - method, was achieved using 30 wt. % of inorganic salt at 1400 °C (heating rate  $10 \text{ K min}^{-1}$ , isothermal period @ 1400 °C for 1 hour). Mesoporosity, causing the small hysteresis in the nitrogen sorption isotherm is of minor importance as shown from porosity details derived from NLDFT model for slit shaped pores, revealing a microporosity of  $\sim 95 \%$ .

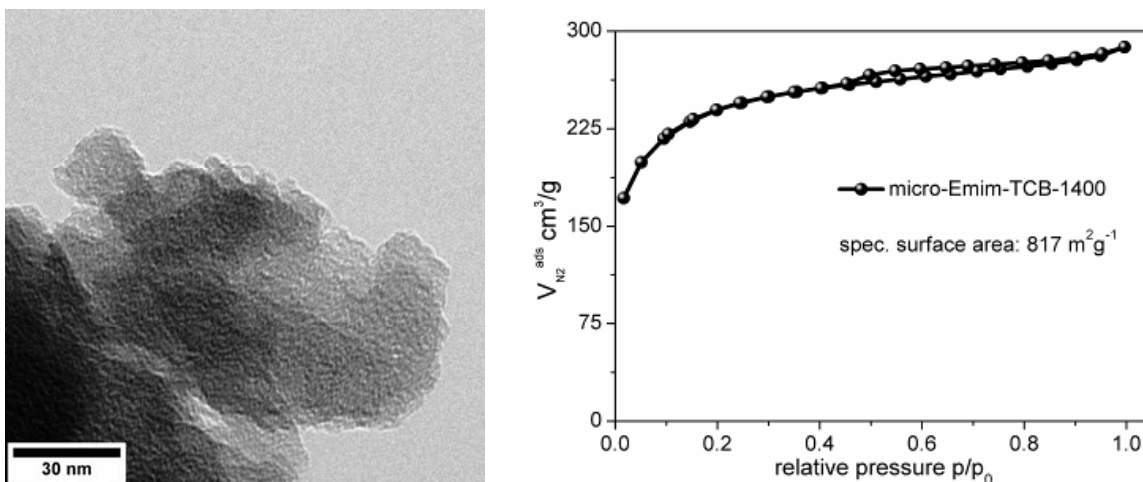


**Figure B29:** Nitrogen sorption isotherm (type I) of *micro-Emim-TCB-1400*.

In accordance with our observation of surface oxidation, like in the LiCl / KCl system, the high surface area boron carbon nitride prepared possesses decreased relative carbon and nitrogen contents going along with increased oxygen content. Therefore the material is better described as microporous BCN(O), in the following denoted as *micro-Emim-TCB-1400*. XPS analysis was applied to characterise the surface composition,

which is crucial for electrochemical application (Figure B30). While elemental analysis resulted in 50.0 % C and 14.6 % N, XPS revealed 57.4 % C, 12.3 % N and 13.9 % B. Referring to XPS the boron carbon (oxy)nitride exhibits a composition of  $B_{1.5}C_{5.4}N_1O_1$ . The difference in the elemental composition again can be explained by the surface sensitivity of XPS. The survey spectrum at the same time confirmed the iron - free character of the catalyst. However small traces of magnesium, silicon and caesium are detected, but can be expected not to contribute to the electrocatalytic activity (see Appendix).

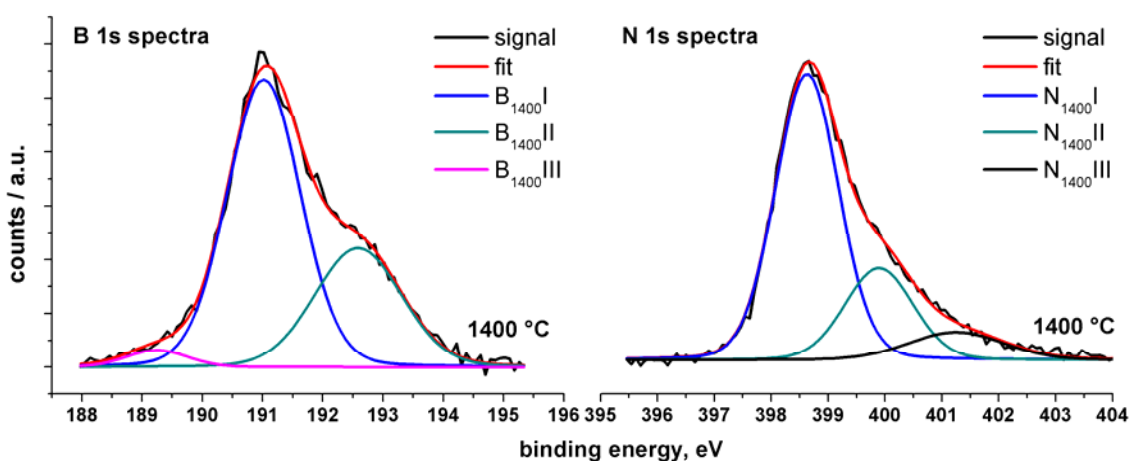


**Figure B30:** High resolution XPS spectra (B 1s and N 1s) of *micro-Emim-TCB-1400*.

The B 1s spectrum like in the case of *Emim-TCB-1400* shows three peaks. While the characteristic BCN peak intensity is decreased ( $B_{1400I}@191$ . eV) the signals for oxygenated boron ( $B_{1400II}@192$ . eV) and B - C moieties ( $B_{1400III}$ ) gain relative importance. Regarding the increased oxygen content for all presented high surface area materials this could be expected. However, even at the surface the main binding site after “salt templating” remains the characteristic BCN motif.

The N 1s spectra are composed of three peaks. In accordance with the B1s spectrum the characteristic BCN peak at 398.6 eV ( $N_{1400I}$ ) dominates, but with decreased relative importance compared to *Emim-TCB-1400*. The peak intensity of pyrrolic carbon bound nitrogen ( $N_{1400II}@399.9$  eV) is clearly increased and a signal at 401.3 eV ( $N_{1400III}$ ) appears in comparison with *Emim-TCB-1400*. This peak can be assigned to

quaternary carbon bound nitrogen. Together the XPS results reveal, that “salt templating” only changes the materials due to partial boron oxidation, obviously leading to a rearrangement of nitrogen, which interestingly can still be hold within the material. The as - prepared microporous boron carbon (oxy)nitride was employed for electrochemical testing.

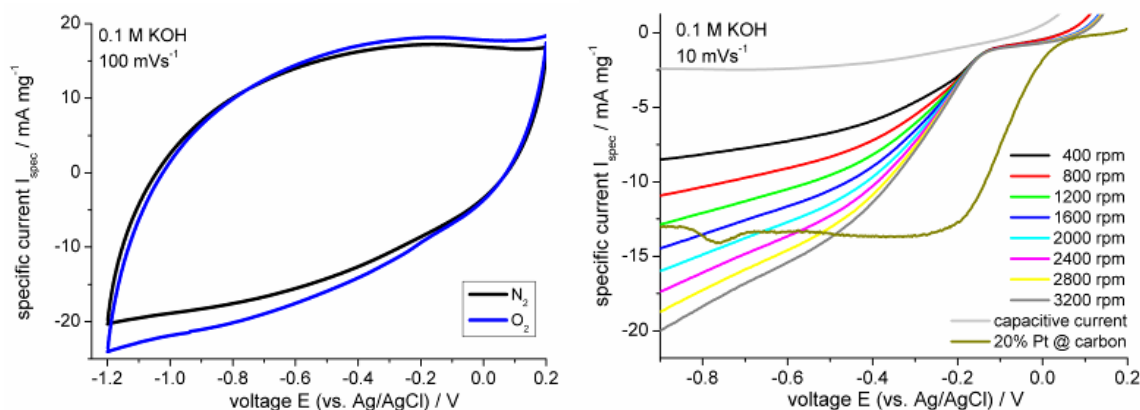


**Figure B31:** Electrochemical investigations on the ORR activity of *micro - Emim - TCB - 1400*. Cyclic voltammograms in deaerated and oxygen - saturated 1M KOH (left). RDE polarisation curves at different rotation rates compared to commercial 20 % Pt on carbon catalyst in 1M KOH (right).

The electrocatalytic activity of *micro - Emim - TCB - 1400* was first studied by cyclic voltammetry (Figure B31/left). Comparison of the CVs purged with nitrogen and oxygen gas, recorded at  $100 \text{ mV s}^{-1}$ , show the increased cathodic currents in the presence of oxygen. However, no well - defined reduction peak is observed. To further study the electrochemical properties LSV - RDE measurements were performed under oxygen saturation in a typical three electrode setup (Figure B31/right). The cathodic currents increase with increasing rotation speed *i.e.* oxygen diffusion. Therefore it is indeed not a capacitive effect, but the faradaic reduction of oxygen, catalysed by *micro - Emim - TCB - 1400*. For comparison the polarisation curve of commercial platinum catalyst (20 wt.% Pt on carbon) recorded at 1600 rpm was added. As can be seen the electrocatalytic ORR activity of the boron carbon (oxy)nitride at low potentials is even exceeding platinum. Still, the onset potential at around - 106 mV is strongly shifted to

lower potentials, indicating that the material is not as efficient as platinum or the former described nitrogen - doped carbons. Nonetheless, it is the first time a boron carbon nitride material is reported to catalyse the ORR.

Kinetic study of the reduction process using Koutecky - Levich Plots (Figure B32) reveals a similar slope to an ideal two electron process. Calculation employing the Koutecky - Levich equation gives an electron transfer number of  $n = 2.12$ , indicating that oxygen is not directly converted into water but intermediate hydrogen peroxide. Referring to the XPS results of *micro - Emim - TCB - 1400* one could doubt the ORR activity of boron carbon nitride itself, but rather assign the activity to pyrrolic and / or quaternary nitrogen. However, especially regarding a recent report on ORR active boron - doped carbon nanotubes<sup>[114]</sup> an active role of the BCN motif has to be considered as well. As supporting fact *micro - Emim - TCB - 1400*, in contrast to the other IL - derived catalysts, showed very low activity in the acidic medium. As observed on a novel material these results are highly interesting in context of the novelty and complexity of the flourishing research field.

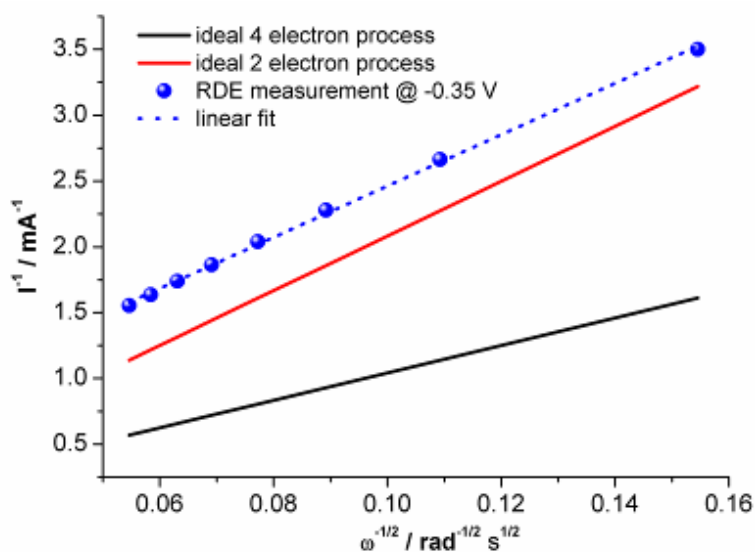


**Figure B32:** Koutecky - Levich plot achieved from the RDE data of *micro - Emim - TCB - 1400* at - 3.5 V vs. Ag / AgCl.

## C Conclusions

The needs for sustainable energy generation, but also a sustainable chemistry displayed the basic motivation of the current thesis. The single investigated cases, which are all related to the element carbon, can be assigned to two major topics. At first, the sustainable synthesis of “useful” carbon materials employing the process of hydrothermal carbonisation (HC) is described. In the second part, the synthesis of heteroatom-containing carbon materials for electrochemical and fuel cell applications employing ionic liquid precursors is presented.

On base of a thorough review of the literature on hydrothermolysis and hydrothermal carbonisation of sugars in addition to the chemistry of hydroxymethylfurfural (HMF), it is possible to apply mechanistic considerations, which potentially enable the control of the hydrothermal carbon structure. Especially when starting from high sugar concentrations and after short times of hydrothermal treatment, the acetalisation of HMF with sugar alters the reactivity of HMF, primarily by protecting the reactive aldehyde group. A set of ring-opening reactions leading to aldol condensations, electrophilic substitution reactions in between furans, as well as etherification reactions with subsequent release of formaldehyde are thought to promote polymerisation and cross-linking within the material. This finally leads to the conjugated carbon substructures, explaining the dark colour of hydrothermal carbon. Diels - Alder reactions within and in between substructures of the cross-linked network lead to further cross-linking, aromatisation and carbonisation. The proposed chemistry, being highly sensitive to nucleophilic species explains the impact of nitrogen containing additives, such as amino acids and proteins. The high reactivity of amines with carbonyl groups accelerates the condensation / polymerisation process *via* aldol-type reactions, leading to imine intermediates. Imines, which act as electron-rich dienophiles, also promote Diels - Alder reactions and the subsequent aromatisation / carbonisation to a larger extent as compared to the intermediates in the carbonisation of pure sugars.

As a new experimental tool for the manipulation of these reaction schemes, borax, which is known to complex sugars, is introduced as an additive for the hydrothermal carbonisation of glucose. It was found to be a highly active catalyst, resulting in decreased reaction times and increased carbon yields. Due to the non-covalent character

of this additive and the convenient access to the natural appearing mineral borax, the HC process can be even improved in terms of recyclability and sustainability. Contrary to the work of Riisager and Ståhlberg *et al.*, isomerisation and dehydration of glucose and fructose, catalysed by boric acid, were not found to be rate limiting steps in HC, but borax accelerates the carbonisation itself. Considering the introduced reaction pathway towards hydrothermal carbon (HTC), it is assumed that borax has a large effect on the acetalisation of aldehydes with sugars and hence influences the reactivity of HMF. While the reactivity of the formyl group is increased, a decreased reactivity of the hydroxyl group as leaving group and the furan ring are expected. Despite a two - sided influence on the process overall borax employment leads to an acceleration of carbonisation. In addition to the catalysing effect, borax also induces HTC particle gelation.

In a second part, this complexation with borax is exploited for the modification of the micro- and nanostructure of hydrothermal carbon. Following trends of the classical system of catalysed polycondensation between resorcinol and formaldehyde, the catalytic activity of borax was utilised to subtly control the particle size of HTC below, but not limited to the sub - 50 nm range, depending on the ratio of glucose to borax. From the borax - mediated aggregation of those primary species, low density, pure hydrothermal carbon aerogels with high porosity and specific surface area were produced. These are features previously missing from reported template - free HC routes. Electron microscopy and gas sorption experiments were used to investigate these *Carbogels*.

Since porous and conductive materials are highly desired in electrochemical applications, subsequent conversion of the porous HTC materials into more carbonised, porous carbon materials and the generated electrical conductivity were also investigated. Interestingly, a strong additional micropore generation, partially retaining the mesopore structure, at moderate carbonisation temperatures (*e.g.* 550 °C) was found, giving an overall specific surface area of about 600 m<sup>2</sup> g<sup>-1</sup>. This decomposition behaviour allows the easy and fast bottom - up generation of high surface area material without additional (chemical) activation. When the primary structural thickness falls below 10 – 20 nm, partial structural collapse is found, which is attributed to capillary forces. Regarding the reaction scheme, *retro* Diels - Alder reactions are likely to be the origin of the micropore

generation. Further carbonisation at higher temperatures results in the loss of the previously generated microporosity.

In summary, the presented borax - assisted synthesis is a simple, sustainable and scalable route and is expected to lay the basis for the development of a wide range of useful sustainable carbon - based products. The ability to control surface chemistry, morphology and textural properties provides a multidimensional approach towards porous carbon aerogels well - suited for potential applications in catalysis, chromatography and electrochemistry. Importantly, the system is based on a cost - effective, sustainable and scalable nanomaterials platform.

To conclude the first section of the thesis, a short series of experiments were carried out, for the purpose of demonstrating the applicability of the HC model to “real” biowaste as feedstock for the production of useful materials. Out of practical convenience, watermelon juice leftovers, which are extensively available (~ 20 million tons worldwide in 2009) were hydrothermally treated at 200 °C. Due to the presence of the amino acid L - citrullin, the resulting hydrothermal carbon is nitrogen - doped, and composed of defined, mostly separated spherical particles. Thus, no obstacles against the use of watermelon juice in advanced material syntheses were identified. This was further extended by successfully applying the watermelon juice as precursor in the synthesis of carboxy - enriched ion exchange resins by addition of acrylic acid as (co)monomer. It is proposed that, besides Diels - Alder addition, the polymerisation of acrylic acid was initiated by hydrothermal carbon particles, once sufficiently conjugated substructures to promote radical reactions were developed.

In part two of the present thesis, imidazolium- or pyridinium - based, cyano - containing ionic liquids were employed as precursors for the synthesis of high - performance, heteroatom - containing carbon materials. The ionothermal synthesis of carbonaceous materials directly from ionic liquids is a very recent research field, which is expected to expand rapidly. So far, mostly nitrogen - doped carbons were reported, but isolated reports on sulphur and boron - doped carbons can be found as well.<sup>[118, 119, 142, 143]</sup> Specifically, Paraknowitsch *et al.* reported on very desirable properties such as high



stability and electrical conductivity of nitrogen - doped carbons obtained from pyrolysis of the ionic liquids 1 - Ethyl - 3 - methyl - imidazolium - dicyanamide (Emim - dca) and N - methyl - 3 - butylpyridinium - dicyanamide (BMP - dca). They also reported on the respective mesoporous high surface area materials, obtained by employing various hard and soft templating strategies. Continuing this research, it was shown, that in addition to the described advantages, the liquid precursor state offers extra possibilities. A simple method to obtain highly microporous carbon materials, without silica hard templates and the often hazardous compounds required to remove them, was developed by mixing the reactive ionic liquid with an inert inorganic salt followed by carbonisation. This works both by dissolving the inorganic salt in the ionic liquid or by preparing a mixed salt melt at high temperatures. This so - called “salt templating” procedure most likely works *via* nanoscale phase separation of the inorganic salt, concurrently to ionic liquid polymerisation. Evaporation of the salt at high temperatures or post - synthetic washing finally generates micropores. This method can be regarded as an additional tool for shaping the micro- / mesostructure of ionic liquid based materials.

Due to its high thermal stability and low resistivity, ionic liquid based nitrogen - doped carbon was expected to perform well as an electrode material. Mesoporous nitrogen - doped carbon, still synthesised *via* the silica hard templating strategy, was tested for its activity in the electrocatalytic oxygen reduction reaction (ORR), which is the cathode reaction in polymer - electrolyte membrane fuel cells (PEMFCs). It could be shown that nitrogen - doped carbon derived from Emim - dca at 1000 °C represents a highly active, non - precious metal electrocatalyst for the ORR. The obtained results corroborate the assumption that nitrogen - doped carbon itself, and not metal traces accidentally introduced into the structure, catalyse the ORR. The nitrogen - doped carbon shows only slightly higher over - potential and comparable faradaic currents with respect to commercial 20 wt. % Pt on carbon catalyst and an electron transfer number of  $n = 3.58$ , indicating a direct reduction of oxygen to water ( $n = 4$ ).

By varying the ionic liquid precursor and the carbonisation conditions, it was also possible to design a non - metal electrocatalyst with high selectivity towards the production of hydrogen peroxide. Interpretation of the electrochemical rotating - disc - electrode measurements by employing the Koutecky - Levich equation revealed an

almost pure 2 electron mechanism. The concentration time behaviour towards the production of hydrogen peroxide was determined *via* photometric measurements, and the Faraday efficiency was calculated to be as high as 65.2 %. A selective electrochemical production of H<sub>2</sub>O<sub>2</sub> directly from hydrogen and oxygen is indeed highly desired and would not only be an example of green chemistry but may lead to a massive reduction of hazards and costs, as this could be done at the right point of time and directly at the place of demand. The electricity costs of the reported synthesis were calculated to be around 2.4 EUR cents per kg H<sub>2</sub>O<sub>2</sub>. As former research in this area suffers from non - specific, mostly precious metal catalysts, which catalyse the 4 electron pathway as well, inexpensive and selective nitrogen - doped carbon catalyst could nicely complement modern electrochemistry. XPS analysis did not allow a clear assignment of nitrogen binding sites to a certain electrochemical reactivity, *i.e.* the 2 or 4 electron process, and further experiments, including theoretical simulations, are needed to resolve this question. In a last example, the ionothermal carbon synthesis based on ionic liquids was expanded to the synthesis of graphitic boron carbon nitrides from the ionic liquid 1 - Ethyl - 3 - methylimidazolium - tetracyanoborate (Emim - TCB). A detailed view at the formation mechanism using TG - IR, FT - IR, solid - state NMR, Raman, WAXS, EELS, XPS and HRTEM showed that the employment of highly stable imidazolium - based ionic liquids opened a new solid formation pathway, different to that reported by Paraknowitsch *et al.* The solid formation in the studied case starts with the formation of a polyimidazole - type network, while cycloaddition reactions contribute to the material formation only in later stages. Carbonisation at 1400 °C gives the graphitic boron carbonitride with a weakly ordered structure, very similar to the case of ionic liquid based nitrogen - doped carbons. The comparably high temperatures are needed to structurally incorporate the highly oxophilic boron into the graphitic lattice. The electronic characterisation of the material shows that it is a p - type semiconductor with low resistivity and, again, high potential for electrode applications. The employment of “salt templating” strategies using caesium salts (together with Nina Fechler) generated high surface area boron carbon (oxy)nitride, which was shown to be another class of non - precious metal electrocatalyst with good activity for the 2 electron ORR in alkaline media. This is similar to recently reported data on boron - doped carbon nanotubes.<sup>[114]</sup> Especially for boron carbon (oxy)nitrides, the

very high surface areas obtainable by “salt templating” may also be interesting with respect to highly selective sorption properties.

## **D Applied Methods**

### **Electron Microscopy (SEM and TEM)**

Scanning Electron Microscopy (SEM) is an instrument allowing to image materials at high magnifications using the wave behaviour of accelerated electrons. As the wavelength limits the resolution highly accelerated electrons, possessing small de Broglie wavelength, allow displaying of much smaller structures as compared to optical spectroscopy. Among other possible information (*e.g.* energy dispersive X-ray mode) it provides structural details such as texture, morphology and particle / pore size of conductive or likewise prepared samples. An electron beam is produced by a hot cathode at the top of the microscope. The electron beam is electrostatic forced to a vertical path through the evacuated microscope. Different lenses arrange and focus the beam, which is scanning the probe in a series of lines and frames. Based on geometrical considerations, secondary electrons generated at the edges and at convex surfaces have higher probability to escape from the surface and reach the detector, while secondary electrons from shallow surfaces have the least probability to escape from surface and reach the detector. Different quantities of generated electrons originate the contrast, which finally allows imaging. Through this contrast mechanism, a magnified image of the sample with topological details of the sample surface can be obtained.

SEM imaging was performed after Au/Pd sputtering of the non-conductive sample on carbon sample holders in a LEO 1550-Gemini system (acceleration voltage: 0.1 to 30 kV).

Like in the case of SEM an accelerated electron beam is used for the imaging of materials. In contrast, in transmission electron microscopy (TEM) the transmission of electrons through a very thin sample is used to obtain even higher resolutions. The contrast originates from the differences in transmittance. This is not only due to the sickness of the sample, but also due to the materials composition. The electrons interact in several ways with the solid material, namely absorption, diffraction, and elastic or inelastic scattering. Scattering processes result from interaction of the electrons with the positively charged nuclei of the sample. Heavy elements therefore lead to stronger scattering, which

results in fewer electrons reaching the image plate. Hence, sample regions containing these elements appear comparably dark. On the other hand areas only containing lightweight elements, such as typical organic compounds, result in limited scattering of electrons and therefore appear bright. At very high resolution (HRTEM), the technique is unique providing a real space image on the atomic arrangement in nanocrystals and on its surface. Nowadays, it is a versatile tool which provides atomic resolution lattice images and in addition chemical information at a spatial resolution of 1 nm or better. The chemical information is obtained using an additional electron spectrometer to perform electron energy loss spectroscopy (EELS). TEM imaging was performed with a TEM type Zeiss EM 912 $\Omega$  using 120 kV acceleration voltage. HRTEM measurements were performed at Fritz-Haber-Institute, Berlin on a Phillips TEM/STEM CM 200 FEG TEM equipped with a Field-emission gun operated at 200 kV and at ZELMI / TU Berlin using a FEI Tecnai G<sup>2</sup> 20 S-TWIN equipped with a LaB<sub>6</sub> cathode operated at 200 kV. Samples were prepared using carbon coated standard Plano copper grids, which were either dipped into fine powder samples or coated with 7 $\mu$ l of a sonicated dilute dispersion of the powder in ethanol with subsequent drying in air for at least 30 minutes.

### **Electron Energy Loss Spectroscopy (EELS)**

Under employment of an additional electron spectrometer in a HRTEM a lot of chemical information of an investigated material can be obtained. The inelastic scattered electrons of an energetically narrow electron beam are detected regarding their energy loss due to the scattering at the sample of interest. Energy loss determining phenomena include phonon excitations, inter- and intraband transitions, Plasmon excitations, inner shell ionisations and Čerenkov radiation. Inner shell ionisations lead to an element characteristic energy loss, the so-called core-loss region. Although quantification is not trivial, EELS can be used to evaluate the elemental composition of the as-analysed sample in a HRTEM. The core-loss signal arises from excited specimen electrons from the deeply bound initial core states to the final states including features indicative of the atoms local bonding environment. This includes both the atomic and the electronic local arrangements.

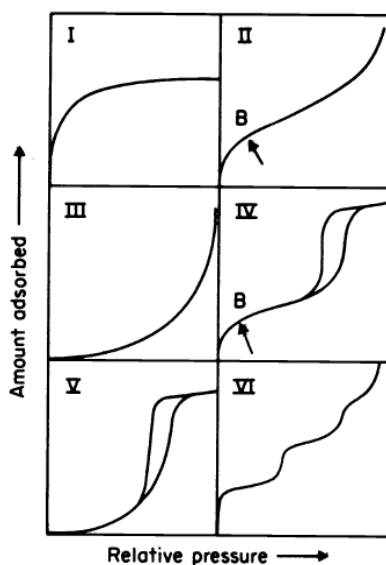
EELS measurements were also performed at Fritz-Haber-Institute, Berlin (see TEM).

## Nitrogen Sorption

Nitrogen sorption is a powerful and widely used gas sorption technique to characterise porous materials. The quantity and character of porosity is evaluated by using an accurate amount of sample as adsorbent for the adsorption of nitrogen gas at the constant temperature of 77 K (liquid nitrogen). The amount of gas dosed into the measuring cell is evaluated as in dependence of the relative pressure ( $p/p_0$ ). The following desorption is measured as well. The respective plot, *i.e.* the nitrogen sorption isotherm indicates the type and quantity of pores. The IUPAC differentiate between three classes of porous materials depending on the pores diameters:

***micropores (up to 2 nm) < mesopores (2 – 50 nm) < macropores (bigger than 50 nm)***

The three classes possess different adsorption effects which allow the assignment of characteristic isotherm shapes to certain pores. One can distinguish 6 types of isotherms:



Types of nitrogen sorption isotherms:

Pure & App!. Chem., Vol. 57, No. 4, pp. 603—619, 1985.  
Printed in Great Britain. ©1985 IUPAC

Type I isotherms are characteristic for pure microporous materials with low external surface area. The micropores are filled at relatively low partial pressures of  $p/p_0$  less than 0.1. Type II and type III isotherms describe the adsorption on macroporous or non porous

adsorbents with strong and weak adsorbate-adsorbent interactions, respectively. The point B, highlighted with an arrow, represents the stage where the monolayer is completely built up and multilayer formation begins. Type IV isotherms are characteristic for mesoporous materials. Herein, the hysteresis loop is a feature of the capillary condensation of gas in mesopores. Different shapes of hysteresis loops can be observed. It is admitted that the different shapes of the hysteresis are related to different pore structures in terms of shape, pore connectivity and cavitations in the material, which are influencing the capillary condensation inside the mesopores. Type V isotherms are observed for mesoporous materials with weak adsorbate-adsorbent interactions. Finally type VI isotherms represent the stepwise adsorption of several layers on a non porous surface. Employment of special models with distinct approximation allows determination of the specific surface area and pore size distribution.

Nitrogen sorption measurements were performed at  $T = 77$  K on a Quantachrome Masterprep system equipped with a Quandrasorp SI pore size analyser. The pore size distributions of the carbon materials were determined by using either QSDFT or NLDFT model of the both nitrogen adsorption and desorption isotherms. Samples were properly degassed before measurement. The specific surface area was calculated by applying BET (Brunauer-Emmett-Teller) method of analysis.

## **Fourier Transform Infrared / Raman Spectroscopy**

The Fourier transform (FT) infrared (IR) and Raman spectroscopy provide information about molecular structures by their rotational and vibrational-rotational properties excited by laser illumination. Both methods are the others complements, Raman concerning the inelastic scattered radiation and IR measuring absorbed or emitted photons. To detect rotations / oscillations in IR spectroscopy the molecules dipole has to change within the vibration, while for Raman spectroscopy a change in the polarity is required. The measurements can be used to determine functional groups within the material or detect substances by their characteristic spectrum. Not only molecular, but also lattice vibrations, which lead either to a changing dipole or polarity, can be observed. The IR spectrum is a

plot of the percentage of the infrared beam transmitted through or absorbed by the sample versus the energy-proportional wavenumber with the unit  $\text{cm}^{-1}$ . While IR spectroscopy is based on scanning of the illuminated laser energy, Raman uses only one specific laser energy and detects the energy shift (Raman shift) at which scattering signals appear. The position and relative strength of the peaks allows insight into the structure of materials or the comparison to spectra of reference material. A very simple model of the motion of the molecules can be made using mass points to represent the atoms and springs to represent the bonds. The mathematical description of this model via classical mechanics indicates the role of mass and spring (*i.e.* bond) strength. The vibration frequency *i.e.* the respective wavenumber is proportional to the ratio of bond strength to mass.

FT - IR was performed with a Varian 600 FTIR Spectrometer equipped with an attenuated total reflection (ATR) support. FT - Raman spectra were acquired using a WiTec Confocal Raman Microscope R-300, frequency doubled green 532 nm Nd/YAG laser with optical resolution diffraction limited to 200 nm laterally and 500 nm vertically and with spectral resolution down to 0.02 wave numbers.

## **X-Ray Photoelectron Spectroscopy**

X-ray photoelectron spectroscopy (XPS) is a quantitative spectroscopic ultra high vacuum technique to measure materials properties such as the elemental composition and the chemical and electronic state of the materials elements. Specimens are irradiated with X-ray photons of energies higher than 100 eV. Due to the high excitation energy in XPS mostly deep core-level electrons are produced via the photoelectric effect, leading to the term “core level spectroscopy”. The X-ray photons penetrate the sample to a micrometer but effectively produce detectable electrons only from the surface to 1 - 10 nm depth. The detected binding energies are characteristic for each element allowing the evaluation of the elemental composition. Due to the Auger process, where electrons from higher states (valence states) change over to the formed free core-states by transferring their energy to additionally emitted electrons, it is possible to detect the elements chemical and electronic state, such as the specific binding motif.



XPS-analysis of the samples was performed using a Thermo Scientific K-Alpha ESCA instrument equipped with aluminium  $K\alpha$  1, 2 monochromatised radiation at 1486.6 eV X-ray source. The XPS measurements were carried out using monochromatic Al- $K\alpha$  radiation ( $h\nu = 1486.6$  eV). Photoelectrons were collected from a take off angle of  $90^\circ$  relative to the sample surface. The measurement was done in a Constant Analyser Energy mode (CAE) with 100 eV pass energy for survey spectra and 20 eV pass energy for high resolution spectra. Charge referencing was done by setting the lower binding energy C 1s photo peak at 285.0 eV C 1s hydrocarbon peak. Surface elemental composition was determined using the standard Scofield photoemission cross sections.

### **Wide-Angle X-Ray Scattering**

X-rays are defined as short-wavelength electromagnetic radiation produced by the deceleration of high-energy electrons or by electronic transitions involving electrons in the inner orbitals of atoms. X-ray diffraction (XRD) is based on a monochromatic X-ray beam that hits the sample and is scattered from certain lattice planes, as the lattice distance and the radiation wavelengths are in the same range. Depending on the geometry i.e. the atoms connectivity or crystal structure in relation to the incidence angle (wave vector), positive interference may lead to reflections, which finally produce the characteristic diffraction pattern of the investigated material. Mathematically, this is described by Bragg's law. The line profiles of the so-called Bragg reflections increases in width with decreasing size and increasing lattice imperfection, indicating the crystallinity or long-range order of the material.

WAXS measurements were performed on a Bruker D8 Advance machine. The X-ray tube was operated at 40 kV and 40 mA. The emitted Cu- $K\alpha$  radiation ( $\lambda = 0.154$  nm) was monochromatised by a multilayer Göbel mirror. An energy dispersive detector (Sol-X, Bruker) was used to ensure low background noise, by filtering out the inelastic scattered photons. The samples were measured on plastic or silicon sample holders in reflection geometry as coupled  $\theta$ - $2\theta$  scans.

## Ultraviolet-Visible Spectroscopy / Photometry

Ultraviolet-Visible Spectroscopy (UV/Vis) refers to absorption spectroscopy in the ultraviolet-visible range meaning that measurements are directly related to the colour of samples. Processes interacting with radiation of that energetic part of the spectrum are due to electronic transitions within the material. Usually, a beam of light with constantly changing wavelength is irradiated in transmission mode through a transparent cuvette of defined thickness, which contains a dilute solution of the sample. The absorbance follows the famous Beer-Lambert law,

$$A = -\lg\left(\frac{I_1}{I_0}\right) = \varepsilon_\lambda \cdot c \cdot l$$

where A is the absorbance, I<sub>1</sub> the intensity of the transmitted light, I<sub>0</sub> the intensity of incident light,  $\varepsilon_\lambda$  the spectral absorption coefficient, c the concentration of the absorbing species and l the length of the transmitted sample. The probably simplest application of UV / Vis spectroscopy is to measure concentrations by photometrical means.

The set of absorption measurements on different dilute standard solutions at a distinct wavelength (usually absorption maxima) are conducted to obtain a linear calibration line. Afterwards the concentration of an unknown sample can simply be calculated by measuring the absorbance and calculation using the linear line equation.

Photometric measurements of hydrogen peroxide solutions were performed using Merck “Wasserstoffperoxid-Test”, which is a test kit for the concentration range of 2.0 - 20 mg L<sup>-3</sup>. KOH base was used to neutralise samples before measurement, as instructed by the manual. The pure base, as well as neutralised base with HCl were and cross - checked towards the test reaction.

## Thermogravimetric Analysis

Thermogravimetric analysis (TGA) presents a thermal analysis method in which the mass change is adequately followed by thermal treatment of sample. Commonly used heating rates are 10 K min<sup>-1</sup> and typical atmospheres are inert or reactive gas depending on the

actual interests. The detected mass change, usually being a mass loss due to the production of volatile species, elucidates the thermal stability and the reactivity towards pyrolysis. In case of synthetic air as a reactive gas, oxidation is observed and can lead to an increase of mass.

TGA was performed using a TG 209 F1 machine from Netzsch, Al<sub>2</sub>O<sub>3</sub> crucibles were used and a nitrogen gas flow of 15 mL min<sup>-1</sup> with a heating rate of 10 K min<sup>-1</sup>.

TG-IR analysis was performed on a 20 mg sample by using a Netzsch STA 409 C/3/F with a TASC 414/3 system controller set at 180 - 200 °C at heating rate of 10 K min<sup>-1</sup> under N<sub>2</sub> at 100 mL min<sup>-1</sup>. IR spectra of volatiles were recorded on a Bruker EQUINOX-55 FT instrument equipped with a liquid N<sub>2</sub> cooled MCT detector with a resolution of 4 cm<sup>-1</sup> and 64 scans.

### **Differential Scanning Calorimetry**

Differential Scanning Calorimetry (DSC) presents a calorimetric method, which allows precise determination of phase transitions, glass transitions and other phenomena being connected to a change in the heat capacity. As an example the thermoenergetic course of reactions can be investigated. Thereby the heat flow is measured as compared to a certain reference sample. Common diagrams plot the heat flow versus time or temperature. Characteristic endothermal or exothermal peaks can be observed depending on the heating rate, which is typically 10 K min<sup>-1</sup>.

### **Elemental Microanalysis / Inductive Coupled Plasma-Optical Emission Spectroscopy**

Elemental Microanalysis is a burning method to quantify the elemental composition in terms of carbon, hydrogen, nitrogen and sulphur content. Samples are catalytically burnt at 1100 °C in oxygen atmosphere and the decomposition gases (CO<sub>2</sub>, H<sub>2</sub>O, SO<sub>2</sub> and N<sub>2</sub>) accurately quantified using heat conductance detectors. Inductive Coupled Plasma (ICP) -

Optical Emission Spectroscopy (OES) is based on the element-characteristic atom spectra. More precisely the ions emission, induced by argon plasma is used to quantitatively measure a materials composition subsequent to its chemical digestion by spectroscopic means.

A VARIO EL elemental analysis instrument from Elementar Analysensysteme was used to determine the carbon, nitrogen, hydrogen and sulphur content of the samples.

ICP-OES Optima 2100 DV from Perkin Elmer was used. Before measurement the sample was microwave-assisted acid chemical digestion was conducted for solubilisation.

### **Nuclear magnetic resonance spectroscopy**

Nuclear magnetic resonance (NMR) spectroscopy is a non-destructive method based on radio-frequency absorption / emission of NMR-active cores while the nuclear spins oscillate and reorient under internal and external magnetic fields. The local environments around the observed nuclei and the mobility of the nearby atoms or molecules greatly influence the oscillation frequency and reorientation times of the observed nuclei by superposition of the respective fields.

Liquid state NMR techniques are a well-known powerful tool in the characterisation of solutions. The advantages of NMR spectroscopy are high sensitivity towards the chemical environment of active cores and the variety of cores ( $^1\text{H}$ ,  $^{11}\text{B}$ ,  $^{13}\text{C}$ ,  $^{14/15}\text{N}$ ,  $^{17}\text{O}$ ,  $^{19}\text{F}$ ,  $^{29}\text{Si}$ ,  $^{31}\text{P}$  *etc.*) which can be investigated. NMR spectroscopy is also an interesting technique for the characterisation of solid materials. However, in contrast to solution NMR in solid state NMR very broad peaks are observed due to anisotropic or orientation-dependent interactions. In principle high-resolution solid state NMR spectra can provide the same type of information available from corresponding solution NMR spectra, but advanced techniques/equipment are required, including magic-angle spinning (MAS), cross-polarisation (CP), special pulse sequences, enhanced probe electronics and so forth. There are a variety of nuclei such as and many others that can be used as probes in solid state NMR because of their NMR activity.

$^1\text{H}$ - und  $^{13}\text{C}$ -NMR spectra in solution were obtained by using deuterated solvents with a Bruker DPX-400 spectrometer with frequencies of 400.1 MHz ( $^1\text{H}$ ) and 100.6 MHz ( $^{13}\text{C}$ ).  $^{13}\text{C}(^1\text{H})$ -CP-NMR spectra (cross polarisation / *magic angle* spinning) for solid state samples were obtained using a Bruker Avance 400 spectrometer with a frequency of 100.6 MHz, under employment of a Bruker 4 mm double resonance-sample holder with a MAS rate of 10 kHz. Other  $^{13}\text{C}$  solid state Magic Angle Spinning (MAS) NMR experiments were acquired on Bruker Avance 300 MHz (7 T) spectrometer using the 4 mm zirconia rotors as sample holders spinning at MAS rate  $\nu\text{MAS}= 14$  kHz. The chemical shift reference was tetramethylsilane (TMS;  $\delta= 0$  ppm). Proton-to-carbon CP MAS was used to enhance carbon sensitivity. Cross-polarisation transfers were performed under adiabatic tangential ramps to enhance the signal with respect to other known methods.

$^{11}\text{B}$  solid state Magic Angle Spinning (MAS) NMR experiments were acquired on Bruker Avance III 700 MHz (7 T) spectrometer at MAS rate  $\nu\text{MAS}= 22$  kHz. The chemical shift reference was boric acid. Recycle delay were 5 s. Number of transients is 64 and  $t_{90^\circ} = 3$  ms.

### **Spark plasma sintering**

Spark plasma sintering (SPS) is a pulsed DC current sintering method. In case of conductive samples in contrast to hot pressing methods the heat is generated internally while pressing the specimen. This allows high heating or cooling rates of up to  $1000 \text{ K min}^{-1}$ .

Spark plasma sintering was carried out for ionic liquid-based materials under vacuum with a heating rate of  $100^\circ\text{C min}^{-1}$  at pressures of 11 kN on a circular area of 2 cm diameter (= 35 MPa) with a maximal temperature of  $1400^\circ\text{C}$  for 5 minutes at *ca.* 530 A and *ca.* 4.8 V.

### **Seebeck coefficient and electric resistance**

Seebeck coefficient and electric resistance were measured with an Ulvac ZEM-3 thermal analyser in a typical four point probe setup in vacuum at temperatures of up to  $1000^\circ\text{C}$ .

## E Experimental Part

### A2.1

20 ml of 30 wt.% aqueous glucose solutions with and without 500 mg borax (sodium tetraborate,  $\text{Na}_4\text{B}_2\text{O}_7 \cdot 10 \text{H}_2\text{O}$ ) were poured into glass vials and heat treated in Teflon lined autoclaves at 200 °C for 1, 2, 3, and 4 hours for comparison.

### A2.2

20 ml of 30 wt.% aqueous fructose solutions with and without 500 mg borax (sodium tetraborate,  $\text{Na}_4\text{B}_2\text{O}_7 \cdot 10 \text{H}_2\text{O}$ ) were poured into glass vials and heat treated in Teflon lined autoclaves at 140 °C for 2, 3, and 4 hours for comparison.

### A3.1

20 ml of 30 wt.% aqueous glucose solutions with 100, 250, 500, 750 and 1000 mg of borax (sodium tetraborate,  $\text{Na}_4\text{B}_2\text{O}_7 \cdot 10 \text{H}_2\text{O}$ ), denoted as Carbogels X, where X corresponds to the used amount of borax in milligrams, were poured into glass vials and heat treated in Teflon lined autoclaves at 180 °C for 8 hours. After cooling, non-incorporated soluble compounds including borax were then removed by  $\text{H}_2\text{O}$  and ethanol extraction (until colour disappeared), followed by further solvent exchange with excess  $\text{H}_2\text{O}$  prior to freeze drying.

Samples of all Carbogels were further carbonised to either 550 or 900 °C in nitrogen atmosphere using a heating rate of  $10 \text{K min}^{-1}$  and an isothermal period of 1 hour at the desired temperature.

### A.4

Watermelons were purchased at fruit merchant (Birlik Market / Kottbusser Tor Berlin). The pulp was separated from the peel and minced with a masher. The mixture was centrifuged and decanted five times 30 minutes at 7000 rpm. The resulting faint yellow solution was stored at 4 °C. As reference an aqueous solution of the pure glucose

(10 wt. %) was prepared and also stored at 4 °C. Hydrothermal carbonisation was carried out by sealing 20 ml of the juice/solution into a glass vial inside a Teflon lined autoclave. For the synthesis of functional hybrid carbon 5, 10 and 20 wt.% of acrylic acid were added to the watermelon juice, respectively. The autoclaves were heated to 200 °C for 20 hours. The solid product was washed with 750 ml of distilled water and vacuum dried at 70 °C over night.

#### B0.1

1g LiCl/KCl salt mixture ( $\text{LiCl}/(\text{LiCl}+\text{KCl}) = 0.592$ ) was grinded and thoroughly mixed with 1g BMP-dca. The mixture was subsequently placed in an alumina crucible and carbonised in an inert oven under nitrogen flow, which is a standard procedure for the preparation of IL - based products. In this case a heating rate of  $10 \text{ K min}^{-1}$  and 1 h isothermal treatment @ 900 °C was used.

#### B1.1

Commercial silica (*i.e.* Ludox® particles) was employed as hard templates. With a ratio of Emim - dca / silica of 1 g : 1 g the precursors were mixed and pyrolysis under nitrogen flow at 1000 °C (heating rate  $10 \text{ K min}^{-1}$ , 1 h isothermal @ 300 °C and 1 h @ 1000 °C) was performed. Subsequent removal of the silica template employing 4 M  $\text{NH}_4\text{HF}_2$  solution ( $40 \text{ mL g}^{-1}$ ) and washing with distilled water, gave the porous nitrogen doped replica, as fine black powder.

To perform electrochemical testing a standard ink was prepared from 5 mg of catalyst with 95  $\mu\text{l}$  Nafion® binder solution and 350  $\mu\text{l}$  of ethanol. A 7  $\mu\text{l}$  aliquot was applied to a freshly polished glassy carbon rotating - disc electrode (diameter ~ 5 mm) to prepare a catalyst thin film. Electrochemical tests were performed in 0.1 M KOH solution in a standard three - electrode setup with an Ag / AgCl reference electrode using Gamry Reference 600 potentiostat (Gamry Instruments) and Gamry EIS 300/Physical Electrochemistry software.

#### B2.1

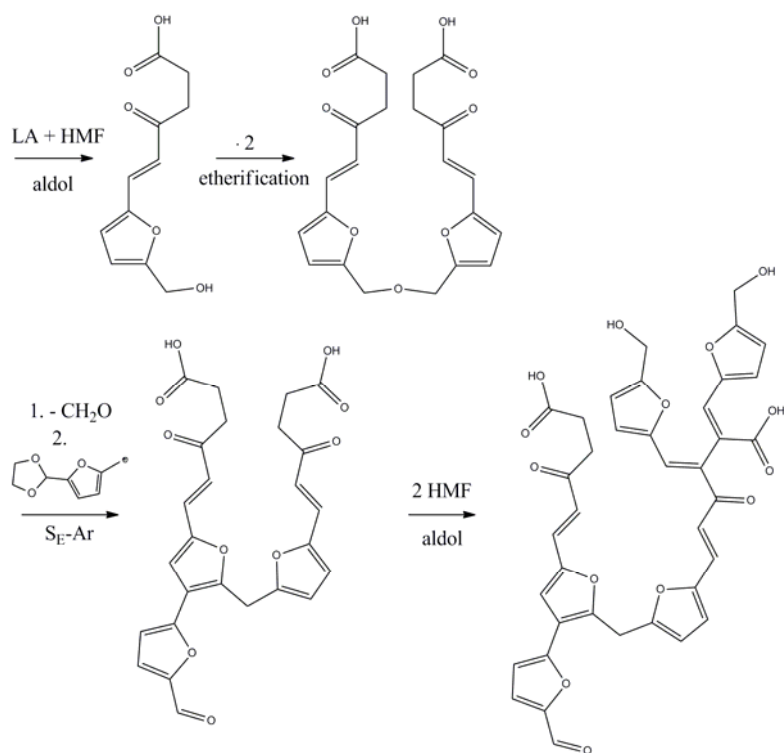
A 40 wt.% aqueous dispersion of silica nanoparticles (Ludox® HS40), Nafion 117 solution (5 wt. %) and  $\text{NH}_4\text{HF}_2$  were achieved from Aldrich and the 0.1 M potassium hydroxide solution, same as the peroxide tests were purchased at Merck KGaA. All chemicals were used as received without further purification. 2 g BMP-dca were mixed with 5 g of the 40 wt.% Ludox dispersion, transferred into alumina crucibles and carbonised afterwards. The thermal treatment was conducted under nitrogen gas flow in a VMK 80 S lab oven (Linn High Therm GmbH). After half an hour of purging, the sample was heated to 800 °C with a heating rate of 10 K min<sup>-1</sup>. The resulting black solid was ground and treated with 4 M  $\text{NH}_4\text{HF}_2$  solution to remove the silica. Washing with water and subsequent drying gives a fine, black powder. The electrochemical characterisation was conducted using the rotating disc electrode (PINE Instruments, USA) technique in a custom made three compartment electrochemical glass cell and a commercial potentiostat (VSP-5, BioLogic, France). The three electrode setup consists of a Pt mesh as counter electrode, a reversible hydrogen electrode (Hydroflex HREF, Gaskatel, Germany) as reference electrode and a commercial fixed glassy carbon electrode (PINE Instruments, USA) with a diameter of 5 mm (0.196 cm<sup>2</sup>) as working electrode. For the preparation of the working electrode with a thin catalytic film, around 15 mg catalyst was suspended in 1.99 ml pure water, 0.5 ml iso-propanol and 10 µl Nafion (5 wt.% solution). After sonification, 10 µl of catalyst suspension was put onto the well polished glassy carbon electrode and dried in air for 10 min at 60 °C. All measurements were conducted at room temperature.

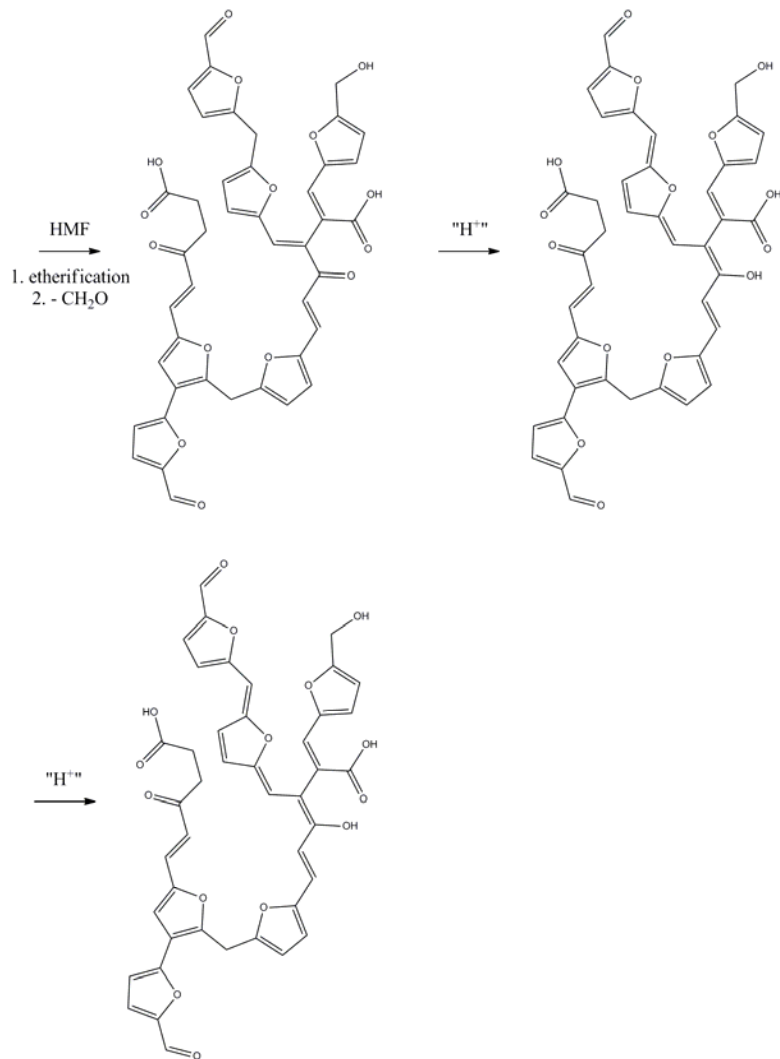
Emim - TCB was heated under nitrogen gas flow to different temperatures (heating rate: 10 K min<sup>-1</sup>, isothermal period at  $T_{\text{max}}$  for 1 hour), 450, 600, 800, 1000, 1100, 1200, 1300, 1400 °C. To perform electrochemical testing a standard ink was prepared from 5 mg of catalyst with 95 µl Nafion® binder solution and 350 µl of ethanol. A 7 µl aliquot was applied to a freshly polished glassy carbon rotating - disc electrode (diameter ~ 5 mm) to prepare a catalyst thin film. Electrochemical tests were performed in 0.1 M KOH solution in a standard three - electrode setup with an Ag / AgCl reference electrode using Gamry Reference 600 potentiostat (Gamry Instruments) and Gamry EIS 300/Physical Electrochemistry software.

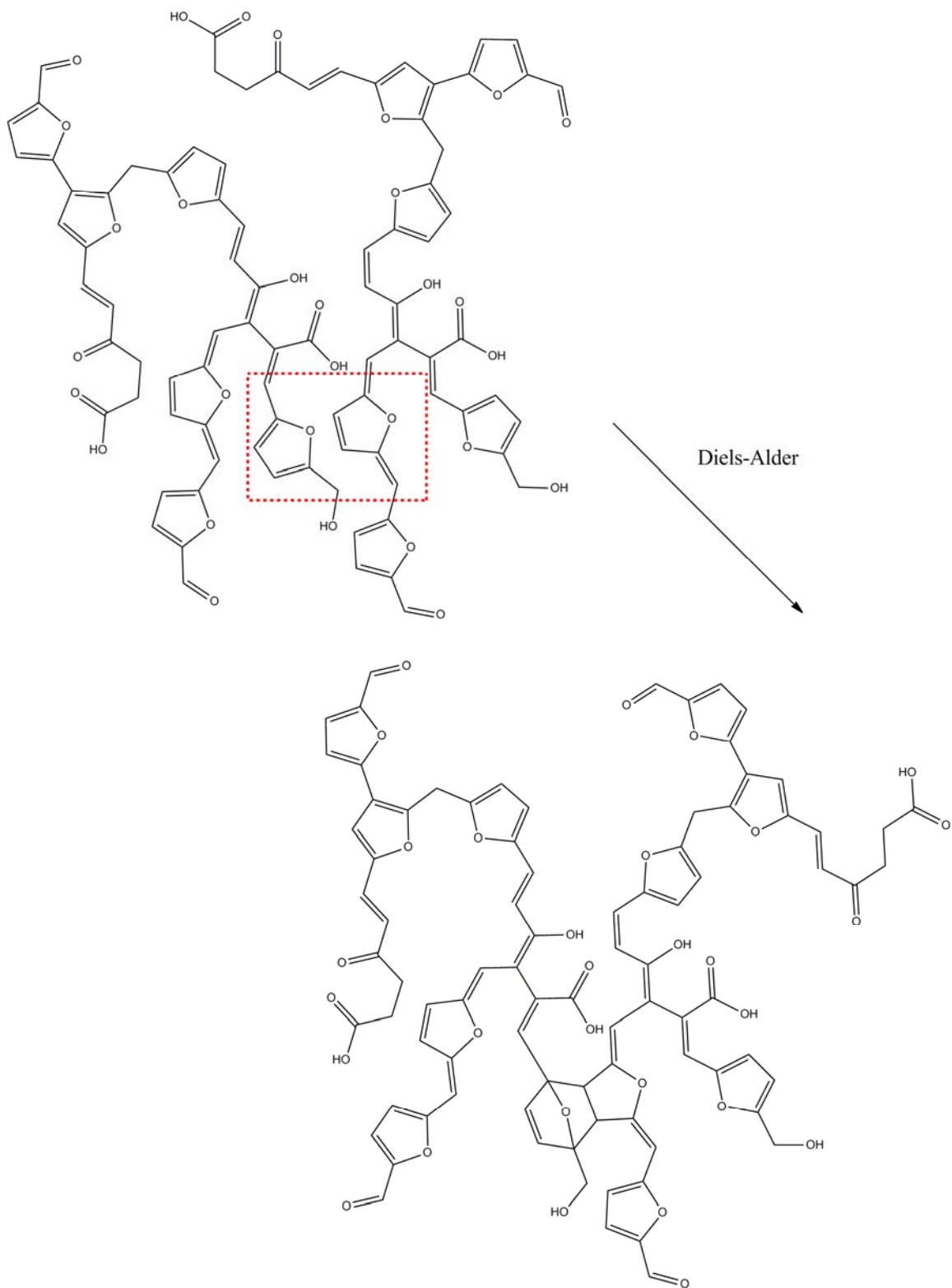


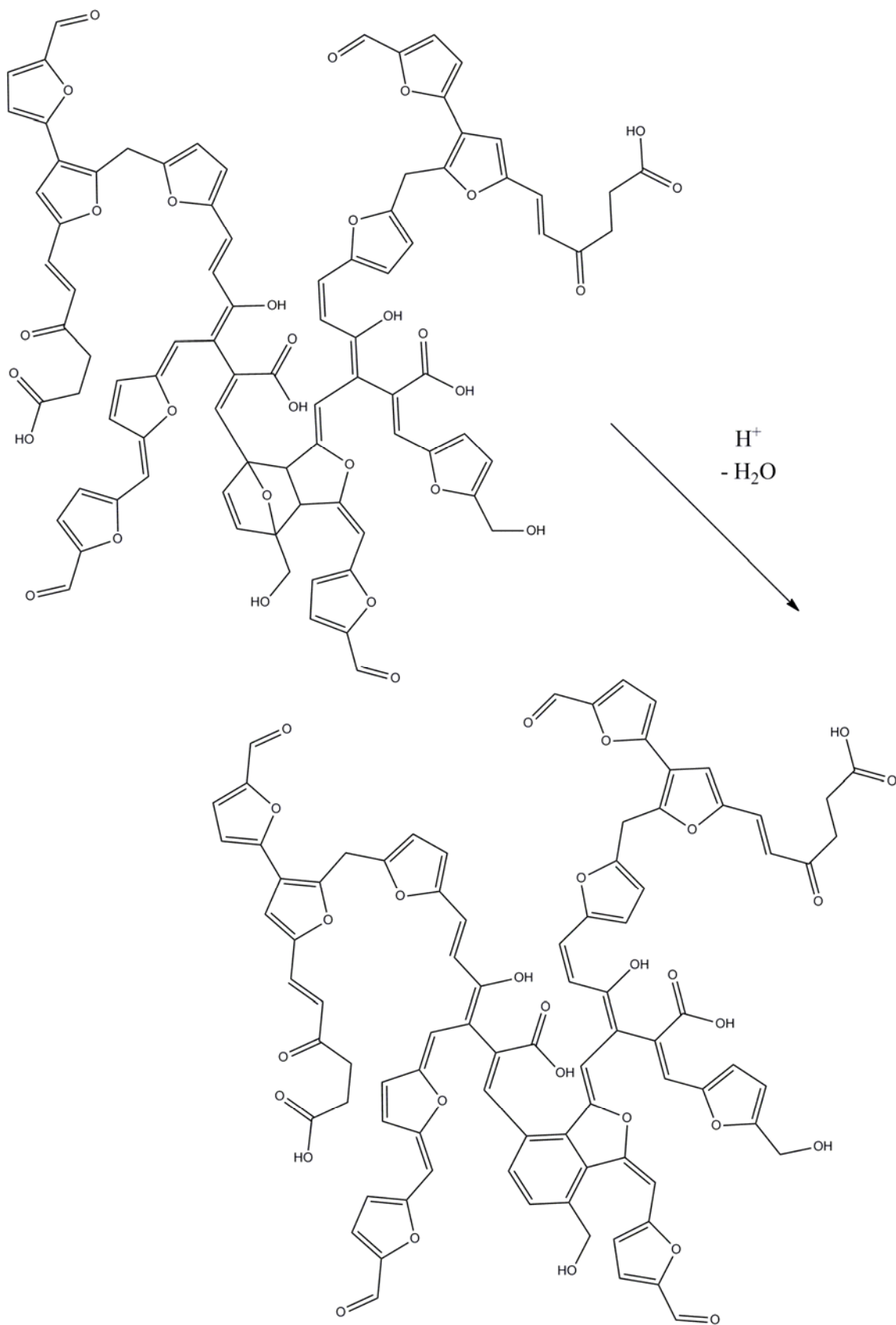
## F Appendix

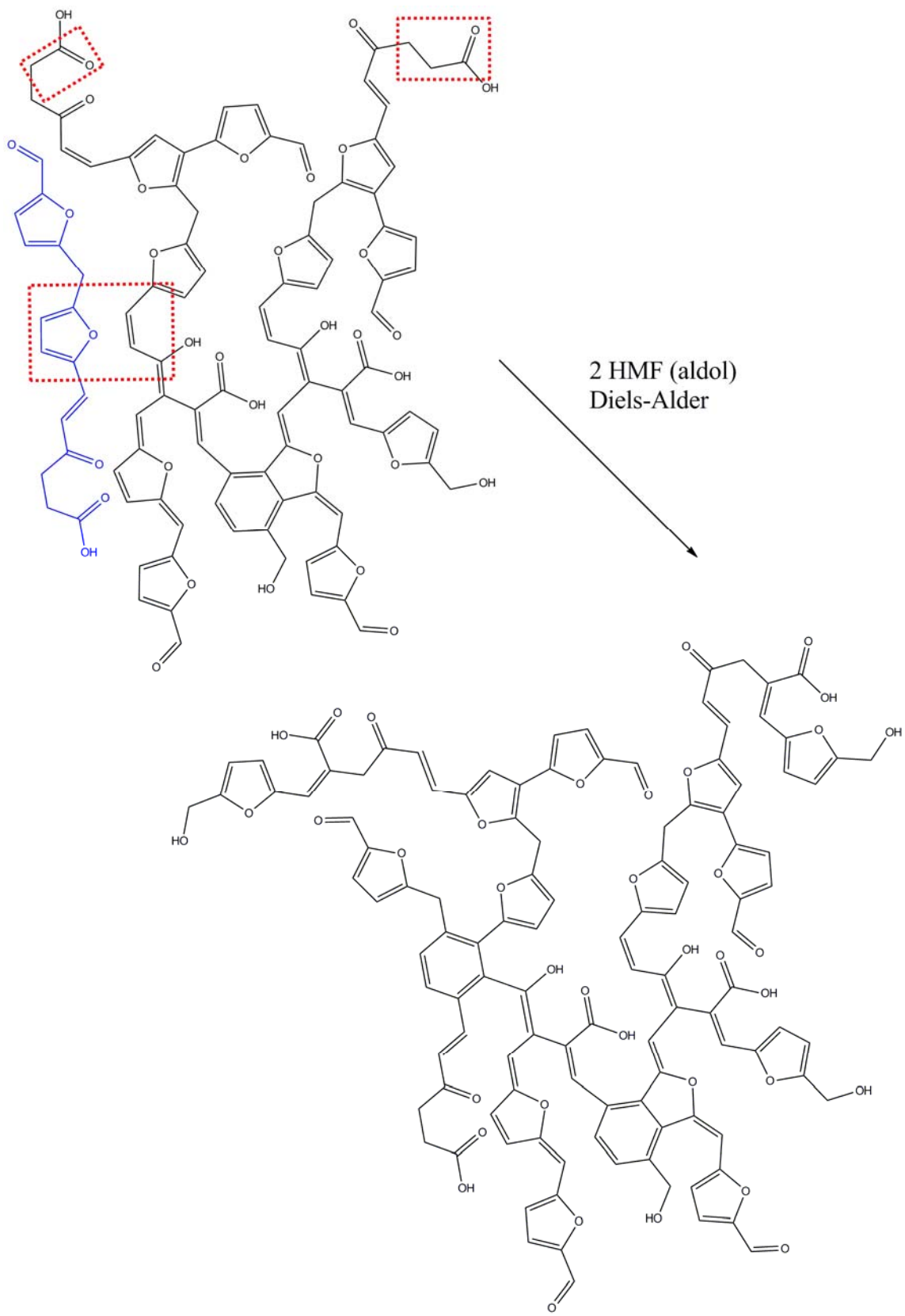
Exemplary reaction sequence within the hydrothermal carbonisation of glucose.

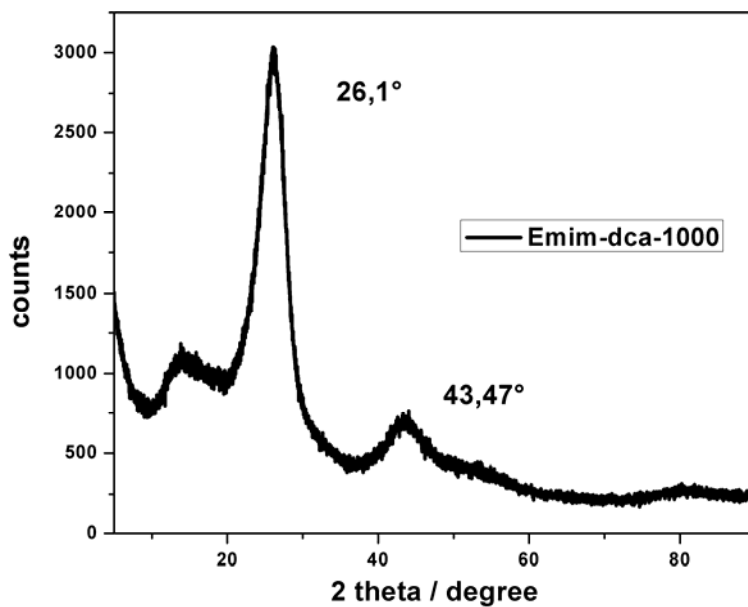




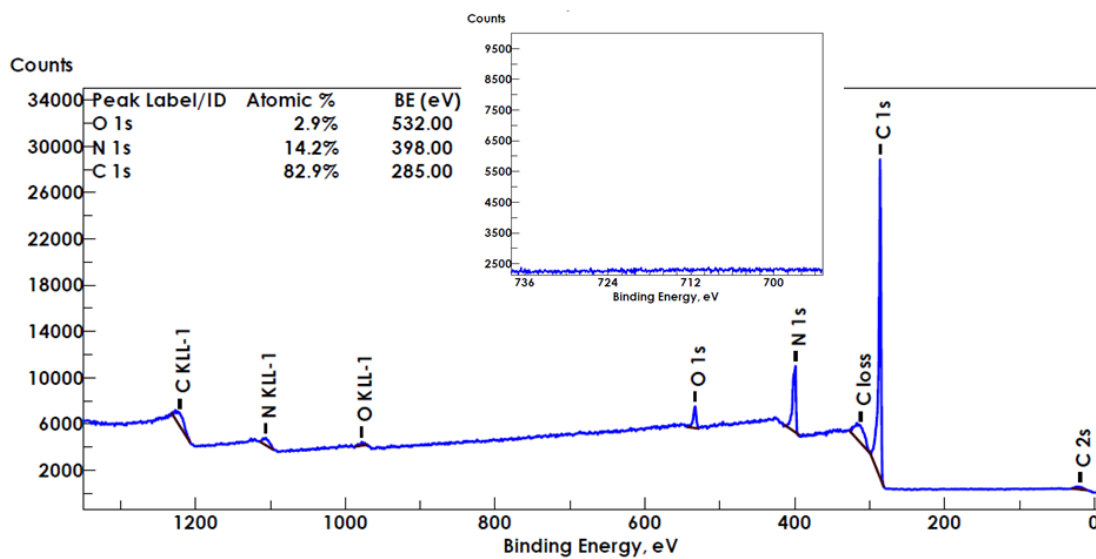




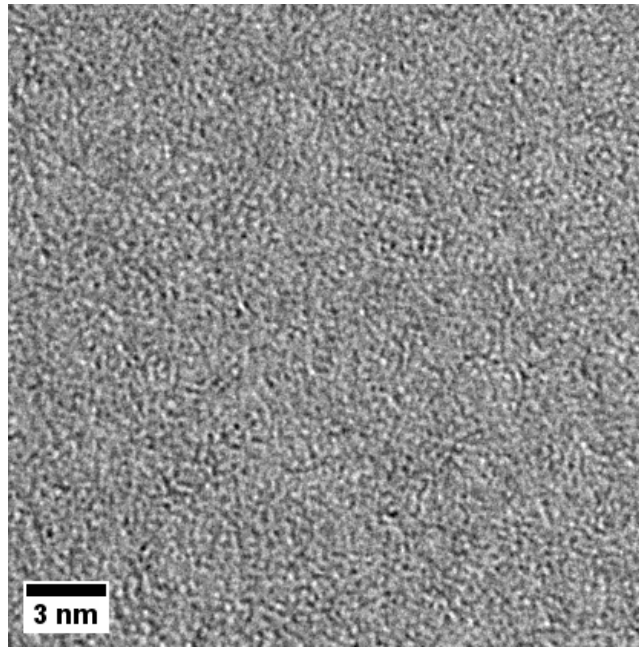




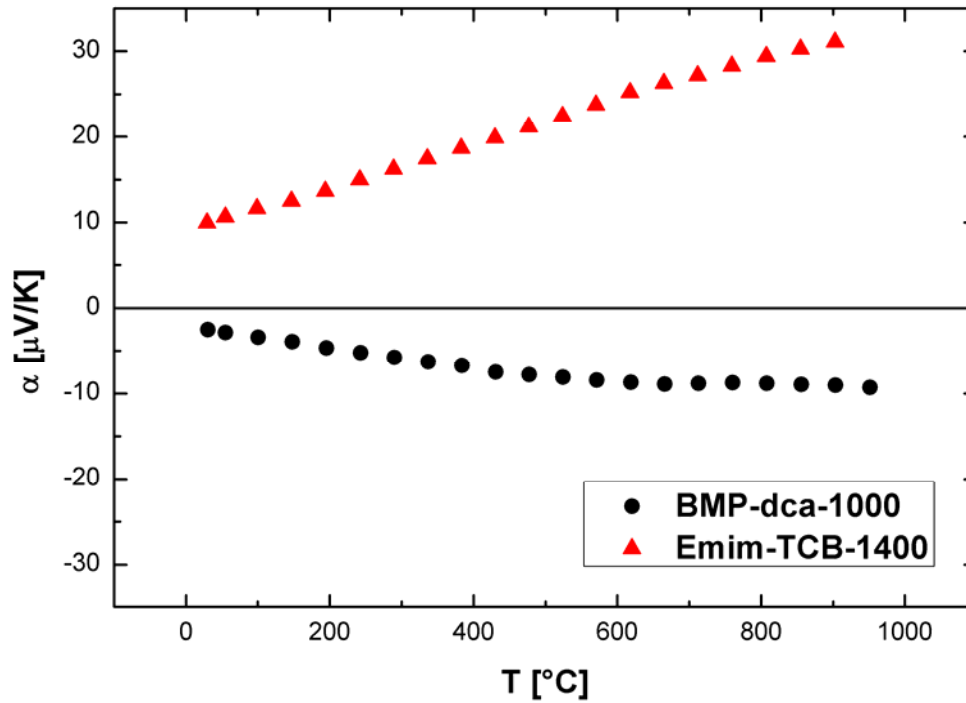
XRD pattern of Emim-dca-1000



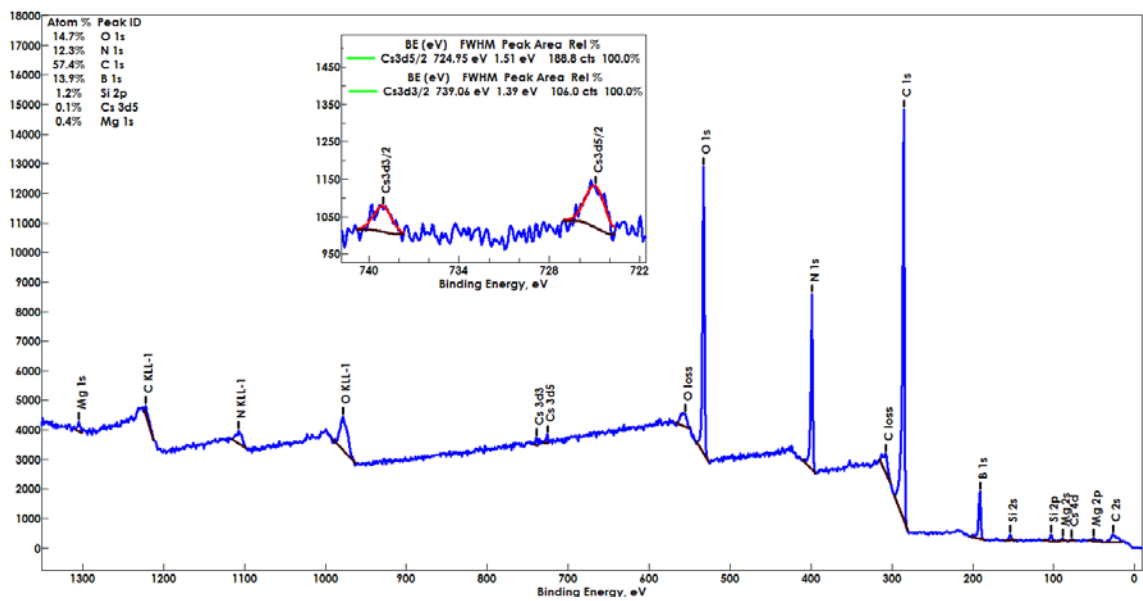
XPS survey spectrum of meso-BMP-800. Inset: High resolution spectrum in the region of iron (F 2p).



HRTEM image of amorphous carbon from carbon film on the TEM grid.



Seebeck coefficients of spark-plasma sintered BMP-dca-1000 and Emim-TCB-1400 at different temperatures (20-950 °C).



XPS survey spectrum of micro-Emim-TCB-1400. Inset: High resolution spectrum in the region of caesium (Cs3d3/5; Cs3d3/2).



## G References

- [1] J. Kunze, U. Stimming, *Angewandte Chemie International Edition* **2009**, *48*, 9230.
- [2] M. M. Titirici, M. Antonietti, N. Baccile, *Green Chemistry* **2008**, *10*, 1204.
- [3] M. M. Titirici, A. Thomas, M. Antonietti, *New Journal of Chemistry* **2007**, *31*, 787.
- [4] M. M. Titirici, M. Antonietti, *Chemical Society Reviews* **2010**, *39*, 103.
- [5] R. Demir Cakan, Potsdam (Potsdam), **2009**.
- [6] M. Zheng, Y. Liu, S. Zhao, W. He, Y. Xiao, D. Yuan, *Inorganic Chemistry* **2010**, *49*, 8674.
- [7] X. J. Cui, M. Antonietti, S. H. Yu, *Small* **2006**, *2*, 756.
- [8] N. N. Haihui Ye, Yury Gogotsi, Almila G. Yazicioglu and Canstantine M. Megaridis *Nanotechnology* **2004**, *15*, 232.
- [9] J. P. Paraknowitsch, A. Thomas, M. Antonietti, *Chemistry of Materials* **2009**, *21*, 1170.
- [10] R. D. Cakan, M. M. Titirici, M. Antonietti, G. L. Cui, J. Maier, Y. S. Hu, *Chemical Communications* **2008**, 3759.
- [11] R. Demir-Cakan, N. Baccile, M. Antonietti, M.-M. Titirici, *Chemistry of Materials* **2009**, *21*, 484.
- [12] B. Lu, J. Bai, X. Bo, L. Zhu, L. Guo, *Electrochimica Acta* **2010**, *55*, 8724.
- [13] Z. H. Wen, Q. Wang, Q. Zhang, J. H. Li, *Electrochemistry Communications* **2007**, *9*, 1867.
- [14] R. J. White, M. Antonietti, M.-M. Titirici, *Journal of Materials Chemistry* **2009**, *19*, 8645.
- [15] O. Bobleter, *Progress in Polymer Science* **1994**, *19*, 797.
- [16] I. Hasegawa, Y. Inoue, Y. Muranaka, T. Yasukawa, K. Mae, *Energy & Fuels* **2011**, *25*, 791.
- [17] N. Baccile, M. Antonietti, M.-M. Titirici, *ChemSusChem* **2010**, *3*, 246.
- [18] R. J. White, N. Yoshizawa, M. Antonietti, M.-M. Titirici, *Green Chemistry* **2011**, *13*, 2428.
- [19] Y. Yan, H. F. Yang, F. Q. Zhang, B. Tu, D. Y. Zhao, *Small* **2006**, *2*, 517.
- [20] X. M. Sun, Y. D. Li, *Journal of Colloid and Interface Science* **2005**, *291*, 7.
- [21] S. Ikeda, K. Tachi, Y. H. Ng, Y. Ikoma, T. Sakata, H. Mori, T. Harada, M. Matsumura, *Chemistry of Materials* **2007**, *19*, 4335.
- [22] E. Berl, A. Schmidt, *Justus Liebigs Annalen der Chemie* **1928**, *461*, 192.
- [23] O. Sackur, *Zeitschrift für Elektrochemie und angewandte physikalische Chemie* **1914**, *20*, 260.
- [24] O. Bobleter, G. Bonn, *Carbohydrate Research* **1983**, *124*, 185.
- [25] G. Bonn, O. Bobleter, *Journal of Radioanalytical and Nuclear Chemistry* **1983**, *79*, 171.
- [26] F. S. Asghari, H. Yoshida, *Industrial & Engineering Chemistry Research* **2007**, *46*, 7703.
- [27] B. M. Kabyemela, T. Adschiri, R. M. Malaluan, K. Arai, *Industrial & Engineering Chemistry Research* **1999**, *38*, 2888.
- [28] Y. Yu, X. Lou, H. Wu, *Energy & Fuels* **2007**, *22*, 46.

- [29] T. M. Aida, Y. Sato, M. Watanabe, K. Tajima, T. Nonaka, H. Hattori, K. Arai, *The Journal of Supercritical Fluids* **2007**, *40*, 381.
- [30] T. S. Hansen, J. Mielby, A. Riisager, *Green Chemistry* **2010**, *13*, 109.
- [31] M. Watanabe, Y. Aizawa, T. Iida, T. M. Aida, C. Levy, K. Sue, H. Inomata, *Carbohydrate Research* **2005**, *340*, 1925.
- [32] H. E. van Dam, A. P. G. Kieboom, H. van Bekkum, *Starch - Stärke* **1986**, *38*, 95.
- [33] Y. Roman-Leshkov, J. N. Chheda, J. A. Dumesic, *Science* **2006**, *312*, 1933.
- [34] D. Knezevici, W. P. M. van Swaaij, S. R. A. Kersten, *Industrial & Engineering Chemistry Research* **2009**, *48*, 4731.
- [35] C. m. Lansalot-Matras, C. Moreau, *Catalysis Communications* **2003**, *4*, 517.
- [36] S. H. Yu, X. J. Cui, L. L. Li, K. Li, B. Yu, M. Antonietti, H. Cölfen, *Advanced Materials* **2004**, *16*, 1636.
- [37] X. Cui, M. Antonietti, S.-H. Yu, *Small* **2006**, *2*, 756.
- [38] M. M. Titirici, A. Thomas, S.-H. Yu, J.-O. Müller, M. Antonietti, *Chemistry of Materials* **2007**, *19*, 4205.
- [39] S. K. R. Patil, C. R. F. Lund, *Energy & Fuels* **2011**, *published online*, null.
- [40] M. Sevilla, A. B. Fuertes, *Carbon* **2009**, *47*, 2281.
- [41] G. C. A. Luijkx, W. van der Horst, S. O. A. Koskinen, F. van Rantwijk, H. van Bekkum, *Journal of Analytical and Applied Pyrolysis* **1994**, *28*, 245.
- [42] G. C. A. Luijkx, F. van Rantwijk, H. van Bekkum, M. J. Antal, *Carbohydrate Research* **1995**, *272*, 191.
- [43] M. Möller, P. Nilges, F. Harnisch, U. Schröder, *ChemSusChem* **2011**, *4*, 566.
- [44] C. N. D. Neumann, TU Darmstadt (Darmstadt), **2010**.
- [45] J. Lewkowski, *Arkivok* **2001**, *2*, 17.
- [46] A. A. Rosatella, S. P. Simeonov, R. F. M. Frade, C. A. M. Afonso, *Green Chemistry* **2011**, *13*, 754.
- [47] A. Gandini, *Polymer Chemistry* **2011**, *1*, 245.
- [48] A. Gandini, M. N. Belgacem, *Progress in Polymer Science* **1997**, *22*, 1203.
- [49] C. Moreau, M. N. Belgacem, A. Gandini, *Topics in Catalysis* **2004**, *27*, 11.
- [50] J. Horvat, B. Klaić, B. Metelko, V. Sunjic, *Tetrahedron Letters* **1985**, *26*, 2111.
- [51] D. C. Rideout, R. Breslow, *Journal of the American Chemical Society* **1980**, *102*, 7816.
- [52] M. Choura, N. M. Belgacem, A. Gandini, *Macromolecules* **1996**, *29*, 3839.
- [53] T. Kim, R. S. Assary, C. L. Marshall, D. J. Gosztola, L. A. Curtiss, P. C. Stair, *ChemCatChem* **2011**, *published online*, n/a.
- [54] H. E. Hoydonckx, W. M. Van Rhijn, W. Van Rhijn, D. E. De Vos, P. A. Jacobs, in *Ullmann's Encyclopedia of Industrial Chemistry*, Wiley-VCH Verlag GmbH & Co. KGaA, **2000**.
- [55] M.-M. Titirici, A. Thomas, M. Antonietti, *Journal of Materials Chemistry* **2007**, *17*, 3412.
- [56] Z. Zhang, K. Dong, Z. Zhao, *ChemSusChem* **2011**, *4*, 112.
- [57] H. M. Pilath, M. R. Nimlos, A. Mittal, M. E. Himmel, D. K. Johnson, *Journal of Agricultural and Food Chemistry* **2010**, *58*, 6131.
- [58] F. Salak Asghari, H. Yoshida, *Industrial & Engineering Chemistry Research* **2006**, *45*, 2163.
- [59] R. Brandt, Bayerische Julius-Maximilians-Universität

Würzburg (Würzburg), **2004**.

- [60] R. W. Pekala, *Journal of Materials Science* **1989**, *24*, 3221.
- [61] R. Demir-Cakan, P. Makowski, M. Antonietti, F. Goettmann, M.-M. Titirici, *Catalysis Today* **2010**, *150*, 115.
- [62] J. Park, J. Joo, S. G. Kwon, Y. Jang, T. Hyeon, *Angewandte Chemie International Edition* **2007**, *46*, 4630.
- [63] R. Petricevic, G. Reichenauer, V. Bock, A. Emmerling, J. Fricke, *Journal of Non-Crystalline Solids* **1998**, *225*, 41.
- [64] P. F. Serp, José Luís *CARBON MATERIALS FOR CATALYSIS*, John Wiley & Sons, Inc., New Jersey, **2009**.
- [65] J. M. Conner, V. C. Bulgrin, *Journal of Inorganic and Nuclear Chemistry* **1967**, *29*, 1953.
- [66] M. Levy, E. A. Doisy, *Journal of Biological Chemistry* **1929**, *84*, 749.
- [67] T. Ståhlberg, S. Rodriguez-Rodriguez, P. Fristrup, A. Riisager, *Chemistry – A European Journal* **2011**, *17*, 1456.
- [68] T. A. Houston, B. L. Wilkinson, J. T. Blanchfield, *Organic Lett.* **2004**, *6*, 679.
- [69] P. A. Wehrli, V. Chu, *The Journal of Organic Chemistry* **1973**, *38*, 3436.
- [70] J. L. Gurav, I. K. Jung, H. H. Park, E. S. Kang, D. Y. Nadargi, *Journal of Nanomaterials* **2010**, *2010*.
- [71] H. Kabbour, T. F. Baumann, J. H. Satcher, A. Saulnier, C. C. Ahn, *Chemistry of Materials* **2006**, *18*, 6085.
- [72] X. Lu, M. C. Arduinischuster, J. Kuhn, O. Nilsson, J. Fricke, R. W. Pekala, *Science* **1992**, *255*, 971.
- [73] K. Nakanishi, H. Minakuchi, N. Soga, N. Tanaka, *Journal of Sol-Gel Science and Technology* **1998**, *13*, 163.
- [74] K. J. Klabunde, R. M. Richards, *Nanoscale Materials in Chemistry*, Second Edition, Wiley VHC, **2009**.
- [75] N. Job, A. Thery, R. Pirard, J. Marien, L. Kocon, J. N. Rouzaud, F. Beguin, J. P. Pirard, *Carbon* **2005**, *43*, 2481.
- [76] M. Mirzaeian, P. J. Hall, *Electrochimica Acta* **2009**, *54*, 7444.
- [77] M. C. Gutierrez, F. Pico, F. Rubio, J. M. Amarilla, F. J. Palomares, M. L. Ferrer, F. del Monte, J. M. Rojo, *Journal of Materials Chemistry* **2009**, *19*, 1236.
- [78] J. Marie, R. Chenitz, M. Chatenet, S. Berthon-Fabry, N. Cornet, P. Achard, *Journal of Power Sources* **2009**, *190*, 423.
- [79] H. Tamon, H. Ishizaka, *Journal of Colloid and Interface Science* **2000**, *223*, 305.
- [80] S. A. Al-Muhtaseb, J. A. Ritter, *Advanced Materials* **2003**, *15*, 101.
- [81] J. A. Dahl, B. L. S. Maddux, J. E. Hutchison, *Chemical Reviews* **2007**, *107*, 2228.
- [82] D. C. Wu, R. M. Fu, *Microporous and Mesoporous Materials* **2006**, *96*, 115.
- [83] A. Thomas, F. Goettmann, M. Antonietti, *Chemistry of Materials* **2008**, *20*, 738.
- [84] W. W. Fish, B. D. Bruton, V. M. Russo, *Biotechnology for Biofuels* **2009**, *2*, 18.
- [85] F. a. A. O. o. t. U. Nations, <http://faostat.fao.org/site/567/DesktopDefault.aspx?PageID=567#ancor> **2009**.
- [86] Y. Z. Fang, S. Yang, G. Y. Wu, *Nutrition* **2002**, *18*, 872.
- [87] M. A. Marletta, *Trends in Biochemical Sciences* **1989**, *14*, 488.

- [88] C. Yao, Y. Shin, L.-Q. Wang, C. F. Windisch, W. D. Samuels, B. W. Arey, C. Wang, W. M. Risen, G. J. Exarhos, *The Journal of Physical Chemistry C* **2007**, *111*, 15141.
- [89] M. Sevilla, A. B. Fuertes, *Chemistry – A European Journal* **2009**, *15*, 4195.
- [90] L. Zhao, L.-Z. Fan, M.-Q. Zhou, H. Guan, S. Qiao, M. Antonietti, M.-M. Titirici, *Advanced Materials*, *22*, 5202.
- [91] W. Yang, T.-P. Fellingner, M. Antonietti, *Journal of the American Chemical Society* **2011**, *133*, 206.
- [92] R. Liu, D. Wu, X. Feng, K. Müllen, *Angewandte Chemie International Edition* **2010**, *49*, 2565.
- [93] L. Zhao, N. Baccile, S. Gross, Y. Zhang, W. Wei, Y. Sun, M. Antonietti, M.-M. Titirici, *Carbon*, *48*, 3778.
- [94] Y. Fleury Rey, in *Eur. Pat. Appl., Vol. EP 2000032 20070604* (Ed.: S. Nestec S.A.), Fleury Rey, Yvette., **2008**.
- [95] C. Z. Song, Jiujun, in *PEM Fuel Cell Catalysts and Catalyst Layers: Fundamentals and Applications*, 1st ed. (Ed.: J. Zhang), Springer, **2008**.
- [96] P. Mani, R. Srivastava, P. Strasser, *The Journal of Physical Chemistry C* **2008**, *112*, 2770.
- [97] J. M. Campos-Martin, G. Blanco-Brieva, J. L. G. Fierro, *Angewandte Chemie-International Edition* **2006**, *45*, 6962.
- [98] W. T. Grubb, *Nature* **1963**, *198*, 883.
- [99] Z. Qi, in *PEM Fuel Cell Catalysts and Catalyst Layers: Fundamentals and Applications*, 1st ed. (Ed.: J. Zhang), Springer, **2008**.
- [100] J. Kouvetakis, R. B. Kaner, M. L. Sattler, N. Bartlett, *Journal of the Chemical Society, Chemical Communications* **1986**, 1758.
- [101] H. J. Burch, J. A. Davies, E. Brown, L. Hao, S. A. Contera, N. Grobert, J. F. Ryan, *Applied Physics Letters* **2006**, *89*.
- [102] S. Glenis, A. J. Nelson, M. M. Labes, *Journal of Applied Physics* **1996**, *80*, 5404.
- [103] Y. Y. Shao, J. H. Sui, G. P. Yin, Y. Z. Gao, *Applied Catalysis B-Environmental* **2008**, *79*, 89.
- [104] Q. H. Yang, W. H. Xu, A. Tomita, T. Kyotani, *Chemistry of Materials* **2005**, *17*, 2940.
- [105] D. P. Kim, C. L. Lin, T. Mihalisin, P. Heiney, M. M. Labes, *Chemistry of Materials* **1991**, *3*, 686.
- [106] R. Czerw, M. Terrones, J. C. Charlier, X. Blase, B. Foley, R. Kamalakaran, N. Grobert, H. Terrones, D. Tekleab, P. M. Ajayan, W. Blau, M. Ruhle, D. L. Carroll, *Nano Letters* **2001**, *1*, 457.
- [107] A. C. M. Carvalho, M. C. dos Santos, *Journal of Applied Physics* **2006**, *100*.
- [108] R. B. Kaner, J. Kouvetakis, C. E. Warble, M. L. Sattler, N. Bartlett, *Materials Research Bulletin* **1987**, *22*, 399.
- [109] L. S. Panchakarla, K. S. Subrahmanyam, S. K. Saha, A. Govindaraj, H. R. Krishnamurthy, U. V. Waghmare, C. N. R. Rao, *Advanced Materials* **2009**, *21*, 4726.
- [110] S. Maldonado, K. J. Stevenson, *Journal of Physical Chemistry B* **2005**, *109*, 4707.
- [111] T. Iwazaki, R. Obinata, W. Sugimoto, Y. Takasu, *Electrochemistry Communications* **2009**, *11*, 376.

- [112] J.-i. Ozaki, N. Kimura, T. Anahara, A. Oya, *Carbon* **2007**, *45*, 1847.
- [113] S.-F. Huang, K. Terakura, T. Ozaki, T. Ikeda, M. Boero, M. Oshima, J.-i. Ozaki, S. Miyata, *Physical Review B* **2009**, *80*, 235410.
- [114] L. Yang, S. Jiang, Y. Zhao, L. Zhu, S. Chen, X. Wang, Q. Wu, J. Ma, Y. Ma, Z. Hu, *Angewandte Chemie International Edition* **2011**, n/a.
- [115] J. Ozaki, N. Kimura, T. Anahara, A. Oya, *Carbon* **2007**, *45*, 1847.
- [116] D. W. Wang, F. Li, Z. G. Chen, G. Q. Lu, H. M. Cheng, *Chemistry of Materials* **2008**, *20*, 7195.
- [117] H. L. Guo, Q. M. Gao, *Journal of Power Sources* **2009**, *186*, 551.
- [118] J. P. Paraknowitsch, A. Thomas, M. Antonietti, *Journal of Materials Chemistry* **2010**, *20*, 6746.
- [119] J. P. Paraknowitsch, J. Zhang, D. Su, A. Thomas, M. Antonietti, *Advanced Materials* **2010**, *22*, 87.
- [120] R. Gadiou, A. Didion, D. A. Ivanov, I. Czekaj, R. Kötz, C. Vix-Guterl, *Journal of Physics and Chemistry of Solids* **2008**, *69*, 1808.
- [121] M. Terrones, P. Redlich, N. Grobert, S. Trasobares, W. K. Hsu, H. Terrones, Y. Q. Zhu, J. P. Hare, C. L. Reeves, A. K. Cheetham, M. Ruhle, H. W. Kroto, D. R. M. Walton, *Advanced Materials* **1999**, *11*, 655.
- [122] M. Terrones, H. Terrones, N. Grobert, W. K. Hsu, Y. Q. Zhu, J. P. Hare, H. W. Kroto, D. R. M. Walton, P. Kohler-Redlich, M. Ruhle, J. P. Zhang, A. K. Cheetham, *Applied Physics Letters* **1999**, *75*, 3932.
- [123] M. Terrones, R. Kamalakaran, T. Seeger, M. Ruhle, *Chemical Communications* **2000**, 2335.
- [124] R. Sen, B. C. Satishkumar, S. Govindaraj, K. R. Harikumar, M. K. Renganathan, C. N. R. Rao, *Journal of Materials Chemistry* **1997**, *7*, 2335.
- [125] J. Liu, R. Czerw, D. L. Carroll, *Journal of Materials Research* **2005**, *20*, 538.
- [126] L. J. Zhi, T. Gorelik, R. Friedlein, J. S. Wu, U. Kolb, W. R. Salaneck, K. Mullen, *Small* **2005**, *1*, 798.
- [127] Y. Liu, L. Zhang, L. Cheng, W. Yang, Y. Xu, Q. Zeng, *Journal of Coatings Technology and Research* **2009**, *6*, 509.
- [128] S. Ding, S. Zheng, M. Xie, L. Peng, X. Guo, W. Ding, *Microporous and Mesoporous Materials* **2011**, *142*, 609.
- [129] Y. Inoue, M. Kitano, K. Nakajima, M. Hara, *Chemistry Letters* **2011**, *40*, 410.
- [130] M. Kawaguchi, T. Kawashima, T. Nakajima, *Chemistry of Materials* **1996**, *8*, 1197.
- [131] R. Riedel, J. Bill, G. Passing, *Advanced Materials* **1991**, *3*, 551.
- [132] K. Raidongia, A. Nag, K. P. S. S. Hembram, U. V. Waghmare, R. Datta, C. N. R. Rao, *Chemistry – A European Journal* **2010**, *16*, 149.
- [133] C. N. R. Rao, A. Nag, *European Journal of Inorganic Chemistry* **2010**, *2010*, 4244.
- [134] L. Ci, L. Song, C. Jin, D. Jariwala, D. Wu, Y. Li, A. Srivastava, Z. F. Wang, K. Storr, L. Balicas, F. Liu, P. M. Ajayan, *Nat Mater* **2010**, *9*, 430.
- [135] M. O. Watanabe, S. Itoh, T. Sasaki, K. Mizushima, *Physical Review Letters* **1996**, *77*, 187.
- [136] Y. Chen, J. C. Barnard, R. E. Palmer, M. O. Watanabe, T. Sasaki, *Physical Review Letters* **1999**, *83*, 2406.

- [137] D. Portehault, C. Giordano, C. Gervais, I. Senkovska, S. Kaskel, C. Sanchez, M. Antonietti, *Advanced Functional Materials* **2010**, *20*, 1827.
- [138] R. L. Malenfant-Patrick, J. Wan, S. T. Taylor, M. Manoharan, *Nat Nano* **2007**, *2*, 43.
- [139] A. Vinu, M. Terrones, D. Golberg, S. Hishita, K. Ariga, T. Mori, *Chemistry of Materials* **2005**, *17*, 5887.
- [140] W. Lei, D. Portehault, R. Dimova, M. Antonietti, *Journal of the American Chemical Society* **2011**, *133*, 7121.
- [141] Y. Wang, H. Li, J. Yao, X. Wang, M. Antonietti, *Chemical Science* **2010**, *2*, 446.
- [142] J. S. Lee, H. Luo, G. A. Baker, S. Dai, *Chemistry of Materials* **2009**, *21*, 4756.
- [143] X. Wang, S. Dai, *Angewandte Chemie International Edition* **2010**, *49*, 6664.
- [144] S. A. Forsyth, J. M. Pringle, D. R. MacFarlane, *Australian Journal of Chemistry* **2004**, *57*, 113.
- [145] C. L. Hussey, *Advances in Molten Salt Chemistry* **1983**, *5*, 185.
- [146] K. Gong, F. Du, Z. Xia, M. Durstock, L. Dai, *Science* **2009**, *323*, 760.
- [147] M. Lefèvre, E. Proietti, F. d. r. Jaouen, J.-P. Dodelet, *Science* **2009**, *324*, 71.
- [148] F. d. r. Jaouen, J. Herranz, M. Lefèvre, J.-P. Dodelet, U. I. Kramm, I. Herrmann, P. Bogdanoff, J. Maruyama, T. Nagaoka, A. Garsuch, J. R. Dahn, T. Olson, S. Pylypenko, P. Atanassov, E. A. Ustinov, *ACS Applied Materials & Interfaces* **2009**, *1*, 1623.
- [149] M. Zhang, Y. Yan, K. Gong, L. Mao, Z. Guo, Y. Chen, *Langmuir* **2004**, *20*, 8781.
- [150] S. Pylypenko, S. Mukherjee, T. S. Olson, P. Atanassov, *Electrochimica Acta* **2008**, *53*, 7875.
- [151] C. W. B. Bezerra, L. Zhang, K. Lee, H. Liu, A. L. B. Marques, E. P. Marques, H. Wang, J. Zhang, *Electrochimica Acta* **2008**, *53*, 4937.
- [152] P. Matter, U. Ozkan, *Catalysis Letters* **2006**, *109*, 115.
- [153] V. Nallathambi, J.-W. Lee, S. P. Kumaraguru, G. Wu, B. N. Popov, *Journal of Power Sources* **2008**, *183*, 34.
- [154] J.-i. Ozaki, T. Anahara, N. Kimura, A. Oya, *Carbon* **2006**, *44*, 3358.
- [155] F. d. r. Jaouen, M. Lefèvre, J.-P. Dodelet, M. Cai, *The Journal of Physical Chemistry B* **2006**, *110*, 5553.
- [156] T. Ikeda, M. Boero, S.-F. Huang, K. Terakura, M. Oshima, J.-i. Ozaki, S. Miyata, *The Journal of Physical Chemistry C* **2008**, *114*, 8933.
- [157] J. Maruyama, N. Fukui, M. Kawaguchi, I. Abe, *Journal of Power Sources* **2009**, *194*, 655.
- [158] Y. Tang, B. L. Allen, D. R. Kauffman, A. Star, *Journal of the American Chemical Society* **2009**, *131*, 13200.
- [159] L. Zhang, K. Lee, C. W. B. Bezerra, J. Zhang, J. Zhang, *Electrochimica Acta* **2009**, *54*, 6631.
- [160] R. Cote, G. Lalande, D. Guay, J. P. Dodelet, G. Denes, *Journal of The Electrochemical Society* **1998**, *145*, 2411.
- [161] E. Pollak, G. Salitra, A. Soffer, D. Aurbach, *Carbon* **2006**, *44*, 3302.
- [162] V. V. Strelko, N. T. Kartel, I. N. Dukhno, V. S. Kuts, R. B. Clarkson, B. M. Odintsov, *Surface Science* **2004**, *548*, 281.
- [163] P. S. Singh, V. K. Aswal, *Journal of Colloid and Interface Science* **2008**, *326*, 176.

- [164] S. Yang, X. Feng, X. Wang, K. Müllen, *Angewandte Chemie International Edition* **2011**, *50*, 5339.
- [165] Z. Luo, S. Lim, Z. Tian, J. Shang, L. Lai, B. MacDonald, C. Fu, Z. Shen, T. Yu, J. Lin, *Journal of Materials Chemistry* **2011**, *21*, 8038.
- [166] Y. Okamoto, *Applied Surface Science* **2009**, *256*, 335.
- [167] R. A. Sidik, A. B. Anderson, N. P. Subramanian, S. P. Kumaraguru, B. N. Popov, *Journal of Physical Chemistry B* **2006**, *110*, 1787.
- [168] H. Offermanns, Dittrich G. und Steiner, N., *Chemie in unserer Zeit* **2000**, *3*, 150.
- [169] R. L. Myers, *The 100 Most Important Chemical Compounds: A Reference Guide Vol. 1*, Greenwood Pub Group Inc, **2007**.
- [170] C. Z. Song, J., in *PEM Fuel Cell Electrocatalysts and Catalyst Layers-Fundamentals and Applications*, 1st ed. (Ed.: J. Zhang), Springer, Berlin, **2008**, p. 1159.
- [171] R. Burch, P. R. Ellis, *Applied Catalysis B: Environmental* **2003**, *42*, 203.
- [172] P. P. Olivera, E. M. Patrito, H. Sellers, *Surface Science* **1994**, *313*, 25.
- [173] I. O. Yamanaka, T.; Hashimoto, T.; Murayama, T., *ChemSusChem* **2011**, *4*, 494.
- [174] J. A. P. Mcintyre, Robert F. , United States of America, **1984**.
- [175] C. Oloman, A. P. Watkinson, *Journal of Applied Electrochemistry* **1979**, *9*, 117.
- [176] S. H. C.-R. Langer, J. A., *Chemtech*. **1985**, *15*, 226.
- [177] K. Otsuka, I. Yamanaka, *Catalysis Today* **1998**, *41*, 311.
- [178] I. Yamanaka, T. Murayama, *Angewandte Chemie-International Edition* **2008**, *47*, 1900.
- [179] E. L. Gyenge, C. W. Oloman, *Journal of Applied Electrochemistry* **2001**, *31*, 233.
- [180] E. Lobyntseva, T. Kallio, N. Alexeyeva, K. Tammeveski, K. s. Kontturi, *Electrochimica Acta* **2007**, *52*, 7262.
- [181] J. C. Forti, R. S. Rocha, M. R. V. Lanza, R. Bertazzoli, *Journal of Electroanalytical Chemistry* **2007**, *601*, 63.
- [182] L.-J. Li, M. Glerup, A. N. Khlobystov, J. G. Wiltshire, J. L. Sauvajol, R. A. Taylor, R. J. Nicholas, *Carbon* **2006**, *44*, 2752.
- [183] Z. Xu, W. Lu, W. Wang, C. Gu, K. Liu, X. Bai, E. Wang, H. Dai, *Advanced Materials* **2008**, *20*, 3615.
- [184] B. Wang, Y. Ma, Y. Wu, N. Li, Y. Huang, Y. Chen, *Carbon* **2009**, *47*, 2112.
- [185] F. Piazza, J. E. Nocua, A. Hidalgo, J. De Jesús, R. Velázquez, B. L. Weiss, G. Morell, *Diamond and Related Materials* **2005**, *14*, 965.
- [186] J. D. G. C. Y. Zhi, X. D. Bai, and E. G. Wang *Journal of Applied Physics* **2002**, *91*, 5325.
- [187] N. G. Chopra, R. J. Luyken, K. Cherrey, V. H. Crespi, M. L. Cohen, S. G. Louie, A. Zettl, *Science* **1995**, *269*, 966.
- [188] D. Golberg, Y. Bando, C. C. Tang, C. Y. Zhi, *Advanced Materials* **2007**, *19*, 2413.
- [189] X. Blase, et al., *EPL (Europhysics Letters)* **1994**, *28*, 335.
- [190] J. S. Lee, X. Wang, H. Luo, G. A. Baker, S. Dai, *Journal of the American Chemical Society* **2009**, *131*, 4596.
- [191] T. J. Wooster, K. M. Johanson, K. J. Fraser, D. R. MacFarlane, J. L. Scott, *Green Chemistry* **2006**, *8*, 691.
- [192] Ohtani, Hajime, Ishimura, Shinji, Kumai, Miyuki, *Thermal Decomposition Behaviors of Imidazolium-type Ionic Liquids Studied by Pyrolysis-Gas*

- Chromatography, Vol. 24*, Japan Society for Analytical Chemistry, Tokyo, JAPON, **2008**.
- [193] E. Bernhardt, G. Henkel, H. Willner, *Zeitschrift für anorganische und allgemeine Chemie* **2000**, 626, 560.
- [194] D. Williams, B. Pleune, J. Kouvetakis, M. D. Williams, R. A. Andersen, *Journal of the American Chemical Society* **2000**, 122, 7735.
- [195] Z. Chen, F. Yan, L. Qiu, J. Lu, Y. Zhou, J. Chen, Y. Tang, J. Texter, *Langmuir* **2010**, 26, 3803.
- [196] J. Lu, F. Yan, J. Texter, *Progress in Polymer Science* **2009**, 34, 431.
- [197] E. Riedel, *Anorganische Chemie, Vol. 5*, de Gruyter, Berlin-New York, **2002**.
- [198] D. W. Flick, M. C. Huff, *Catalysis Letters* **1997**, 47, 91.
- [199] J. P. Paraknowitsch, Universität Potsdam (Potsdam), **2009**.
- [200] T. Yamamoto, T. Uemura, A. Tanimoto, S. Sasaki, *Macromolecules* **2003**, 36, 1047.
- [201] H. O. Pierson, *Handbook of Carbon, Graphite, Diamond, and Fullerenes: Properties, Processing, and Applications*, **1993**.
- [202] Y. Saito, T. Yoshikawa, S. Bandow, M. Tomita, T. Hayashi, *Physical Review B* **1993**, 48, 1907.
- [203] D. Mang, H. P. Boehm, K. Stanczyk, H. Marsh, *Carbon* **1992**, 30, 391.
- [204] R. A. Serway, *Principles of Physics*, Saunders College Pub., London, **1998**.
- [205] J. Bill, F. Aldinger, G. Petzow, M. Sloma, J. Maier, R. Riedel, *Journal of Materials Science Letters* **1999**, 18, 1513.